

Modeling the Dispersal of the San Francisco Bay Plume over the Northern and Central California Shelf

Jian Zhou¹, Jonathan Izett², Christopher A Edwards², Pierre Damien³, Faycal Kessouri⁴, and James C. McWilliams³

¹Hohai University

²University of California, Santa Cruz

³University of California Los Angeles

⁴Southern California Coastal Water Research Project

December 21, 2022

Abstract

High-resolution simulations by the Regional Ocean Modeling System (ROMS) were used to investigate the dispersal of the San Francisco Bay (SFB) plume over the northern-central California continental shelf during the period of 2011 to 2012. The modeled bulk dynamics of surface currents and state variables showed many similarities to corresponding observations. After entering the Pacific Ocean through the Golden Gate, the SFB plume is dispersed across the shelf via three pathways: (i) along the southern coast towards Monterey Bay, (ii) along the northern coast towards Point Arena, and (iii) an offshore pathway restricted within the shelf break. On the two-year mean timescale, the along-shore zone of impact of the northward-dispersed plume is about 1.5 times longer than that of the southern branch. Due to the opposite surface Ekman transports induced by the northerly or southerly winds, the southern plume branch occupies a broader cross-shore extent, roughly twice as wide as the northern branch which extends roughly two times deeper due to coastal downwelling. Besides these mean characteristics, the SFB plume dispersal also shows considerable temporal variability in response to various forcings, with wind and surface-current forcing most strongly related to the dispersing direction. Applying constituent-oriented age theory, we determine that it can be as long as 50 days since the SFB plume was last in contact with SFB before being flushed away from the Gulf of the Farallones. This study sheds light on the transport and fate of SFB plume and its impact zone with implications for California's marine ecosystems.

Modeling the Dispersal of the San Francisco Bay Plume over the Northern and Central California Shelf

Jian Zhou^{1,2,3}, Jonathan G. Izett², Christopher A. Edwards², Pierre Damien³,
Fayçal Kessouri^{3,4}, and James C. McWilliams³

¹State Key Laboratory of Hydrology-Water Resources and Hydraulic Engineering, Hohai University,
Nanjing, Jiangsu, China

²Department of Ocean Sciences, University of California, Santa Cruz, CA, USA

³Department of Atmospheric and Oceanic Sciences, University of California, Los Angeles, CA, USA

⁴Biogeochemistry Department, Southern California Coastal Water Research Project, Costa Mesa, CA,
USA

Key Points:

- Three distinct dispersal pathways of San Francisco Bay plume are identified: southward, northward, and offshore
- Zone of impact of the northern plume is farther along-shore, narrower cross-shore, and vertically deeper compared to the southern branch
- Surface water typically spends less than 50 days in the Gulf of the Farallones after entering via the Golden Gate

Corresponding author: Jian Zhou, jzhou@hhu.edu.cn

Abstract

High-resolution simulations by the Regional Ocean Modeling System (ROMS) were used to investigate the dispersal of the San Francisco Bay (SFB) plume over the northern-central California continental shelf during the period of 2011 to 2012. The modeled bulk dynamics of surface currents and state variables showed many similarities to corresponding observations. After entering the Pacific Ocean through the Golden Gate, the SFB plume is dispersed across the shelf via three pathways: (i) along the southern coast towards Monterey Bay, (ii) along the northern coast towards Point Arena, and (iii) an offshore pathway restricted within the shelf break. On the two-year mean timescale, the along-shore zone of impact of the northward-dispersed plume is about 1.5 times longer than that of the southern branch. Due to the opposite surface Ekman transports induced by the northerly or southerly winds, the southern plume branch occupies a broader cross-shore extent, roughly twice as wide as the northern branch which extends roughly two times deeper due to coastal downwelling. Besides these mean characteristics, the SFB plume dispersal also shows considerable temporal variability in response to various forcings, with wind and surface-current forcing most strongly related to the dispersing direction. Applying constituent-oriented age theory, we determine that it can be as long as 50 days since the SFB plume was last in contact with SFB before being flushed away from the Gulf of the Farallones. This study sheds light on the transport and fate of SFB plume and its impact zone with implications for California's marine ecosystems.

Plain Language Summary

San Francisco Bay (SFB) is the largest estuary on the U.S. West Coast, situated in a highly urbanized region impacted by agricultural, industrial, and commercial wastes. As water exits the SFB through the narrow Golden Gate strait and meets the Pacific Ocean currents, it forms the SFB Plume: a layer of low-salinity water that advances over the denser seawater. Understanding how SFB plume and the nutrients, phytoplankton, and contaminants it contains are distributed in the coastal ocean is crucial for the ecosystem management of a network of National Marine Sanctuaries. This study uses three-dimensional realistic numerical simulations to explore the transport of SFB plume over the northern-central California continental shelf. We focus on the different pathways along which the SFB plume moves and the respective zones of impact in response to various atmospheric and oceanic forcings (e.g., wind and river discharge). A timescale analysis reveals that SFB plume is

50 typically flushed out of the Gulf of the Farallones within 50 days since it leaves the Golden
51 Gate. Our study sheds light on how the anthropologically modulated SFB plume may in-
52 fluence the highly dynamic marine ecosystem off the U.S. West Coast, which supports one
53 of the world’s most productive fisheries.

54 **1 Introduction**

55 Rivers carry more than one-third of land-based precipitation to the ocean (Trenberth
56 et al., 2007), channeling large freshwater fluxes through narrow outlets along the coast.
57 The impact of the terrigenous material carried by the river water into ecologically sensitive
58 coastal waters depends strongly on physical processes that transport and transform buoyant
59 freshwater in the region around the river mouth as it merges with deeper, salty ocean waters.
60 In particular, the dilution rates and along-shore transport rates of river-borne material
61 are determined by a suite of processes, including stratified-shear mixing, frontal processes,
62 geostrophic transport, and wind forcing (Whitney & Garvine, 2006; Horner-Devine et al.,
63 2015; Basdurak et al., 2020; Xiao et al., 2021). In the coastal ocean, these discharges
64 form river plumes, which are distinct regions where water properties and dynamics are
65 significantly influenced by the riverine freshwater. The distinguishing dynamical feature of
66 a river plume is the horizontal advection of freshwater from the river mouth that defines
67 the shape and character of the plume. The associated dispersal pathway of a river plume
68 depends on outflow angle (Garvine, 1999), wind forcing (Fong & Geyer, 2001; S. Lentz,
69 2004), ambient current (Fong & Geyer, 2002), and latitude (Sharples et al., 2017; Izett &
70 Fennel, 2018a). Given the temporal variation of some forcing, freshwater pathways are often
71 highly mobile, and the unsteady freshwater transport pathways have important ecological
72 implications related to contaminant, larval, and nutrient transport (e.g., Cahill et al., 2008;
73 Kessouri, McLaughlin, et al., 2020).

74 The San Francisco Bay (SFB) is the largest estuary on the west coast of North America.
75 Its watershed extends from the ridgeline of the Sierra Nevada mountains to the strait of the
76 Golden Gate. SFB has been a focus of research by the U.S. Geological Survey (USGS)
77 since 1969 to learn how estuaries respond to hydroclimatic and human disturbances such as
78 nutrient enrichment (Cloern et al., 2020). The formation of the SFB plume is due to mixing
79 of coastal seawater that has entered the bay on flood tides and incoming freshwater from the
80 Sacramento and San Joaquin Rivers, prior to returning to the ocean as the SFB plume on
81 the ebb tide (Fram et al., 2007). The supply of coastal seawater into the bay far exceeds the

82 average river input, resulting in an SFB plume that has a relatively high salinity compared
83 to a typical river plume. Upon entering coastal waters, the plume is influenced by prevailing
84 winds and near surface currents north, west, or south over the relatively broad continental
85 shelf (S. J. Lentz, 1987). The chemical constituents of the SFB plume differ from the river
86 and coastal seawater entering the bay because the saline estuary has its own internal cycling
87 of nutrients that is largely driven by anthropogenic inputs within the estuary (Cloern, 1996;
88 Wang et al., 2020). Characterizing the plume’s dispersal is of fundamental importance for
89 understanding any influence of San Francisco Bay on coastal biogeochemical processes in an
90 ecologically sensitive region (Chin et al., 2001) that includes a network of National Marine
91 Sanctuaries (NMSs) such as the Greater Farallones NMS, the Cordell Bank NMS, and the
92 Monterey Bay NMS. The Gulf of the Farallones is loosely indicated in Figure 3, covering the
93 region on the shelf from Point Reyes in the north to Pedro Point south of the Golden Gate,
94 though the boundaries of the NMS extend further north. For a map of the NMSs outside the
95 Golden Gate, please refer to <https://farallones.noaa.gov/gallery/maps.html>. Further
96 place names used in the text are highlighted in Figure 12.

97 The SFB plume enters into the California Current System (CCS), an Eastern Boundary
98 Upwelling System (Huyer, 1983; Hickey, 1998; Jacox et al., 2018; Renault et al., 2020). In the
99 central portion of the CCS during spring/summer, predominantly equatorward, along-shore
100 winds induce offshore Ekman transport and coastal upwelling, drawing nutrient-rich water
101 from depth; downwelling is driven by poleward along-shore winds that result in onshore
102 Ekman transport (e.g., Marchesiello et al., 2003). To date, little is known about the levels
103 and spatio-temporal patterns of SFB plume dispersal within the Gulf of Farallones and
104 further afield in the context of complex oceanic circulations along the U. S. West Coast
105 (Kaplan & Largier, 2006; Hurst & Bruland, 2008). As such, the mechanisms that drive
106 SFB plume dispersal on the shelf and its subsequent fate in the coastal ocean remains
107 unclear. Furthermore, the SFB plume has high levels of nutrients, phytoplankton, dissolved
108 organic matter, and contaminants (Wang et al., 2020), which may be similar to upwelled
109 concentrations (Hurst & Bruland, 2008).

110 In this study, we numerically investigate the dispersal pathways of the SFB plume over
111 the northern and central California shelf in the period of 2011–2012. A downscaled Regional
112 Ocean Modeling System (ROMS) configuration was established, scaling from a 4-km hori-
113 zontal resolution configuration spanning the entire CCS (Renault et al., 2020; Deutsch et al.,
114 2020), to a 1-km resolution grid covering much of the California coast (Kessouri, Bianchi,

115 et al., 2020), and finally to a 0.3-km grid along the portions of the northern and central
116 California coast centered around the San Francisco Bay (this study). The 0.3-km ROMS
117 grid was coupled with high-frequency ocean-estuary exchanges derived from a well-validated
118 SFB-focused modeling study (Wang et al., 2020) using the Semi-implicit Cross-scale Hy-
119 droscience Integrated System Model (SCHISM). The main objectives are to characterize
120 the shelf-wide spreading of SFB-sourced water discharged from the Golden Gate, and to
121 describe the mean characteristics and temporal variability of its dispersal pathways. We
122 will address the following two major concerns regarding the spatio-temporal pattern of the
123 SFB plume dispersal: (i) how is the net baywater effluent dispersed in the coastal ocean
124 along the various pathways? and (ii) how sustained are periods dominated by any given
125 pathway throughout the investigated time span? This paper lays groundwork for coupled
126 physical-biogeochemical investigations of anthropogenic nutrient discharges in support of
127 San Francisco Bay Nutrient Management Strategy ([https://sfbaynutrients.sfei.org/
128 books/nutrient-management-strategy-san-francisco-bay](https://sfbaynutrients.sfei.org/books/nutrient-management-strategy-san-francisco-bay)).

129 **2 Model Configuration**

130 **2.1 Oceanic Configuration**

131 The Regional Ocean Modeling System, ROMS (Shchepetkin & McWilliams, 2005;
132 Shchepetkin, 2015), is used for the ocean circulation simulations. ROMS is a primitive-
133 equation, hydrostatic, terrain-following oceanic model that allows high-resolution simula-
134 tions in shallow shelf seas. It contains state-of-art numerical algorithms that provide an
135 accurate and stable representation of physical processes down to scales of tens of meters,
136 and allows for multi-level offline downscaling of higher-resolution subdomains within larger
137 domains. Vertical mixing in the boundary layers is represented by a K-profile parameteri-
138 zation (Large et al., 1994).

139 The U.S. hindcast model (Figure 1a) has been successfully run over two decades at 4-km
140 (L0 domain) and 1-km (L1 domain) horizontal resolutions using high-resolution spatial and
141 temporal atmospheric forcing that represents the effects of near-coast wind stress changes,
142 current feedback on the surface stress, and high-frequency wind fluctuations (Renault, Hall,
143 & McWilliams, 2016; Renault, Molemaker, et al., 2016). The L0 simulation was initialized
144 and forced at the open boundaries by a pre-existing northeast Pacific-wide ROMS solution at
145 12-km resolution (Renault et al., 2020), which was initialized and forced on the boundaries

146 by the global model Mercator Glorys2V3 (<http://www.myocean.eu>). The L0 simulation
 147 was run for the period 1995-2017 after a spin-up of 2 years. The L1 simulation was then
 148 initialized and forced by the L0 model, starting in October 1996 and ending in December
 149 2017. Readers are referred to Renault et al. (2020), Deutsch et al. (2020), and Kessouri,
 150 Bianchi, et al. (2020) for the details of 1-km and 4-km model setups and boundary forcings.

151 Forced at the western, southern, and northern boundaries and initialized by the L1
 152 solution, this study investigates the L2 domain with a nominal resolution of 0.3 km ($450 \times$
 153 1200 horizontal cells in total) to capture submesoscale processes, focusing on portions of
 154 the northern and central California coast centered around the San Francisco Bay (Figure
 155 1a). The offline downscaling is based on the Orlanski scheme for the baroclinic mode
 156 (Marchesiello et al., 2001) and a modified Flather scheme for the barotropic mode (Mason
 157 et al., 2010). The model domain extends along a 400-km stretch of the coast (spanning
 158 from Ragged Point in the south to Point Arena in the north), and about 150 km offshore.
 159 The bathymetry data were acquired from the General Bathymetric Chart of the Oceans
 160 (GEBCO_2019) with 15 arc-second resolution. The grid has 60 σ -coordinate vertical levels
 161 with stretching parameters of $\theta_s = 6$, $\theta_b = 3$, and $h_c = 250$ m (Shchepetkin & McWilliams,
 162 2009). The L2 domain is tidally forced by adding the TPXO9-atlas barotropic tides (Egbert
 163 & Erofeeva, 2002) to the L1 forcing at the northern, western, and southern boundaries. The
 164 first 10 constituents are phased with the tide-resolving eastern boundary forcing from the
 165 SCHISM model (i.e., at the Golden Gate).

166 2.2 Ocean-Estuary Coupling

167 A portion of the eastern boundary of the L2 domain is forced at the Golden Gate by
 168 high-frequency (two-hourly) output from a well-validated SFB-focused modeling study over
 169 the 10-year period of 2005–2014 (Wang et al., 2020, see Figure 1b) using the Semi-implicit
 170 Cross-scale Hydroscience Integrated System Model (SCHISM). SCHISM is an open-source
 171 community model based on unstructured grids designed for seamless simulation of three-
 172 dimensional baroclinic circulation across creek-lake-estuary-shelf-ocean scales (Y. Zhang &
 173 Baptista, 2008; Y. Zhang et al., 2016). The 3D model output of momentum, temperature,
 174 and salinity across the Golden Gate in the SCHISM model (yellow line in Figure 1b) were
 175 extracted and offline coupled with the ROMS model. A major challenge was that the ROMS
 176 (structured grid) and SCHISM (unstructured grid) models differ in the bathymetry across
 177 the Golden Gate due to different horizontal and vertical resolutions. Therefore, momentum

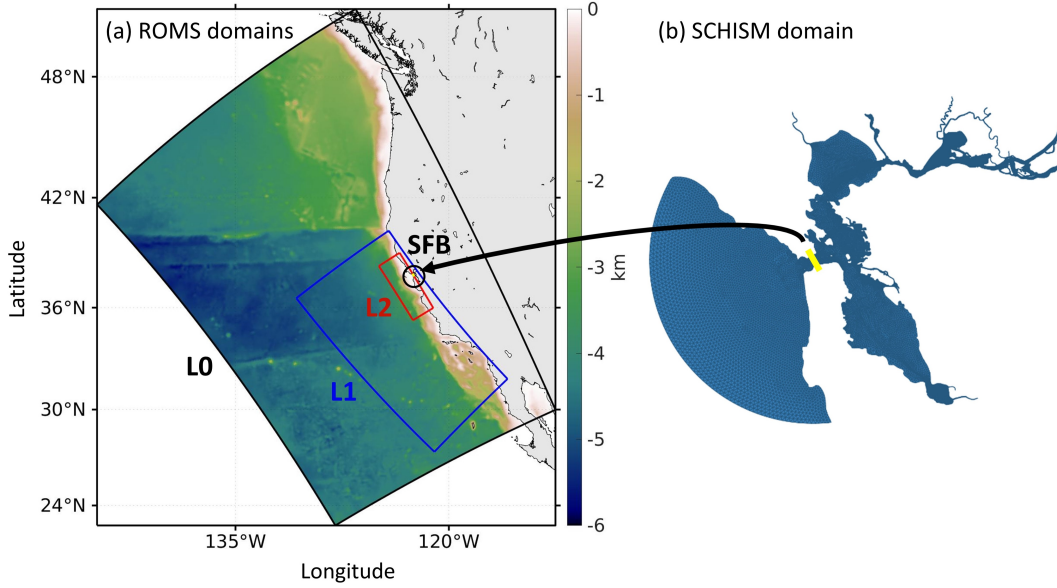


Figure 1. Model configuration: (a) ROMS nested domains; (b) SCHISM domain by Wang et al. (2020). In (a), continuous colors represent bathymetry along the U.S. West Coast and discrete rectangular perimeters indicate the triple grid nesting configuration. The black, blue, and red boxes show the L0, L1, and L2 domains with horizontal resolutions of 4 km, 1 km, and 0.3 km (the present study), respectively. The innermost circle in (a) corresponds to the estuary-focused domain in (b). The yellow line in (b) indicates the cross section from which 3D momentum, temperature, and salinity are extracted to force the eastern boundary of the L2 domain in (a).

178 and tracer concentrations were re-constructed as being laterally uniform while preserving
 179 their vertical structures, which we consider to be more important to capture the key features
 180 of ocean-estuary exchange flows at such a narrow strait. Due to the different average sea
 181 levels between models, the sea surface height at every location of the eastern boundary
 182 was forced as $\zeta = \bar{\zeta}_{\text{ROMS, no SFB-forcing}} + \zeta'_{\text{SCHISM}}$, where $\bar{\zeta}_{\text{ROMS, no SFB-forcing}}$ refers to the
 183 mean sea surface height in ROMS simulations without SFB-forcing (i.e., a closed eastern
 184 boundary condition), and ζ'_{SCHISM} represents sea surface height anomalies in the SCHISM
 185 model.

186 To avoid the ambiguity of reference salinity for ocean water in the coastal ocean (e.g.,
 187 Castela et al., 2008) and also to isolate the San Francisco Bay plume from other sources of
 188 fresh water in the model, a passive, conservative tracer with unit concentration was intro-
 189 duced at the Golden Gate. Following the simulated passive tracer concentration gives an
 190 unambiguous measure, anywhere in the model domain, of the volume fraction of water con-

191 tributed by the SFB outflow, hereafter referred to as “baywater”. The model was initialized
192 with zero baywater concentration everywhere outside of the Golden Gate.

193 As described in section 2.1, an Orlanski scheme was used for 3D temperature and
194 salinity on the eastern boundary, while the clamped open boundary conditions was used for
195 3D momentum. This approach seeks discharge volume consistency with the SCHISM model,
196 as it has been validated against measurements of major river runoffs (including Sacramento
197 River and San Joaquin River) by the California Department of Water Resources (DWR).

198 The model was integrated with a baroclinic time step of $dt = 30$ seconds. Model fields
199 were saved as sequential two-hour averages in order to achieve an accurate calculation of
200 the residual baywater flux which may be dominated by the tidal pumping flux in tidally
201 energetic estuaries and coastal seas (Fram et al., 2007; Zhou et al., 2020; Zhou & Stacey,
202 2020). The L2 simulation was run from January 2011 to December 2012. Upon investigation,
203 remnant coastal freshwater inherited from the L1 solution (where river runoff was included
204 as surface precipitation) is completely dispersed in the L2 simulation on the order of 1–2
205 months, consistent with the results in section 5 where the mean water age in the Gulf of
206 Farallones is generally less than 50 days. Given this rapid flushing, no spin-up period for
207 the passive tracer is considered. As a verification, shifting the average time window forward
208 by 2 months (i.e., from March 2011 to February 2013; not shown) has little effect on the
209 long-term pattern of baywater dispersal.

210 **3 Model Evaluation**

211 Before proceeding to the analysis of the simulation results, we evaluate the model to
212 establish that the modeled ocean hydrodynamics has acceptable fidelity with respect to rel-
213 evant observations. We focus on the L2 domain, as the L0 and L1 domains were previously
214 validated against available observations (Renault et al., 2020). Though discrepancies be-
215 tween the model and data exist, the model-data comparison for various fields shows good
216 overall representation of features of the bulk dynamics of surface currents and state variables.
217 Our goal is to demonstrate that the model is valid for the statistical average simulation of
218 baywater spreading in ocean water off the central California coast. We note that there has
219 been no assimilation of satellite or other data in these simulations.

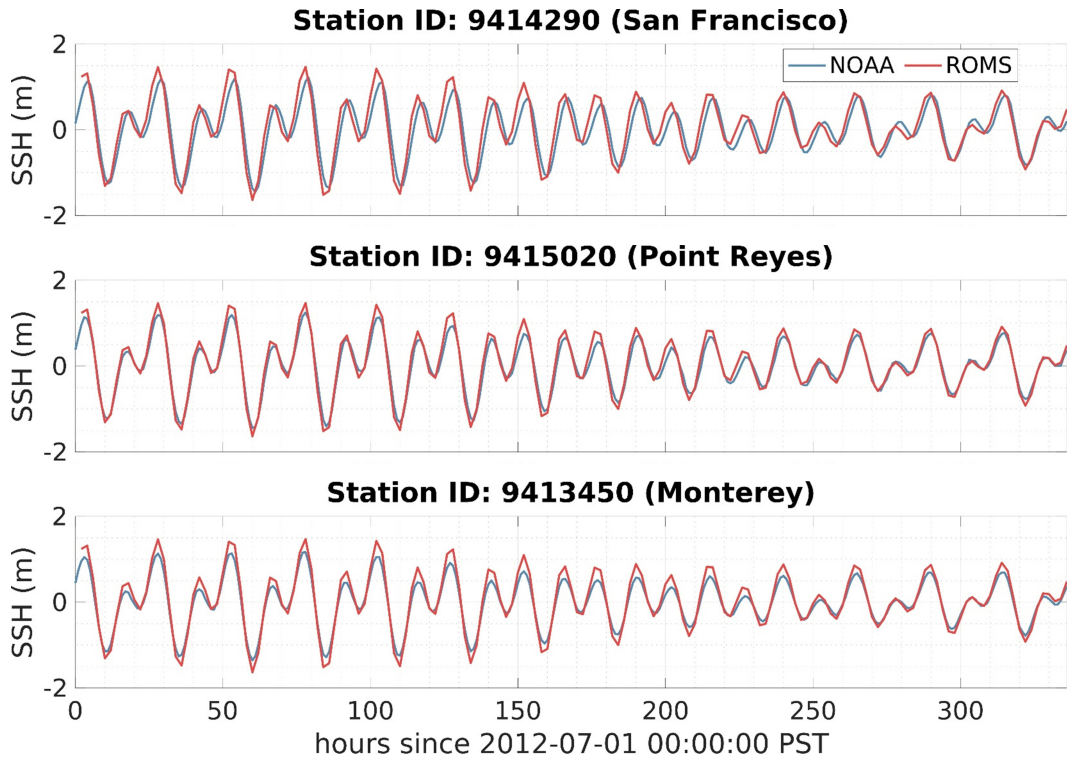


Figure 2. Comparison of modeled and observed sea surface height time-series at three representative locations (blue lines: NOAA tidal gauge measurements; red lines: ROMS simulations). Data during the first two weeks of July 2012 are shown for demonstration.

220 3.1 NOAA Tidal Gauge Measurements

221 The National Oceanic and Atmospheric Administration (NOAA) provides hourly wa-
 222 ter level information at various locations along the U.S. coast ([https://tidesandcurrents](https://tidesandcurrents.noaa.gov/)
 223 [.noaa.gov/](https://tidesandcurrents.noaa.gov/)), with three tide gauge stations within our model domain: 9414290 (San Fran-
 224 cisco), 9415020 (Point Reyes), and 9413450 (Monterey). The modeled sea surface height is
 225 compared with NOAA measurements in Figure 2 for two weeks in July 2012. The model
 226 agrees well with the observations, with root-mean-square deviations (RMSD) between the
 227 model and observation throughout 2011–2012 of 0.318 m, 0.238 m, and 0.234 m for stations
 228 9414290 (San Francisco), 9415020 (Point Reyes), and 9413450 (Monterey), respectively.

229 3.2 High-Frequency Radar Data of Surface Current

230 The land-based HF Radar Network (HFRNet; [https://hfrnet-tds.ucsd.edu/thredds/](https://hfrnet-tds.ucsd.edu/thredds/catalog.html)
 231 [catalog.html](https://hfrnet-tds.ucsd.edu/thredds/catalog.html)) was developed to measure the speed and direction of ocean surface currents

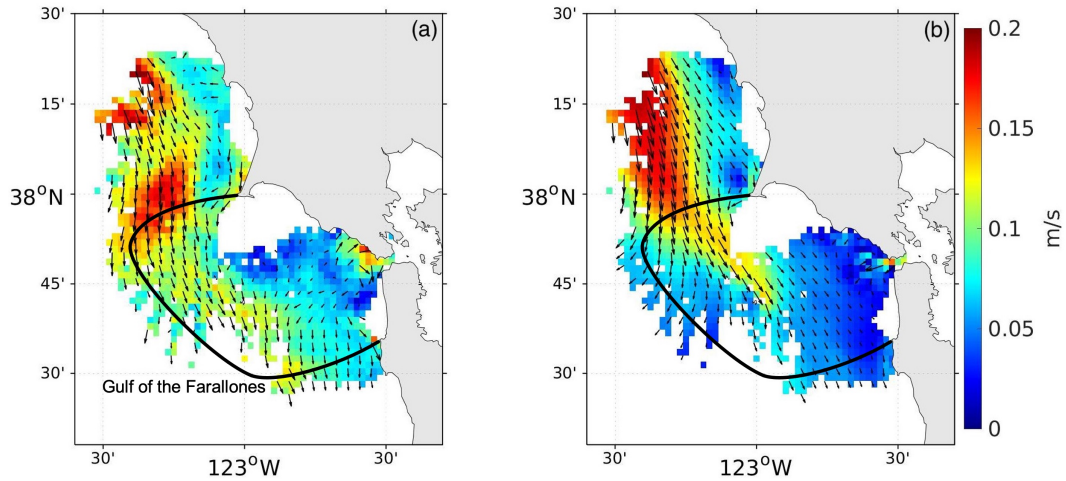


Figure 3. Comparison of annual-mean surface currents for the year 2012 at the outflow of the Golden Gate, including the Gulf of the Farallones (indicated with black outline): (a) observed (HFR); (b) modeled. Color represents current magnitude, and scaled arrows indicate the direction. Note that the model results (0.3 km-resolution) are remapped onto the HFR grid (2 km-resolution) to aid comparison.

232 in near real-time. HFR data covering the U.S. West Coast (including the Central California
 233 Coast centered around the San Francisco Bay) first became available in 2012.

234 Figure 3 compares the annual mean surface currents between HFR data and the model
 235 in 2012. The observed data are plotted only at locations where data availability in time
 236 exceeds 70%; modeled results are plotted at the same locations for ease of comparison. Over
 237 this time period, both observations and model show a predominantly southward mean flow.
 238 Surface currents are generally weak close to the coast, strengthening offshore. A tongue-
 239 shaped zone of strong southward flow north of Point Reyes is successfully reproduced, with
 240 the model showing a somewhat more continuous pattern. Discrepancies between the model
 241 and data also exist. In particular, there exists a difference in mean flow within the Gulf of
 242 the Farallones. The model shows weak alongshore flow whereas the observations indicate
 243 stronger offshore flow. Discrepancies between observations and the model may in part
 244 result from the differing data availability across the average period: the model has full
 245 temporal coverage across the investigated period, while at some locations there are only
 246 limited HFR data available to contribute to the annual mean current. This is especially
 247 the case immediately outside of the Golden Gate where sufficiently high temporal coverage
 248 is needed to obtain averaged currents on tidal and spring-neap timescales. Meanwhile,

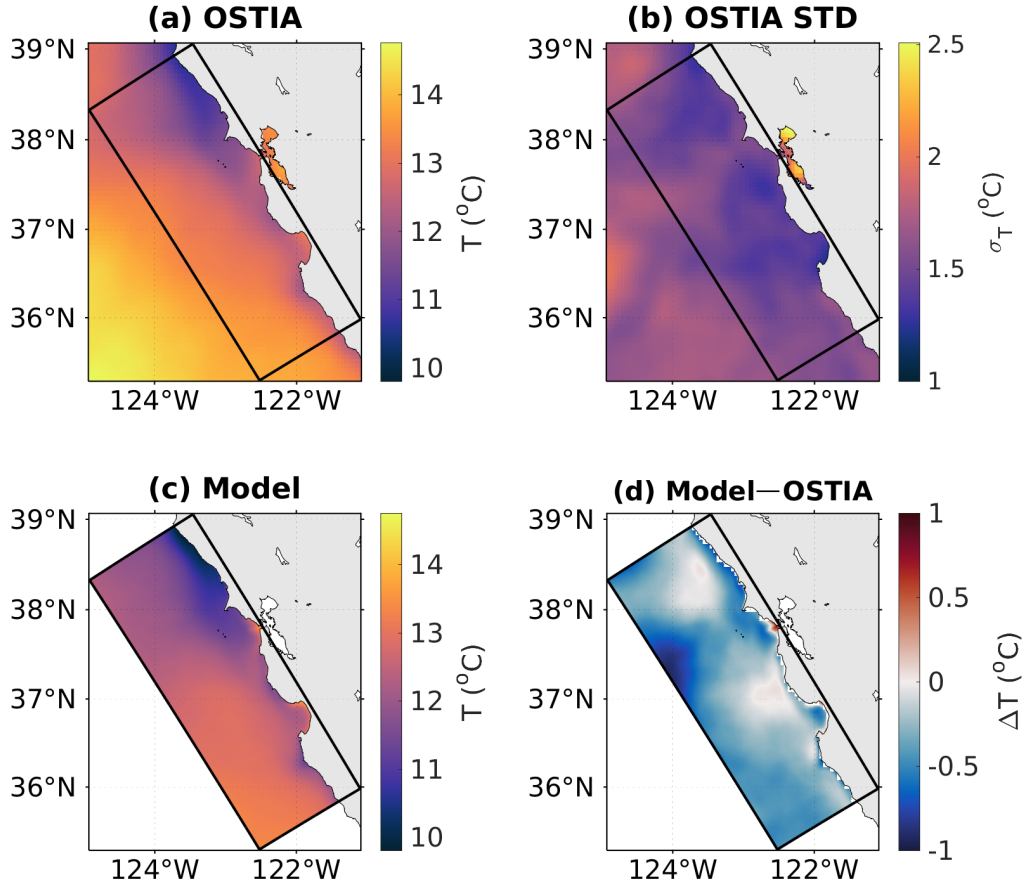


Figure 4. Comparison of observed and modeled 2-year mean sea surface temperature: (a) OSTIA Level-4 product; (b) standard deviation of OSTIA data; (c) modeled SST; (d) model bias ($SST_{\text{model}} - SST_{\text{obs}}$).

249 different spatial resolutions may also contribute to the model-data discrepancy (i.e. 2 km in
 250 the HFR data and 0.3 km in the model). Despite the differences, the general patterns are
 251 well represented and yield a Pearson correlation coefficient of 0.63.

252 3.3 Remote-Sensing Observations of Sea Surface Temperature

253 Sea surface temperature (SST) is one measure of ocean temperature that is readily
 254 available for model evaluation in satellite observations. We compare the GHRSSST Level 4
 255 OSTIA SST product with a spatial resolution of $0.05^\circ \times 0.05^\circ$ ([https://podaac.jpl.nasa](https://podaac.jpl.nasa.gov/dataset/OSTIA-UKMO-L4-GLOB-v2.0)
 256 [.gov/dataset/OSTIA-UKMO-L4-GLOB-v2.0](https://podaac.jpl.nasa.gov/dataset/OSTIA-UKMO-L4-GLOB-v2.0)) to the model results. As shown in Figure 4, the

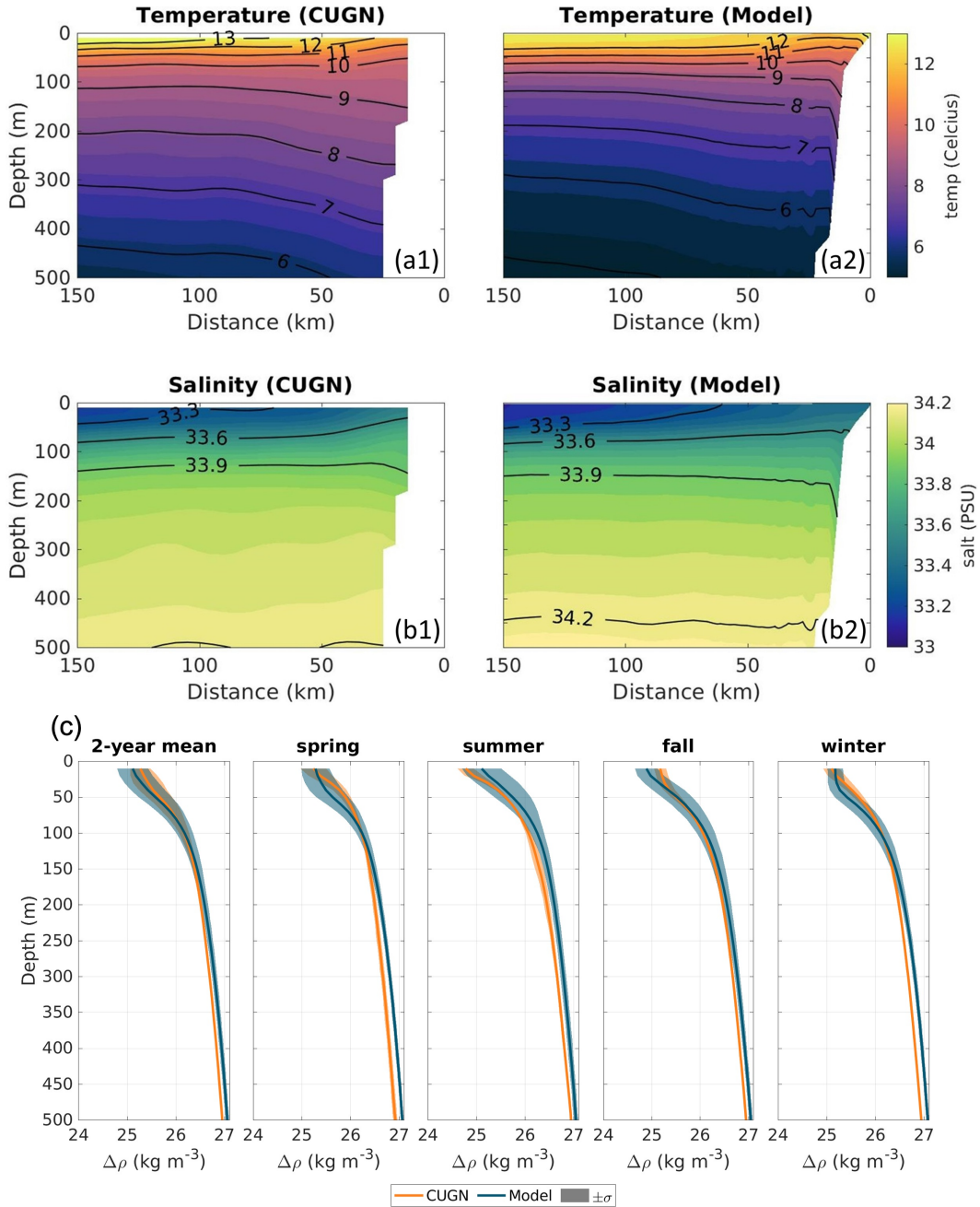


Figure 5. Model evaluation using CUGN data: (a) cross-shore contours of two-year mean (2011–2012) water temperature; (b) cross-shore contours of two-year mean (2011–2012) salinity; (c) vertical profiles of the density anomaly along CalCOFI line 66.7 over the entire 2-year period of 2011–2012 and in different seasons. In (c), both the CUGN data (orange lines) and model results (blue lines) are averaged along the cross-shore direction as shown in (a) and (b), with the shading representing ± 1 standard deviation.

257 overall level and the horizontal distribution of mean SST during 2011–2012 are reasonably
258 captured with a predominantly cold bias throughout the domain, except at the Golden Gate
259 where modeled SST is warmer than OSTIA SST. Overall, biases are smaller than 1°C in
260 magnitude, which is less than the OSTIA standard deviation throughout the domain. We
261 note that instantaneous comparisons of modeled and remotely sensed SST are more variable.
262 Greater discrepancies between model and data on short time-scales are to be expected as
263 small-scale features (e.g., eddies and filaments) are quite nonlinear and less predictable than
264 longer-term mean features.

265 **3.4 The California Underwater Glider Network**

266 The California Underwater Glider Network (<http://spraydata.ucsd.edu/climCUGN/>),
267 CUGN, uses autonomous underwater gliders to measure variables including temperature and
268 salinity. The gliders make repeated dives from the surface to 500-m depth and back, repeat-
269 ing the cycle every 3 hours, and traveling 3 km horizontally each cycle. We compare our
270 model output to the glider data from the cross-shore California Cooperative Oceanic Fish-
271 eries Investigations (CalCOFI) line 66.7 off Monterey Bay (see black dotted line in Figure 6).
272 For ease of comparison, both the CUGN and model data are averaged along the cross-shore
273 direction to obtain vertical density profiles as a function of time. This comparison provides
274 an assessment of the model performance in terms of vertical stratification in the ocean. As
275 shown in Figure 5, agreement in the vertical structure is generally good for the two-year
276 mean of temperature and salinity, with the mean halocline a bit deeper in the model than
277 observations. The model successfully reproduces the shoaling of the pycnocline during sum-
278 mer due to solar heating and upwelling, while also capturing the deepening during winter
279 due to diminished insolation and increased surface turbulence (Figure 5c). The modeled
280 mean pycnocline is, however, deeper (~10 m) than observed in spring and winter, with less
281 (more) dense surface water in fall (summer).

282 **4 Baywater Dispersal**

283 **4.1 Analysis Framework**

284 To examine the patterns of the SFB plume spreading over the continental shelf and
285 beyond, we consider flow across a total of 30 arcs (thick gray lines in Figure 6) centered
286 at the Golden Gate. The radii of the arcs increase by 5 km, starting at a radius of 5 km

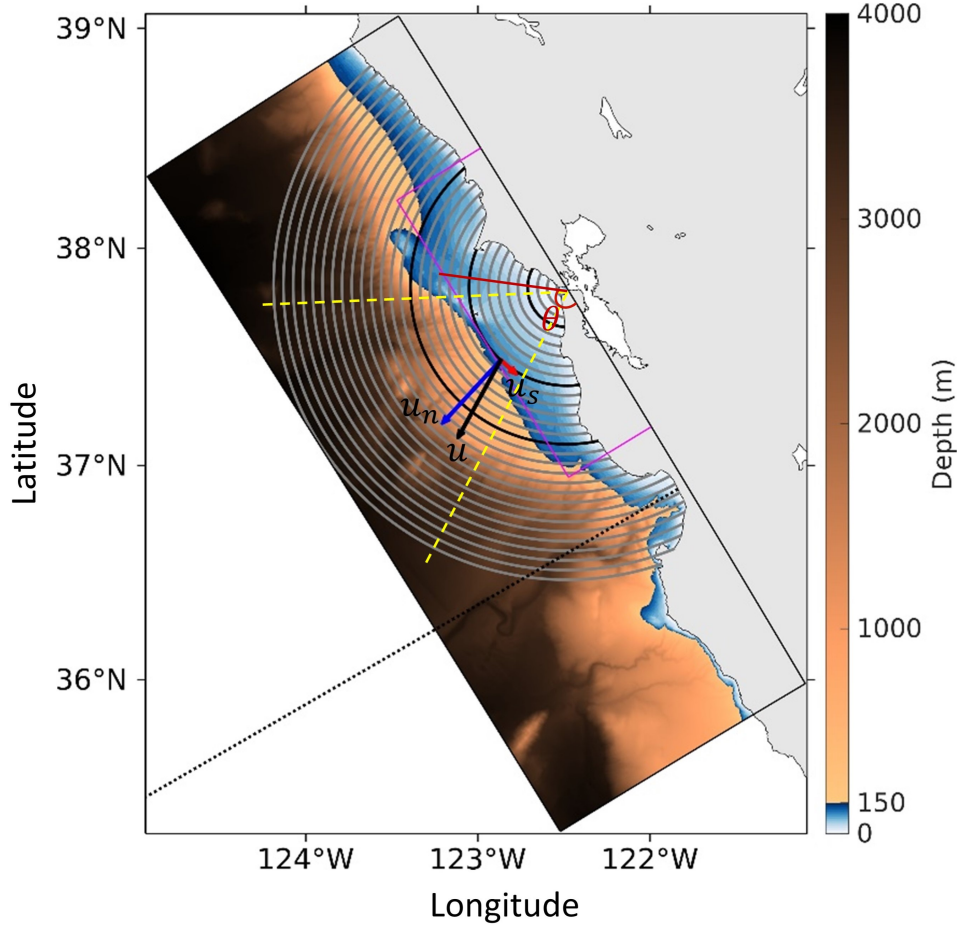


Figure 6. Analysis framework of baywater dispersal superimposed on the bathymetry of the present L2 domain. The continental shelf (defined as regions with depths ≤ 150 m) is highlighted by the bluish colorscale. The concentric arcs on which passive tracer flux is calculated are colored by gray, except for the three black arcs which indicate the locations of the representative arcs in Figure 8. The azimuth angle θ starts at the eastern edge of the grid and increases clockwise. The yellow dashed lines divide the arcs into their southern, offshore, and northern segments (as θ increases from zero). The magenta box indicates the subdomain within which the winds and surface currents are averaged in Figure 10. The CalCOFI line 66.7 is marked by the black dotted line (see section 3.4).

287 (arc 1) out to a radius of 150 km (arc 30). Throughout this paper, “arc i ” corresponds to
 288 the arc with a radius of $5i$ km. At any location on a certain arc, the flow velocity vector is
 289 decomposed into its normal component u_n (blue arrow) and tangential component u_s (red
 290 arrow). Positive u_n is defined as outgoing from the source (i.e., spreading away from the

291 SFB), and positive u_s indicates velocities directed toward the northern end of an arc. We
 292 focus primarily on arcs with radii smaller than 100 km.

293 4.2 Mean Plume Characteristics

294 The two-year (2011-2012) time-averaged, depth-integrated passive-tracer concentration
 295 (Figure 7a) reveals the typical patterns of the SFB plume as it disperses across the northern
 296 and central California shelf. For visualization, the color scale for the depth-integrated tracer
 297 C_{VI} is selected to have an upper limit of 1 in order to emphasize tracer decay structure over
 298 the shelf. The immediate inner-shelf region within the first arc is heavily influenced by the
 299 tidal jets through the narrow Golden Gate, exhibiting elevated levels of vertically integrated
 300 tracer ranging from 1–30. Throughout much of the domain, except for the tidally dominated
 301 region < 25 km from the Golden Gate, the standard deviation of the mean field (Figure 7b)
 302 is considerably larger than the mean, highlighting the plume’s variability. Overall, the plume
 303 influences a large region of the shelf, with the mean tracer found all along the shelf from
 304 near Point Arena to the Monterey Bay.

305 In addition to horizontal variability, the plume is vertically inhomogeneous. Figure 7c
 306 plots the mean centroid depth the SFB plume, $h_c = \int zCdz / \int Cdz$. Overall, the plume
 307 centroid remains shallower than ~ 20 m deep throughout much of the Gulf and to the south,
 308 with plume waters north of Point Reyes extending more deeply. On the innermost arcs, the
 309 plume occupies the whole water depth ($D < 2h_c$). As the arc crosses the shelf break (around
 310 $r = 50$ km), depth increases dramatically and $2h_c$ more reasonably represents the vertical
 311 plume dimension.

312 The 2012 monthly mean fields in Figures 7d–o further illustrate the temporal variabil-
 313 ity of the plume, with the spatial pattern highly variable. Three major baywater transport
 314 pathways emerge: (i) a northward pathway, (ii) a southward pathway, and (iii) an offshore-
 315 directed pathway. The northward pathway is characterized by a sharp, buoyant coastal
 316 current whose tracer signature extends well north of Point Reyes to roughly 120 km up the
 317 coast, largely penetrating deeper than the rest of the plume and travelling closer to the
 318 coast. The second pathway is directed southward from the Golden Gate. It starts as a
 319 strong, broad, shallow feature near its source ($r < 20$ km) that is roughly twice as wide and
 320 the northward pathway and with the highest concentrations shifted offshore. The plume be-
 321 comes increasingly diffuse and less concentrated between 30 and 100 km from the Gate. The

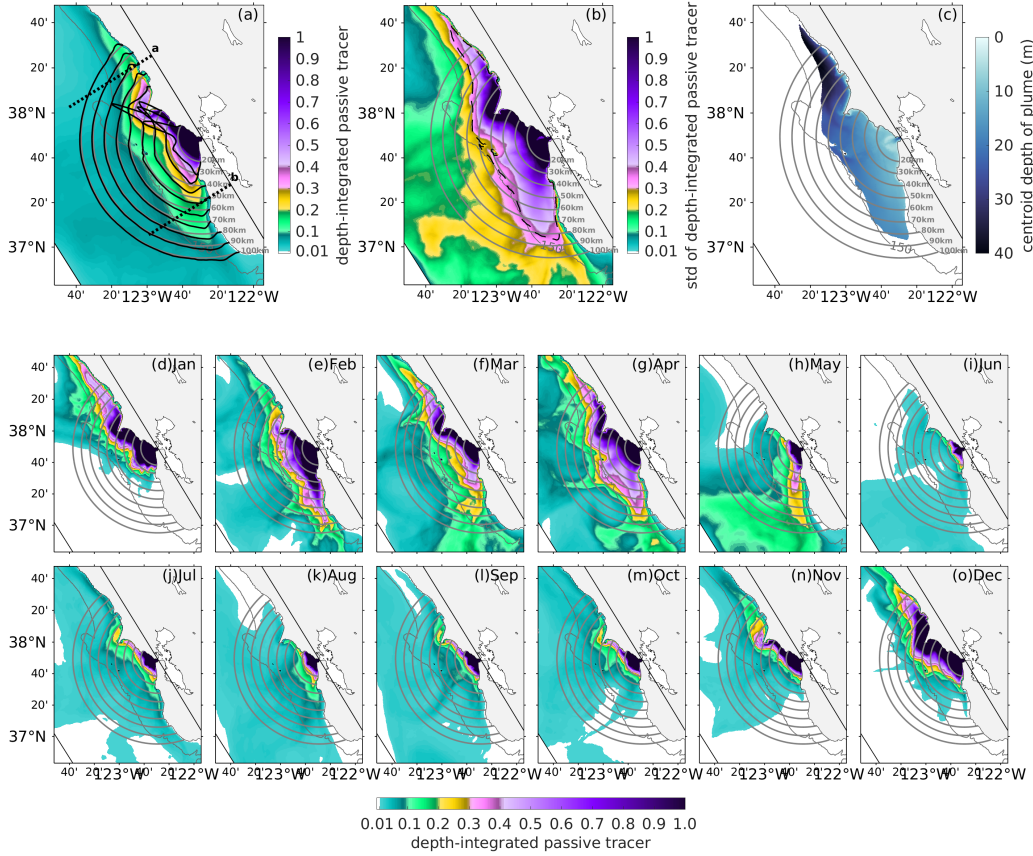


Figure 7. Depth-integrated passive tracer. (a) Two-year mean vertically integrated passive tracer concentration, C_{VI} . Black lines indicate the vertically integrated tracer flux across each arc. The two dotted lines indicate locations of the cross-shore planes in Figure 11 that extend 80 km from the eastern edge of the domain. (b) Standard deviation of mean passive tracer with dashed line indicating the point where $C_{VI} = 0.1$ in (a). (c) Centroid depth of passive tracer within the mean plume. (d–o) Monthly mean vertically integrated tracer concentrations in the year 2012. In all panels, the 150-m isobath is shown as a demarcation between shelf and slope.

322 third pathway is directed westward, but decays offshore quite rapidly, extending only weakly
 323 beyond the shelf-break. This pathway appears transiently and rarely in instantaneous fields
 324 compared to the northward and southward directed motions.

325 The cross-shelf dispersal of baywater seems to be greatly suppressed, with the majority
 326 of the SFB plume body (e.g., with depth-integrated passive tracer concentrations higher
 327 than 0.1) largely inshore of the 150-m isobath (see the portion of plume encompassed by the
 328 dashed line in Figure 7b). Conservation of potential vorticity in a rotating, homogeneous, in-

329 viscid, and steady fluid requires transport along and not across bathymetric contours (Brink,
 330 1998). Though this fluid is not homogeneous, inviscid, or steady, cross-isobath transport is
 331 severely constrained in this region, as it is in other coastal environments. Although cross-
 332 shore Ekman transport at the surface and in the bottom boundary layer, as well as transient
 333 motions (e.g., eddies and filaments), do result in cross-shore flow, their impact on the mean
 334 baywater dispersal is quite modest. While the California Current system is an eddy-rich
 335 region (Kessouri, Bianchi, et al., 2020) with potential impacts on biogeochemical activity
 336 (Gruber et al., 2011), our simulations do not indicate eddy transport as a significant mech-
 337 anism within the Gulf of the Farallones itself. Instead, we find that the eddy kinetic energy
 338 within the Gulf is almost entirely contained within sub-tidal timescales, with little sustained
 339 (sub-)mesoscale energy (not shown).

340 The mean radial flux of baywater reveals vertical and horizontal plume structure at
 341 different distances from the Golden Gate. Figure 8 plots azimuth-depth contours of tracer
 342 flux across three representative arcs. On arc 4 (Figure 8a), a typical two-layer estuarine
 343 circulation (gravitational circulation; Geyer & MacCready, 2014) can be observed even at
 344 this offshore location, with outgoing flux near the surface and ingoing flux at depth. On arc
 345 10 (Figure 8b), the estuarine circulation largely diminishes, and there exists an ingoing flux
 346 between $\theta = 100\text{--}150^\circ$, associated with a recirculation near Drakes Bay and south of Point
 347 Reyes (see Figure 7a). On arc 16 (Figure 8c), the bathymetry deepens significantly as the
 348 arc crosses the shelf break. At this distance, it is clear that the plume exists as a thin layer
 349 in the upper few tens of meters, sharply differentiated from the underlying shelf and slope
 350 water. This structure is a common feature of surface-trapped river plumes (Fong & Geyer,
 351 2002; Horner-Devine et al., 2015).

352 A more quantitative description of the average baywater dispersal can be based on
 353 simple geometrical arguments, testing a model to describe the mean vertically integrated
 354 passive tracer concentration (\overline{C}_{VI}) on a given arc, knowing only the modeled vertically
 355 integrated passive tracer concentration on arc 1 ($\overline{C}_{VI,\text{modeled}}|_{r_1}$). The overbar here indicates
 356 averaging along a given arc (i.e., arc-averaged). The total concentration along an arc of
 357 radius, r , is equal to $2\pi\overline{C}_{VI,\text{calculated}} \cdot r$. If we assume that all of the passive tracer on arc 1
 358 is dispersed onto an outer arc, a uniformly spreading plume would be described as

$$359 \quad \overline{C}_{VI,\text{calculated}} = \overline{C}_{VI,\text{modeled}}|_{r_1} \cdot (r/r_1)^{-1}. \quad (1)$$

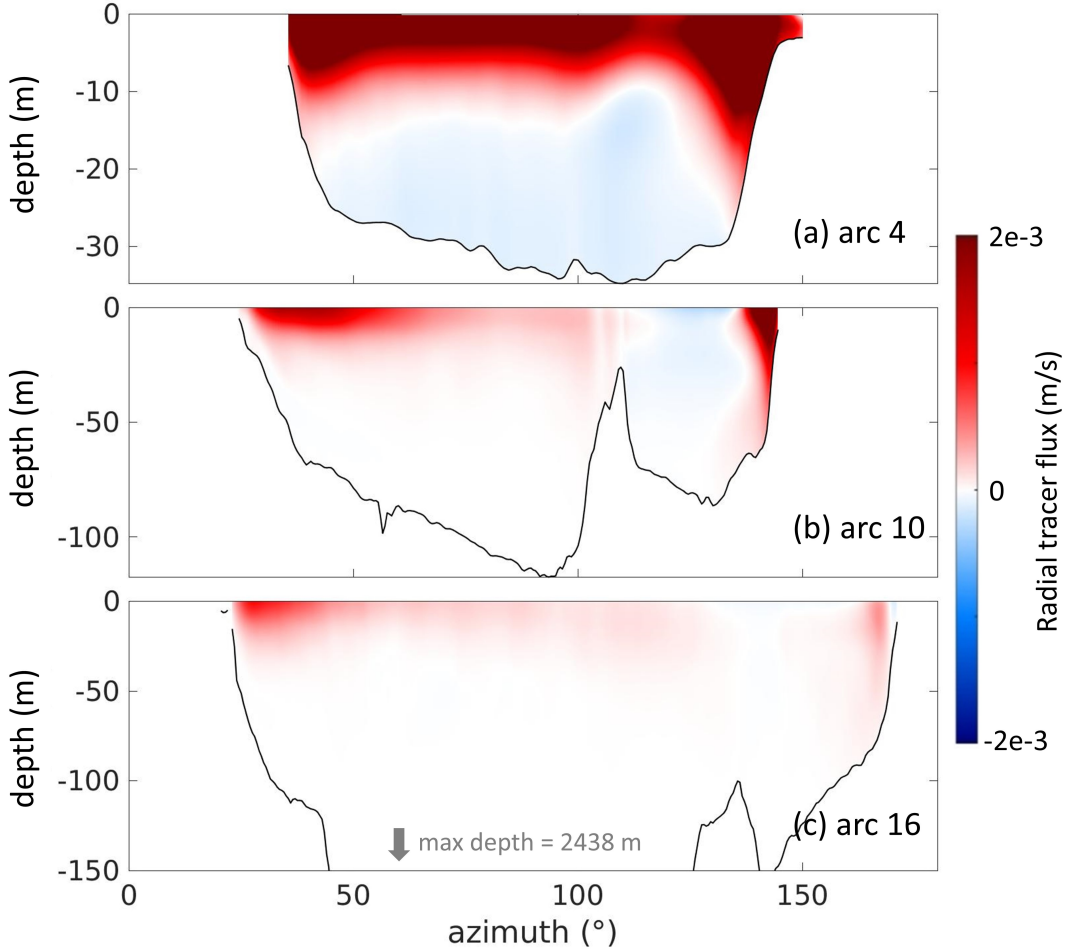


Figure 8. Two-year mean radial tracer flux across three representative arcs. Note the differing extents of vertical axes among panels. In (c), the max depth reaches 2438 meters, but only the upper 150 meters of water is shown.

360 Equation (1) is plotted in Figure 9 for all the 30 arcs considered in section 4.1. Rather
 361 than scaling directly with the ratio of the arc radii, the plume is best described by a -1.4
 362 power law, a more rapid decline in concentration than predicted by pure spreading. The
 363 -1.4 power relationship likely results from the local storage of tracer on the inner arcs and
 364 cross-arc mixing. It is also worth noting that as r increases in Figure 9, the curve of $2\bar{h}_c$
 365 (an approximation for the arc-averaged vertical dimension of the plume) gradually flattens,
 366 in contrast to the considerable increase of arc-averaged water depth \bar{D} . This is consistent
 367 with Figure 8c where the plume exists as a thin surface layer on distant outer arcs.

The above spreading analysis assumes advective dispersal. A similar exercise can also be conducted for a purely diffusive case. Assuming a continuous point source at the origin,

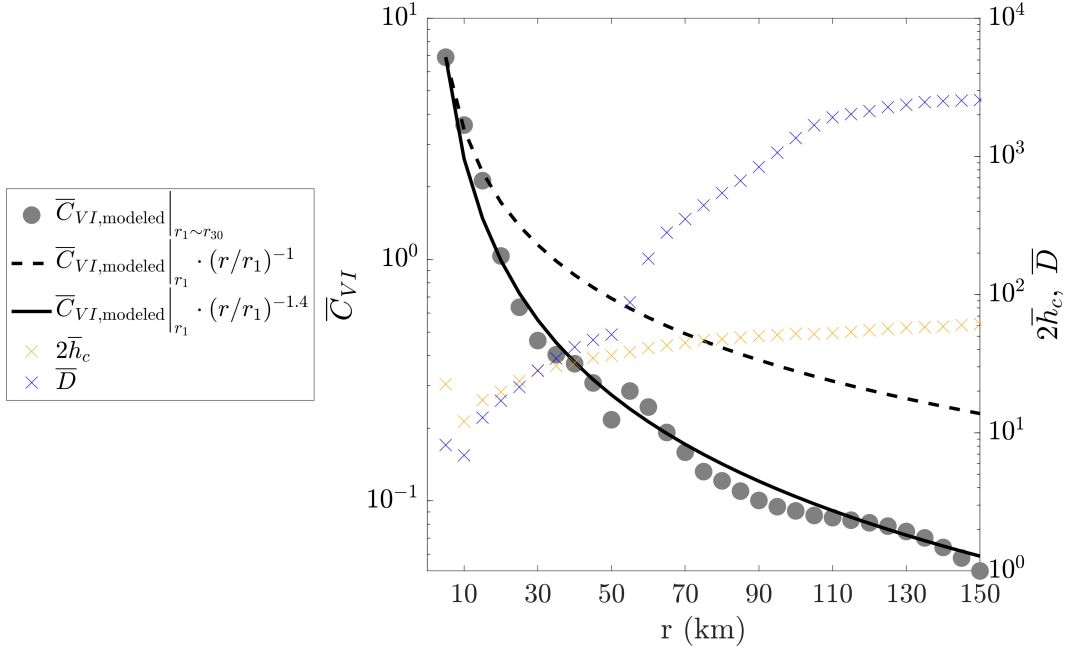


Figure 9. Vertically integrated passive tracer averaged along a given arc, \overline{C}_{VI} , as a function of arc radius, illustrating the geometrical plume spreading.

if the diffusion coefficient is κ and the source strength at radius $r = 0$ is $S > 0$ starting at $t = 0$ when the concentration is $C(r, 0) = 0$, then the concentration on each arc will increase in time and decrease with distance according to (Carslaw & Jaeger, 1959; Crank, 1975):

$$C(r, t) = \frac{S}{4\pi\kappa} E_1\left(\frac{r^2}{4\kappa t}\right), \quad (2)$$

368 where $E_1(x) = \int_x^\infty \frac{e^{-t}}{t} dt$ is the exponential integral. Under this purely diffusive assumption,
 369 the concentration decreases rapidly with increasing radial distance. Combining both the
 370 advective and diffusive analysis, we can infer that the transport is predominantly advective,
 371 though with some diffusive influence and storage given the more rapid decay in concentration
 372 ($r^{-1.4}$) than predicted by pure advection.

4.3 Drivers of Temporal Variability

374 While mean properties are useful to describe the overall behavior of the SFB plume,
 375 temporal information offers understanding of the drivers of plume dynamics. Two-year
 376 timeseries of several fields related to baywater dispersal are presented in Figure 10, including
 377 the net baywater discharge at the Golden Gate, the cross-shore and along-shore winds,
 378 the along-shore barotropic pressure gradient, and the along-shore surface-current velocity.

379 We note that the net baywater discharge in Figure 10a should not be interpreted as the
 380 conventional “river discharge” of typical river plumes because freshwater enters the San
 381 Francisco Bay from the Sacramento River and San Joaquin delta far upstream of the Golden
 382 Gate, and these waters undergo intensive mixing with saline water of coastal origin before
 383 being exported from the estuary. To remove high-frequency signals and focus on subtidal
 384 frequencies, we apply a Godin filter, a three-step low-pass filter (Godin, 1972), to all time-
 385 series in this figure. Despite this filtering, there remains a small spring-neap cycle visible in
 386 Figure 10a that likely still results from tidal aliasing. Winds and surface currents are spatial
 387 averages within a sizable subdomain (indicated by the magenta box in Figure 6) that spans
 388 the majority of the region of interest. Positive baywater flux is defined as outgoing from
 389 SFB.

390 The bay discharge (Figure 10a) shows largest amplitude in the spring of 2011 with small
 391 values through the rest of the 2-year period. The winter/spring signal in Q is surprisingly
 392 muted in 2012. Characteristic equatorward winds are apparent during much of the two years
 393 (Figure 10c), punctuated by brief reversals (also referred to as relaxations) that last a few
 394 days except for more sustained poleward winds during early spring of 2011 and 2012 and
 395 late fall/winter of 2012. The spatial mean along-shore surface current (Figure 10e) generally
 396 follows that of the along-shore wind, except for September 2011–January 2012 when the
 397 Davidson Current (a poleward surface coastal current off U.S. West Coast) dominates (Reid
 398 & Schwartzlose, 1962; Hickey & Pola, 1983; Connolly et al., 2014). This is manifested by
 399 the poleward barotropic pressure gradient between September 2011 and January 2012 in
 400 Figure 10d.

401 Figure 10f–h presents plume dispersal characteristics, including net baywater discharge
 402 across arc 10 ($r = 50$ km) as a function of time and angle relative to the alongshore strike
 403 of the coast (Figure 10f), the total transport across arc 10 in the three pathways identified
 404 (Figure 10g), and the angle reached by the furthest point on the plume with a vertically
 405 integrated passive-tracer concentration of at least 1.0 (Figure 10h). An azimuth of 25° indi-
 406 cates transport adjacent to the coast south of the Golden Gate, 90° indicates the direction
 407 directly offshore, and 145° corresponds to waters adjacent to the coast to its north. Regions
 408 with azimuth ranges of 0° – 25° and 145° – 180° are land-masked.

409 Figure 10f reveals characteristic spatial and temporal patterns of baywater discharge.
 410 Export from the Golden Gate generally crosses arc 10 either over much of its southern

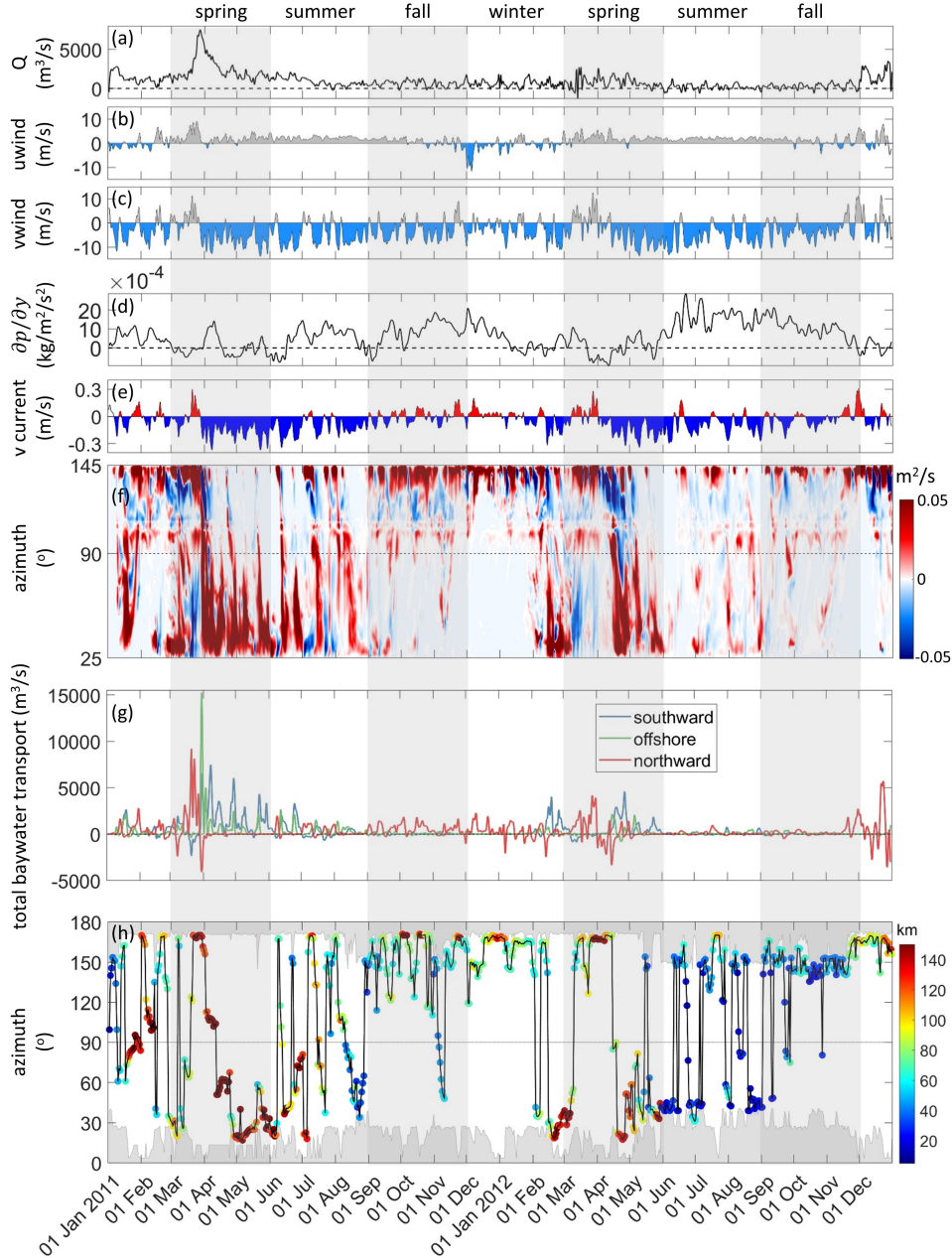


Figure 10. Godin-filtered time series of (a) net baywater discharge at the Golden Gate; (b) subdomain-averaged cross-shore wind (light blue indicates easterly wind); (c) subdomain-averaged along-shore wind (light blue indicates northerly wind); (d) along-shore barotropic pressure gradient, $(p_{\text{south}} - p_{\text{north}})/L$, in a narrow coastal band (L is the along-shore distance between the northern/southern boundaries); (e) subdomain-averaged along-shore surface current (blue indicates southward current); (f) vertically integrated baywater flux across arc 10.; (g) spatially integrated baywater transport across the three segments of arc 10; (h) positional history of the plume front. In (h): color indicates the radius of the outermost arc across which the maximum vertically-integrated tracer concentration C_{VI} is higher than 1.0; and vertical axis indicates the azimuthal location of maximum value on the outmost arc; gray-shaded area represents the coastal land-masked cells for the corresponding arc.

411 half, or in a very narrow zone near its northern edge. Between these export signals is a
 412 recirculation that crosses the arc toward the Golden Gate, between $\theta \approx 105^\circ$ and 125° ,
 413 consistent with the baywater circulation shown in Figure 7. All of these features of the
 414 cross-arc flow variability can also be observed for arcs with $r = 20\text{--}60$ km in Figure 7, but
 415 disappear for more distant arcs ($r = 70\text{--}100$ km; not shown).

416 There is a noticeable seasonality in the baywater dispersal patterns, with peak fluxes
 417 predominantly occurring during spring months and the temporal variation of baywater
 418 highly dependent on net input of baywater into the domain, the wind field, and the surface
 419 current. Generally south and northward baywater flux occur during south and northward
 420 alongshore surface currents (Figure 10e), respectively. The baywater transport intensity on
 421 the arc differs between years, with the outgoing flux being stronger and more continuous in
 422 the spring of 2011 than in 2012, and clearly related to the interannual differences in peak
 423 discharge. Overall, there is a pattern of north/south switching, with baywater discharge
 424 generally being larger in magnitude to the south or north but not simultaneously.

425 Consistent with idealized river plume studies (e.g., Fong & Geyer, 2001, 2002; S. Lentz,
 426 2004), the pattern of the along-shore wind field significantly influences the behavior of the
 427 SFB plume. As shown in Figure 11, the direction and magnitude of the wind forcing deter-
 428 mines the plume shape. Southerly, downwelling-favorable wind drives northward dispersal
 429 of baywater and the associated onshore surface Ekman transport confines higher concentra-
 430 tions near to the coast (Figure 11a). Equatorward (northerly), upwelling-favorable winds
 431 lead to southward dispersal of baywater and the associated offshore surface Ekman trans-
 432 port draws the plume away from the coast (Figure 11b). These qualitative descriptions are
 433 borne out in the spatial patterns shown in Figure 7.

434 A plume's trajectory is the result of its forcing history. As such, comparing instantane-
 435 ous forcing to instantaneous plume direction does not result in any significant correlations.
 436 We find, however, that comparing 1-week running means with lag times of up to a few days
 437 can result in high correlations between a forcing parameter and plume azimuth. Azimuth
 438 is most strongly related to the surface currents ($r^2 > 0.8$ for a two-week lag), which are in
 439 turn strongly related to the near-surface winds. As a result, the mean plume azimuth is
 440 also well-correlated with the wind direction ($r^2 > 0.7$), with strengthening northerly winds
 441 resulting in more pronounced southward plume transport.

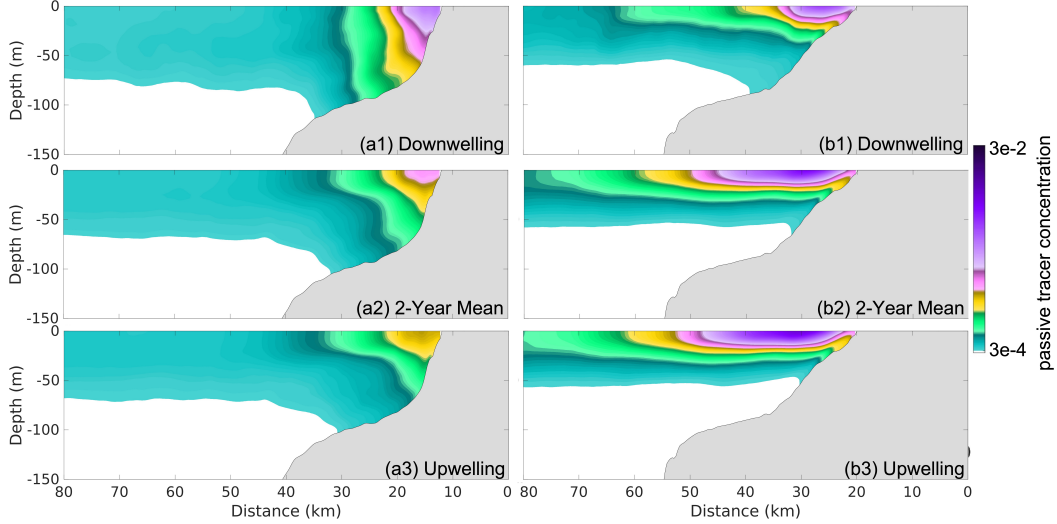


Figure 11. Cross-shore contours of passive tracer concentration at transects a and b in Figure 7a for different conditional averaging: (1) during downwelling (southerly winds) conditions, (2) two-year mean, and (3) during upwelling (northerly wind) conditions.

4.4 Spatio-Temporal Summary of Transport

Based on the discussions in preceding sections, Figure 12 provides a more global perspective on the spatio-temporal pattern of the shelf-wide spreading of the SFB plume. Figure 12 plots the total baywater transport (solid lines) and the total time spent in a given pathway (dashed lines) with increasing arc radius on the vertical axis. More precisely, \bar{Q}_i is the two-year averaged, spatially integrated baywater transport across the three arc segments as defined in Figure 6, where i corresponds to one of the following: “total”, “southward”, “off-shore”, and “northward”, and \bar{Q}_{GG} is the two-year mean baywater discharge at the Golden Gate, which is 924 m^3 (an invariant number that is strictly matched between ROMS and SCHISM models). The total time the plume is dominated by southward, offshore, and northward baywater transport, denoted $\sum T_i$, is determined by accumulating periods with the largest intensity of the three pathways throughout 2011–2012 on each arc (see Figure 10g for the example of arc 10 with a radius of 50 km). Finally, $\sum T_{total}$ is the total length of the two-year timeframe.

Values for \bar{Q}_i/\bar{Q}_{GG} reveal how net baywater effluent is distributed along the different transport pathways in a temporally averaged sense. For example, at $r = 75 \text{ km}$, $\bar{Q}_{southward}/\bar{Q}_{GG} = 43.5\%$ (blue solid), indicating that on this arc 43.5% of the total bay-

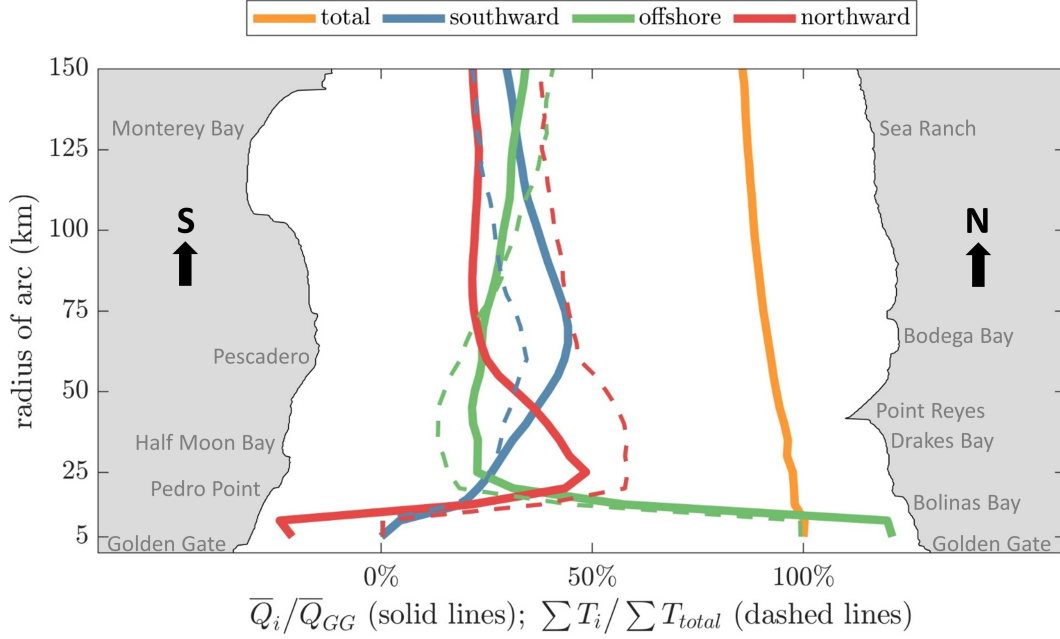


Figure 12. Spatio-temporal pattern of baywater dispersal as a function of arc radius. Solid lines: proportions of two-year mean southward ($\theta = 0-120^\circ$), offshore ($\theta = 120-240^\circ$), and northward ($\theta = 240-360^\circ$) transport of the total 2-year mean discharge at the Golden Gate (924 m^3); Dashed lines: fraction of time dominated by southward, offshore, and northward transport throughout 2011–2012. The southern and northern coastlines surrounding the Golden Gate are superimposed to provide context for the given radii.

459 water discharge is dispersed along the southward pathway. Near the Golden Gate ($r < 25$
 460 km), offshore transport $\bar{Q}_{offshore}/\bar{Q}_{GG}$ (green) dominates other pathways and for $r < 10$
 461 km, the northern pathway (red) is negative, indicating a return flow on northern segments.
 462 Offshore transport declines rapidly from the Golden Gate as the baywater tracer flux shifts
 463 primarily to the northern and secondarily to the southern pathways. At arcs free from the
 464 SFB tidal pulses ($r > 25$ km), $\bar{Q}_{offshore}/\bar{Q}_{GG}$ shows a mild increase as it receives tracer
 465 from two separate sources: (i) Tracer within the northward pathway shifts to the offshore
 466 pathway due to southward transport near Point Reyes ($25 < r < 50$ km) and direct ad-
 467 vection by the prevailing northerly wind still further north ($r > 50$ km). The northward
 468 fraction, $\bar{Q}_{northward}/\bar{Q}_{GG}$, shows a corresponding decrease for $25 < r < 70$ km; (ii) The
 469 offshore pathway also receives offshore-advected water from the southward pathway due to
 470 surface Ekman transport and possibly from the transient, directly offshore motion. This is
 471 accompanied by the decrease of $\bar{Q}_{southward}/\bar{Q}_{GG}$ for $70 < r < 150$ km. Comparing vari-

472 ations of $\bar{Q}_{northward}/\bar{Q}_{GG}$ and $\bar{Q}_{southward}/\bar{Q}_{GG}$ for $50 < r < 70$ km reveals that much of
 473 the water originally along the northward pathway is ultimately passed on to the southward
 474 pathway, with the offshore third acting as a mediator. The fact that there is no noticeable
 475 increase in the offshore transport at this distance is indicative of the tracer passing through
 476 the arcs with no flux divergence in and out of the region. The sum-total baywater transport
 477 $\bar{Q}_{total}/\bar{Q}_{GG}$ (yellow) gradually decreases towards outer arcs due to small local storage of
 478 tracer in areas between the inner arcs over this two year period.

479 The ratio of $\sum T_i/\sum T_{total}$ (dashed lines in Figure 12) reveals how dominant each path-
 480 way is through the modeled period and comparing $\sum T_i/\sum T_{total}$ to \bar{Q}_i/\bar{Q}_{GG} reveals infor-
 481 mation about the intensity of transport. For example, the fraction of southward transport,
 482 $\bar{Q}_{southward}/\bar{Q}_{GG}$ always exceeds the fraction of time the plume is dominated by southward
 483 transport, $\sum T_{southward}/\sum T_{total}$. This means that the southward pathway accounts for a
 484 larger portion of the total baywater transport in less time. In contrast, $\bar{Q}_{northward}/\bar{Q}_{GG}$ is
 485 always less than $\sum T_{northward}/\sum T_{total}$ meaning that the more frequent northward pathway
 486 accounted for less transport of plume water over the two-year period. This imbalance in
 487 transport is likely due to the coincidence of peak discharge and persistent northerly wind
 488 in Spring of 2011 (Figure 10), rather than an indication that the southward transport is
 489 somehow more efficient. The offshore pathway, having strong interaction with the two along-
 490 shore pathways, exhibits an intermediate state with a transition point $r \simeq 80$ km (where
 491 the solid and dashed green lines intersect). Performing an average across all the 30 arcs,
 492 weighted by arc radius, we are able to give the following estimates of the spatio-temporal
 493 pattern of SFB plume dispersal during 2011–2012: (i) of the two-year mean net discharge of
 494 924 m^3 , 11.1% is stored within 150 km of the Golden Gate, 35.1% is dispersed southward,
 495 29.7% is dispersed offshore (up to the shelf break), and 24.1% is dispersed northward; (ii)
 496 across the two-year time span, the discharged baywater is dispersed southward for 26.0% of
 497 the time, offshore for 31.8% of the time, and northward for 42.2% of the time.

498 5 Water Age

499 Water age has utility for estimating ventilation rates of ocean basins, inferring ocean
 500 circulation and mixing, and studying rates of biogeochemical processes (W. G. Zhang et al.,
 501 2010). In this section, we focus on the time scale associated with the spreading of the SFB
 502 plume over the northern and central California shelf. We apply the constituent-oriented age
 503 theory (Delhez et al., 1999) to the circulation of the SFB-sourced water.

5.1 The Constituent-Oriented Age Theory

According to the constituent-oriented age theory (Delhez et al., 1999), the age of a passive tracer is a time-dependent, pointwise quantity that can be obtained from the solution of two partial differential equations governing the evolution of the concentration of the passive tracer (C) and an auxiliary variable called the “mean age concentration” (α).

In this approach, each fluid parcel at position \mathbf{x} and time t is recognized to consist of constituents having different ages (i.e., times since leaving the Golden Gate). A parcel’s age concentration (i.e., the concentration of tracer with a particular age τ) is denoted $c(\mathbf{x}, t, \tau)$, where \mathbf{x} refers to the parcel position at time t . The total passive tracer concentration is calculated as the integral of the age concentration across all ages $C(\mathbf{x}, t) = \int_0^\infty c(\mathbf{x}, t, \tau) d\tau$, and the mean age concentration $\alpha(\mathbf{x}, t)$ is given by the first moment of the age concentration, $\alpha(\mathbf{x}, t) = \int_0^\infty \tau c(\mathbf{x}, t, \tau) d\tau$. The mean age, $a(\mathbf{x}, t)$, is obtained as the ratio of the mean age concentration to the total tracer concentration,

$$a(\mathbf{x}, t) = \frac{\alpha(\mathbf{x}, t)}{C(\mathbf{x}, t)}. \quad (3)$$

In this application, concentration and age tracers are introduced only at the Golden Gate and there is no production or destruction of tracer within the domain. Concentrations of a given age can be changed through advection, mixing, and aging of the tracer itself. Thus, the evolution of age concentration obeys

$$\frac{\partial c}{\partial t} = \nabla \cdot (\mathbf{u}c - \mathbf{K} \cdot \nabla c) - \frac{\partial c}{\partial \tau}. \quad (4)$$

Here, the flow velocity is given by \mathbf{u} , and \mathbf{K} represents the eddy diffusivity tensor. The final term on the right-hand side represents the aging of water within the grid cell. The integral of equation (4) with respect to τ yields an expression for the time evolution of $C(\mathbf{x}, t)$. Applying a sensible constraint on the age concentration, $\lim_{\tau \rightarrow \infty} c(t, \mathbf{x}, \tau) = 0$, one obtains

$$\frac{\partial C}{\partial t} = c(\mathbf{x}, t, \tau = 0) - \nabla \cdot (\mathbf{u}C - \mathbf{K} \cdot \nabla C). \quad (5)$$

The evolution equation for the mean age concentration $\alpha(\mathbf{x}, t)$ is obtained by multiplying equation (5) by τ and integrating in τ

$$\frac{\partial \alpha}{\partial t} = C(\mathbf{x}, t) - \nabla \cdot (\mathbf{u}\alpha - \mathbf{K} \cdot \nabla \alpha). \quad (6)$$

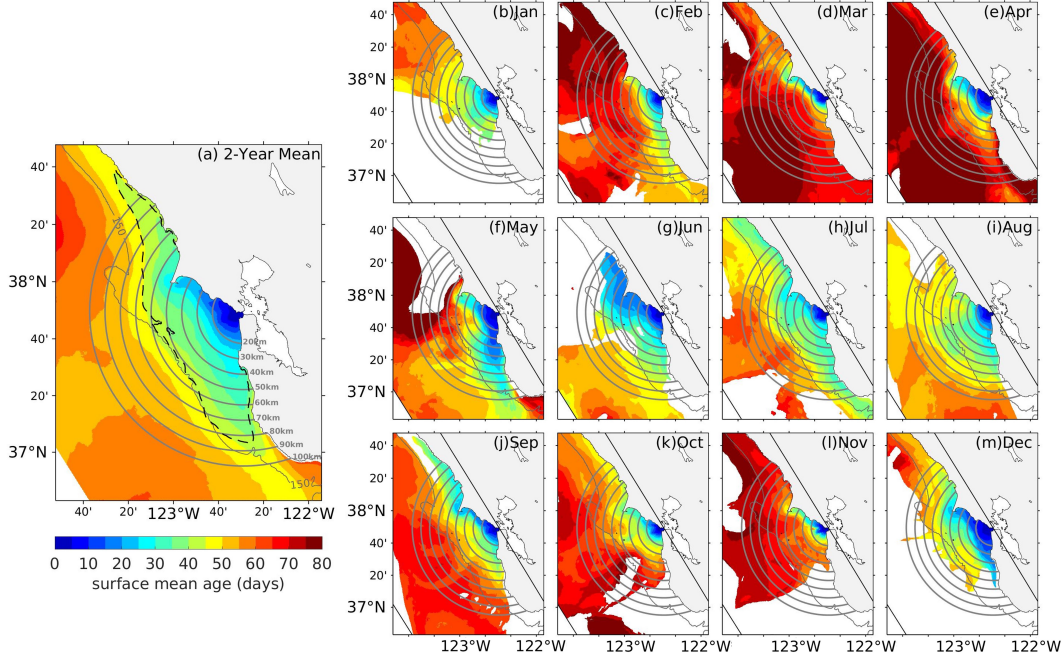


Figure 13. Surface mean age where depth-integrated passive tracer concentration $C_{VI} \geq 0.01$: (a) two-year mean; (b–m) monthly mean in the year 2012.

531 The total tracer concentration $C(\mathbf{x}, t)$ thus drives changes in mean age concentration. Con-
 532 sidering an isolated parcel in the absence of advection and diffusion, if a passive tracer is
 533 non-zero, the mean age concentration increases in time, and $\frac{da(\mathbf{x}, t)}{dt} = 1$.

534 In the present study, the first term on the right-hand side of equation (6) was added
 535 to the ROMS code, and equations (5) and (6) were solved together numerically. Here, we
 536 regard locations where the concentration is lower than 10^{-4} as being free of SFB plume
 537 water, and water age there is undefined. The initial conditions for both C and α is zero.

538 **5.2 Surface Mean Age of the SFB Plume**

539 Figure 13a shows the two-year averaged surface mean age. Water age increases rapidly
 540 with increasing radius from the Golden Gate; starting at 0 days, up to roughly 20 days at a
 541 distance of 20 km from the Golden Gate. Within the main body of the plume ($C_{VI} \geq 0.1$;
 542 encompassed by the dashed line in Figures 7b and 13a), the average surface mean age ranges
 543 from 0–45 days. The maximum value of surface mean age in the Gulf of the Farallones is
 544 around 50 days, which indicates that the SFB-sourced water is typically flushed out of
 545 the region within this time frame. Consistent with the three-pathway pattern of baywater

546 dispersal described in section 4, we see the farthest penetration of young water along the
547 coast north of the Golden Gate. For example, water with a mean age of 45 days can be
548 found 120 km up the northern coast. Water in Drakes Bay is persistently freshened as it
549 retains SFB-sourced water, and the mean age there ranges between 20–25 days. On the
550 other hand, along the southern coast, water with a mean age of 45 days only extends up
551 to 90 km from the Golden Gate. Half Moon Bay experiences slightly older water than just
552 offshore, and Monterey Bay hosts relatively old water with mean age of 55–60 days when
553 the plume travels far enough south.

554 Temporal variability is highlighted when considering monthly averaged surface mean
555 age as shown in Figures 13b–m (c.f., passive tracer concentrations in Figures 7d–o). In
556 some months, water is transported more rapidly through the Gulf, with surface mean ages
557 less than 30 days throughout much of the region (e.g., June). On the other hand, there
558 are months where water is retained for much longer time periods within the Gulf. April
559 shows the oldest average age in the Gulf of the Farallones, that is, around 60–70 days. The
560 mean age is inversely related to the baywater discharge (more rapid flushing associated with
561 stronger outflow). Mean age north of the Golden Gate decreases during northward surface
562 transport of young water directly from the Golden Gate (often associated with southerly
563 winds), and increases during southward transport (often associated with northerly winds).
564 Overall, the cross-shore distribution of surface mean age in Figure 13 echoes the baywater
565 dispersal pattern shown in Figure 7 (i.e., the portion of the southern shelf occupied by
566 young water is wider and shifted offshore more than that of the northern shelf due to the
567 differential Ekman transports).

568 **6 Summary and Discussion**

569 We conducted a study of the dispersal of the San Francisco Bay plume over the northern
570 and central California shelf. Two years (2011–2012) of high-resolution simulations were used
571 to analyze the baywater dispersal pathways and associated time scales (i.e., mean water
572 age) in terms of both mean behaviour and temporal variability. High-frequency ocean-bay
573 exchange data that are available from an existing estuarine model (SCHISM) were applied to
574 the domain’s eastern boundary at the Golden Gate through which the SFB-sourced water
575 enters the coastal ocean. A passive tracer was introduced to facilitate an unambiguous
576 measure of the baywater dispersal.

577 Tidal forcing is an important factor in driving exchange at the Golden Gate (e.g., Fram
578 et al., 2007) as well as mixing (e.g., MacCready et al., 2009, as in the Columbia River plume),
579 particularly within the estuary. Previous work has also shown that tides exert an important
580 influence at the inflow of a buoyant plume over one tidal cycle (McCabe et al., 2009) and
581 can enhance cross-shelf mixing in the absence of other forcing (e.g., Izett & Fennel, 2018a).
582 We did not carry out analysis of mixing associated with tidal bottom stresses along the shelf
583 but generally find that the plume structure is surface enhanced except for a narrow region
584 immediately outside the Golden Gate. Thus while tidal motion is critical in that vicinity,
585 plume variability is largely dominated by wind stress forcing.

586 In spite of the complex coastline of the region, the San Francisco Bay plume behaves
587 similarly to other river-sourced buoyant plumes, including idealized plumes. Upon entering
588 the ocean, the vast majority of the SFB plume is sharply differentiated from the underlying
589 shelf water. We identify three distinct transport pathways: a southward pathway that
590 extends 80 km south of the Golden Gate on average; a northward pathway that reaches as
591 far as 120 km north of the Golden Gate on average; and an offshore pathway that transiently
592 delivers baywater cross-shore, which largely ceases near the shelf break (Figure 7). The
593 natural tendency for the plume to turn north under the influence of the Coriolis force,
594 combined with northward surface currents during downwelling conditions, result in a plume
595 that is narrower and deeper in Figures 7 and 11 (e.g., Fong & Geyer, 2002; Lv et al.,
596 2020; Izett & Fennel, 2018a) compared to the southern branch which is favored during
597 upwelling conditions that result in a broader, shallower plume (as in Fong & Geyer, 2001,
598 2002). Though intra- and inter-annual variability exists, shelf waters within the Gulf of the
599 Farallones exhibit water ages typically less than 50 days from release at the Golden Gate.

600 Overall, we find similar behavior to the Columbia River plume described by Hickey
601 et al. (2005). As with our analysis, they find that a bi-directional plume is present at
602 the Columbia River outflow due to the presence of both upwelling and downwelling wind
603 conditions. The narrower northward branch of the Columbia River plume occurs roughly
604 50% of the time, which is similar to the 42% we find for the SF Bay plume. Despite its less
605 frequent occurrence (26% of the time), the southern pathway contributes most to export
606 (35.1% of total baywater) due to the coincidence of high plume discharge and northerly
607 winds in Spring 2011. Wind forcing is the dominant factor in determining the prevailing
608 direction of the plume, with a lag of three days between a weakening or reversal of winds

609 and a reversal of plume direction. This value is consistent with Hickey et al. (2005) who also
610 find a lag with wind reversal and a propagation of the plume front of roughly 35 km d^{-1} .

611 The dispersal pathways of the plume have implications for biogeochemical processes over
612 northern and central California shelf because the San Francisco Bay is a significant source of
613 nutrients, organic matter, and dissolved and suspended contaminants to the shelf, with loads
614 similar to open ocean inputs (Hurst & Bruland, 2008). The patterns of baywater dispersal
615 revealed here indicate that the destination of material transported in the San Francisco Bay
616 discharge changes rapidly on the scales of a few days, but also with longer-term seasonal
617 differences. The water age analysis echoes the pattern of tracer dispersal pathways, with
618 youngest water near the Golden Gate (<10 days old) and within the main body of the
619 plume (< 50 days on average). For river-borne material that is biologically or geochemically
620 active on time scales from a few days to months, the transport pathways and water age
621 inferred here will influence deposition, availability to the regional marine ecosystem in several
622 national marine sanctuaries (e.g., the Gulf of the Farallones NMS, the Cordell Bank NMS,
623 and the Monterey Bay NMS), as well as regions where material may be exported from the
624 San Francisco Bay by advection. When considering export timescales, a change of just
625 a few days can have a significant impact on the amount of nutrients processed locally or
626 downstream within a plume (Izett & Fennel, 2018b). Similar to the work by Kessouri et al.
627 (2021), follow-up work should use physical-biogeochemical coupled simulations to explore
628 the importance of anthropogenic nutrient loads in the California Current System, which is
629 one of the world's four major wind-driven upwelling systems.

630 **Data Availability Statement**

631 The model code and outputs of this study are available at: <https://doi.org/10.5281/zenodo.7433924>.

632 **Acknowledgments**

633 This work was funded by the San Francisco Estuary Institute (SFEI) grant #1270, the
634 California Ocean Protection Council grant #17661, the National Natural Science Foundation
635 of China (52209085), the Jiangsu Specially-Appointed Professor Program (B1203512), and
636 the Fundamental Research Funds for the Central Universities (B220201033). Computational
637 resources were provided by the Extreme Science and Engineering Discovery Environment
638 (XSEDE) through allocations TG-OCE170017 and TG-OCE030000N. We thank Zhengui
639 Wang and Fei Chai for sharing the SCHISM data of high-frequency ocean-estuary exchanges.

References

- 640
- 641 Basdurak, N. B., Largier, J. L., & Nidzieko, N. J. (2020). Modeling the dynamics of small-
 642 scale river and creek plumes in tidal waters. *Journal of Geophysical Research: Oceans*,
 643 *125*, e2019JC015737.
- 644 Brink, K. H. (1998). Deep sea forcing and exchange processes. In K. H. Brink & A. R. Robin-
 645 son (Eds.), *The global coastal ocean: process and methods* (Vol. 10, p. 151-167). Cam-
 646 bridge, MA: Harvard University Press.
- 647 Cahill, B., Schofield, O., Chant, R., Wilkin, J., Hunter, E., Glenn, S., & Bissett, P. (2008).
 648 Dynamics of turbid buoyant plumes and the feedbacks on near-shore biogeochemistry
 649 and physics. *Geophysical Research Letters*, *35*, L10605.
- 650 Carslaw, H. S., & Jaeger, J. C. (1959). *Conduction of heat in solids*. New York: Oxford
 651 University Press. (520 pp)
- 652 Castelao, R., Schofield, O., Glenn, S., Chant, R., & Kohut, J. (2008). Cross-shelf transport
 653 of freshwater on the New Jersey shelf. *Journal of Geophysical Research: Oceans*, *113*,
 654 C07017.
- 655 Chin, J. L., Ueber, E., Stauffer, P. H., & James W. Hendley II. (2001). *Beyond the*
 656 *golden gate; oceanography, geology, biology, and environmental issues in the gulf of*
 657 *the farallones* (Tech. Rep. No. 1198). USGS.
- 658 Cloern, J. E. (1996). Phytoplankton bloom dynamics in coastal ecosystems: A review with
 659 some general lessons from sustained investigation of San Francisco Bay, California.
 660 *Reviews of Geophysics*, *34*, 127-168.
- 661 Cloern, J. E., Schraga, T. S., Nejad, E., & Martin, C. (2020). Nutrient status of San
 662 Francisco Bay and its management implications. *Estuaries and Coasts*, *43*, 1299-
 663 1317.
- 664 Connolly, T. P., Hickey, B. M., Shulman, I., & Thomson, R. E. (2014). Coastal trapped
 665 waves, alongshore pressure gradients, and the California Undercurrent. *Journal of*
 666 *Physical Oceanography*, *44*(1), 319-342.
- 667 Crank, J. (1975). *The mathematics of diffusion*. London, WI: Oxford University Press.
 668 (414 pp)
- 669 Delhez, E. J. M., Campin, J., Hirst, A. C., & Deleersnijder, E. (1999). Toward a general
 670 theory of the age in ocean modeling. *Ocean Modelling*, *1*, 17-27.
- 671 Deutsch, C., Frenzel, H., McWilliams, J. C., Renault, L., Kessouri, F., Howard, E., . . . Yang,
 672 S. (2020). Biogeochemical variability in the California Current System. *bioRxiv*, *2*(10),

- 673 942565.
- 674 Egbert, G. D., & Erofeeva, S. Y. (2002). Efficient inverse modeling of barotropic ocean
675 tides. *Journal of Atmospheric and Oceanic Technology*, *19*(2), 183-204.
- 676 Fong, D. A., & Geyer, W. R. (2001). Response of a river plume during an upwelling favorable
677 wind event. *Journal of Geophysical Research: Oceans*, *106*(C1), 1067-1084.
- 678 Fong, D. A., & Geyer, W. R. (2002). The alongshore transport of freshwater in a surface-
679 trapped river plume. *Journal of Physical Oceanography*, *32*, 957-972.
- 680 Fram, J. P., Martin, M. A., & Stacey, M. T. (2007). Dispersive fluxes between the coastal
681 ocean and a semienclosed estuarine basin. *Journal of Physical Oceanography*, *37*,
682 1645-1660.
- 683 Garvine, R. W. (1999). Penetration of buoyant coastal discharge onto the continental shelf:
684 A numerical model experiment. *Journal of Physical Oceanography*, *29*, 1892-1909.
- 685 Geyer, W. R., & MacCready, P. (2014). The estuarine circulation. *Annual Review of Fluid*
686 *Mechanics*, *46*, 175-197.
- 687 Godin, G. (1972). *The analysis of tides*. Toronto: University of Toronto Press. (264 pp)
- 688 Gruber, N., Lachkar, Z., Frenzel, H., Marchesiello, P., Munnich, M., McWilliams, J., . . .
689 Plattner, G.-K. (2011). Eddy-induced reduction of biological production in eastern
690 boundary upwelling systems. *Nature Geosciences*, *4*, 787-792.
- 691 Hickey, B. M. (1998). Coastal oceanography of Western North America from the tip of
692 Baja California to Vancouver Island. In K. H. Brink & A. R. Robinson (Eds.), *The*
693 *Sea* (Vol. 11, p. 345-393). New York, NY: Wiley and Sons, Inc.
- 694 Hickey, B. M., Geier, S., Kachel, N., & MacFadyen, A. (2005). A bi-directional river plume:
695 The columbia in summer. *Continental Shelf Research*, *25*(14), 1631-1656.
- 696 Hickey, B. M., & Pola, N. E. (1983). The seasonal alongshore pressure gradient on the
697 West Coast of the United States. *Journal of Geophysical Research: Oceans*, *88*(C12),
698 7623-7633.
- 699 Horner-Devine, A. R., Hetland, R. D., & MacDonald, D. G. (2015). Mixing and transport
700 in coastal river plumes. *Annual Review of Fluid Mechanics*, *47*, 569-594.
- 701 Hurst, M. P., & Bruland, K. W. (2008). The effects of the San Francisco Bay plume on
702 tracer metal and nutrient distributions in the Gulf of the Farallones. *Geochimica et*
703 *Cosmochimica Acta*, *72*, 395-411.
- 704 Huyer, A. (1983). Coastal upwelling in the california current system. *Progress in Oceanog-*
705 *raphy*, *12*(3), 259-284.

- 706 Izett, J. G., & Fennel, K. (2018a). Estimating the cross-shelf export of riverine materials:
707 Part 1. general relationships from an idealized numerical model. *Global Biogeochemical*
708 *Cycles*, *32*(2), 160-175.
- 709 Izett, J. G., & Fennel, K. (2018b). Estimating the cross-shelf export of riverine materials:
710 Part 2. estimates of global freshwater and nutrient export. *Global Biogeochemical*
711 *Cycles*, *32*(2), 176-186.
- 712 Jacox, M. G., Edwards, C. A., Hazen, E. L., & Bograd, S. J. (2018). Coastal upwelling
713 revisited: Ekman, Bakun, and improved upwelling indices for the U.S. West Coast.
714 *Journal of Geophysical Research: Oceans*, *123*, 7332-7350.
- 715 Kaplan, D. M., & Largier, J. (2006). HF radar-derived origin and destination of surface
716 waters off Bodega Bay, California. *Deep Sea Research Part II: Topical Studies in*
717 *Oceanography*, *53*, 2906-2930.
- 718 Kessouri, F., Bianchi, D., Renault, L., McWilliams, J. C., Frenzel, H., & Deutsch,
719 C. A. (2020). Submesoscale currents modulate the seasonal cycle of nutrients and
720 productivity in the California Current System. *Global Biogeochemical Cycles*, *34*,
721 e2020GB006578.
- 722 Kessouri, F., McLaughlin, K., Sutula, M., Bianchi, D., Ho, M., McWilliams, J. C., ...
723 Leinweber, A. (2020). Configuration and validation of an oceanic physical and biogeo-
724 chemical model to investigate coastal eutrophication in the Southern California Bight.
725 *Earth and Space Science Open Archive*, 1-62.
- 726 Kessouri, F., McWilliams, J. C., Bianchi, D., Sutula, M., Renault, L., Deutsch, C., ...
727 Weisberg, S. B. (2021). Coastal eutrophication drives acidification, oxygen loss, and
728 ecosystem change in a major oceanic upwelling system. *Proceedings of the National*
729 *Academy of Sciences*, *118*(21), e2018856118.
- 730 Large, W. G., McWilliams, J. C., & Doney, S. C. (1994). Oceanic vertical mixing: A review
731 and a model with a nonlocal buoyancy layer parameterization. *Reviews of Geophysics*,
732 *32*(4), 363-403.
- 733 Lentz, S. (2004). The response of buoyant coastal plumes to upwelling-favorable winds.
734 *Journal of Physical Oceanography*, *34*, 2458-2469.
- 735 Lentz, S. J. (1987). A description of the 1981 and 1982 spring transition over the northern
736 California shelf. *Journal of Geophysical Research: Oceans*, *92*, 1545-1567.
- 737 Lv, R., Cheng, P., & Gan, J. (2020). Adjustment of river plume fronts during downwelling-
738 favorable wind events. *Continental Shelf Research*, *202*, 104143.

- 739 MacCready, P., Banas, N. S., Hickey, B. M., Dever, E. P., & Liu, Y. (2009). A model study
740 of tide- and wind-induced mixing in the columbia river estuary and plume. *Continental*
741 *Shelf Research*, *29*(1), 278-291.
- 742 Marchesiello, P., McWilliams, J. C., & Shchepetkin, A. (2001). Open boundary conditions
743 for long-term integration of regional oceanic models. *Ocean Modelling*, *3*(1-2), 1-20.
- 744 Marchesiello, P., McWilliams, J. C., & Shchepetkin, A. (2003). Equilibrium structure and
745 dynamics of the California Current System. *Journal of Physical Oceanography*, *33*,
746 753-783.
- 747 Mason, E., Molemaker, J., Shchepetkin, A. F., Colas, F., McWilliams, J. C., & Sangra, P.
748 (2010). Procedures for offline grid nesting in regional ocean models. *Ocean Modelling*,
749 *35*(1-2), 1-15.
- 750 McCabe, R. M., MacCready, P., & Hickey, B. M. (2009). Ebb-tide dynamics and spreading
751 of a large river plume. *Journal of Physical Oceanography*, *39*(11), 2839 - 2856.
- 752 Reid, J. L., & Schwartzlose, R. A. (1962). Direct measurements of the Davidson Current
753 off central California. *Journal of Geophysical Research: Oceans*, *67*(6), 2491-2497.
- 754 Renault, L., Hall, A., & McWilliams, J. C. (2016). Orographic shaping of u.s. west coast
755 wind profiles during the upwelling season. *Climate Dynamics*, *46*, 273-289.
- 756 Renault, L., McWilliams, J. C., Jousse, A., Deutsch, C., Frenzel, H., Kessouri, F., & Chen,
757 R. (2020). The physical structure and behavior of the California Current System.
758 *bioRxiv*, *2*(10), 942730.
- 759 Renault, L., Molemaker, M. L., McWilliams, J. C., Shchepetkin, A. F., Lemarie, F., Chelton,
760 D., ... Hall, A. (2016). Modulation of wind work by oceanic current interaction with
761 the atmosphere. *Journal of Physical Oceanography*, *46*, 1685-1704.
- 762 Sharples, J., Middelburg, J. J., Fennel, K., & Jickells, T. D. (2017). What proportion of
763 riverine nutrients reaches the open ocean? *Global Biogeochemical Cycles*, *31*.
- 764 Shchepetkin, A. F. (2015). An adaptive, courant-number-dependent implicit scheme for
765 vertical advection in oceanic modeling. *Ocean Modelling*, *91*, 38-69.
- 766 Shchepetkin, A. F., & McWilliams, J. C. (2005). The Regional Oceanic Modeling Sys-
767 tem (ROMS): A split-explicit, free-surface, topography-following-coordinate oceanic
768 model. *Ocean Modelling*, *9*(4), 347-404.
- 769 Shchepetkin, A. F., & McWilliams, J. C. (2009). Correction and commentary for “Ocean
770 forecasting in terrain-following coordinates: Formulation and skill assessment of the
771 regional ocean modeling system” by Haidvogel et al. *J. Comp. Phys.* *227*, pp. 3595-

- 772 3624. *Journal of Computational Physics*, 228(24), 8985-9000.
- 773 Trenberth, K. E., Smith, L., Qian, T., Dai, A., & Fasullo, J. (2007). Estimates of the global
774 water budget and its annual cycle using observational and model data. *Journal of*
775 *Hydrometeorology*, 8, 758-769.
- 776 Wang, Z., Chai, F., Dugdale, R., Liu, Q., Xue, H., Wilkerson, F., . . . Zhang, H. (2020). The
777 interannual variabilities of chlorophyll and nutrients in San Francisco Bay: a modeling
778 study. *Ocean Dynamics*, 70, 1169-1186.
- 779 Whitney, M. M., & Garvine, R. W. (2006). Simulating the Delaware Bay buoyant outflow:
780 Comparison with observations. *Journal of Physical Oceanography*, 36, 3-21.
- 781 Xiao, C., Zhang, W., & Chen, Y. (2021). Impact of shelf valleys on the spread of surface-
782 trapped river plumes. *Journal of Physical Oceanography*, 51, 247-266.
- 783 Zhang, W. G., Wilkin, J. L., & Schofield, O. M. E. (2010). Simulation of water age and
784 residence time in New York Bight. *Journal of Physical Oceanography*, 40, 965-982.
- 785 Zhang, Y., & Baptista, A. M. (2008). SFLFE: A semi-implicit Eulerian-Lagrangian finite-
786 element model for cross-scale ocean circulation. *Ocean Modelling*, 21(3-4), 71-96.
- 787 Zhang, Y., Ye, F., Stanev, E. V., & Grashorn, S. (2016). Seamless cross-scale modeling
788 with SCHISM. *Ocean Modelling*, 102, 64-81.
- 789 Zhou, J., & Stacey, M. T. (2020). Residual sediment transport in tidally energetic estuarine
790 channels with lateral bathymetric variation. *Journal of Geophysical Research: Oceans*,
791 125, e2020JC016140.
- 792 Zhou, J., Stacey, M. T., Holleman, R. C., Nuss, E., & Senn, D. B. (2020). Numerical
793 investigation of baroclinic channel-shoal interaction in partially stratified estuaries.
794 *Journal of Geophysical Research: Oceans*, 125, e2020JC016135.

Modeling the Dispersal of the San Francisco Bay Plume over the Northern and Central California Shelf

Jian Zhou^{1,2,3}, Jonathan G. Izett², Christopher A. Edwards², Pierre Damien³,
Fayçal Kessouri^{3,4}, and James C. McWilliams³

¹State Key Laboratory of Hydrology-Water Resources and Hydraulic Engineering, Hohai University,
Nanjing, Jiangsu, China

²Department of Ocean Sciences, University of California, Santa Cruz, CA, USA

³Department of Atmospheric and Oceanic Sciences, University of California, Los Angeles, CA, USA

⁴Biogeochemistry Department, Southern California Coastal Water Research Project, Costa Mesa, CA,
USA

Key Points:

- Three distinct dispersal pathways of San Francisco Bay plume are identified: southward, northward, and offshore
- Zone of impact of the northern plume is farther along-shore, narrower cross-shore, and vertically deeper compared to the southern branch
- Surface water typically spends less than 50 days in the Gulf of the Farallones after entering via the Golden Gate

Corresponding author: Jian Zhou, jzhou@hhu.edu.cn

Abstract

High-resolution simulations by the Regional Ocean Modeling System (ROMS) were used to investigate the dispersal of the San Francisco Bay (SFB) plume over the northern-central California continental shelf during the period of 2011 to 2012. The modeled bulk dynamics of surface currents and state variables showed many similarities to corresponding observations. After entering the Pacific Ocean through the Golden Gate, the SFB plume is dispersed across the shelf via three pathways: (i) along the southern coast towards Monterey Bay, (ii) along the northern coast towards Point Arena, and (iii) an offshore pathway restricted within the shelf break. On the two-year mean timescale, the along-shore zone of impact of the northward-dispersed plume is about 1.5 times longer than that of the southern branch. Due to the opposite surface Ekman transports induced by the northerly or southerly winds, the southern plume branch occupies a broader cross-shore extent, roughly twice as wide as the northern branch which extends roughly two times deeper due to coastal downwelling. Besides these mean characteristics, the SFB plume dispersal also shows considerable temporal variability in response to various forcings, with wind and surface-current forcing most strongly related to the dispersing direction. Applying constituent-oriented age theory, we determine that it can be as long as 50 days since the SFB plume was last in contact with SFB before being flushed away from the Gulf of the Farallones. This study sheds light on the transport and fate of SFB plume and its impact zone with implications for California's marine ecosystems.

Plain Language Summary

San Francisco Bay (SFB) is the largest estuary on the U.S. West Coast, situated in a highly urbanized region impacted by agricultural, industrial, and commercial wastes. As water exits the SFB through the narrow Golden Gate strait and meets the Pacific Ocean currents, it forms the SFB Plume: a layer of low-salinity water that advances over the denser seawater. Understanding how SFB plume and the nutrients, phytoplankton, and contaminants it contains are distributed in the coastal ocean is crucial for the ecosystem management of a network of National Marine Sanctuaries. This study uses three-dimensional realistic numerical simulations to explore the transport of SFB plume over the northern-central California continental shelf. We focus on the different pathways along which the SFB plume moves and the respective zones of impact in response to various atmospheric and oceanic forcings (e.g., wind and river discharge). A timescale analysis reveals that SFB plume is

50 typically flushed out of the Gulf of the Farallones within 50 days since it leaves the Golden
51 Gate. Our study sheds light on how the anthropologically modulated SFB plume may in-
52 fluence the highly dynamic marine ecosystem off the U.S. West Coast, which supports one
53 of the world’s most productive fisheries.

54 **1 Introduction**

55 Rivers carry more than one-third of land-based precipitation to the ocean (Trenberth
56 et al., 2007), channeling large freshwater fluxes through narrow outlets along the coast.
57 The impact of the terrigenous material carried by the river water into ecologically sensitive
58 coastal waters depends strongly on physical processes that transport and transform buoyant
59 freshwater in the region around the river mouth as it merges with deeper, salty ocean waters.
60 In particular, the dilution rates and along-shore transport rates of river-borne material
61 are determined by a suite of processes, including stratified-shear mixing, frontal processes,
62 geostrophic transport, and wind forcing (Whitney & Garvine, 2006; Horner-Devine et al.,
63 2015; Basdurak et al., 2020; Xiao et al., 2021). In the coastal ocean, these discharges
64 form river plumes, which are distinct regions where water properties and dynamics are
65 significantly influenced by the riverine freshwater. The distinguishing dynamical feature of
66 a river plume is the horizontal advection of freshwater from the river mouth that defines
67 the shape and character of the plume. The associated dispersal pathway of a river plume
68 depends on outflow angle (Garvine, 1999), wind forcing (Fong & Geyer, 2001; S. Lentz,
69 2004), ambient current (Fong & Geyer, 2002), and latitude (Sharples et al., 2017; Izett &
70 Fennel, 2018a). Given the temporal variation of some forcing, freshwater pathways are often
71 highly mobile, and the unsteady freshwater transport pathways have important ecological
72 implications related to contaminant, larval, and nutrient transport (e.g., Cahill et al., 2008;
73 Kessouri, McLaughlin, et al., 2020).

74 The San Francisco Bay (SFB) is the largest estuary on the west coast of North America.
75 Its watershed extends from the ridgeline of the Sierra Nevada mountains to the strait of the
76 Golden Gate. SFB has been a focus of research by the U.S. Geological Survey (USGS)
77 since 1969 to learn how estuaries respond to hydroclimatic and human disturbances such as
78 nutrient enrichment (Cloern et al., 2020). The formation of the SFB plume is due to mixing
79 of coastal seawater that has entered the bay on flood tides and incoming freshwater from the
80 Sacramento and San Joaquin Rivers, prior to returning to the ocean as the SFB plume on
81 the ebb tide (Fram et al., 2007). The supply of coastal seawater into the bay far exceeds the

82 average river input, resulting in an SFB plume that has a relatively high salinity compared
83 to a typical river plume. Upon entering coastal waters, the plume is influenced by prevailing
84 winds and near surface currents north, west, or south over the relatively broad continental
85 shelf (S. J. Lentz, 1987). The chemical constituents of the SFB plume differ from the river
86 and coastal seawater entering the bay because the saline estuary has its own internal cycling
87 of nutrients that is largely driven by anthropogenic inputs within the estuary (Cloern, 1996;
88 Wang et al., 2020). Characterizing the plume’s dispersal is of fundamental importance for
89 understanding any influence of San Francisco Bay on coastal biogeochemical processes in an
90 ecologically sensitive region (Chin et al., 2001) that includes a network of National Marine
91 Sanctuaries (NMSs) such as the Greater Farallones NMS, the Cordell Bank NMS, and the
92 Monterey Bay NMS. The Gulf of the Farallones is loosely indicated in Figure 3, covering the
93 region on the shelf from Point Reyes in the north to Pedro Point south of the Golden Gate,
94 though the boundaries of the NMS extend further north. For a map of the NMSs outside the
95 Golden Gate, please refer to <https://farallones.noaa.gov/gallery/maps.html>. Further
96 place names used in the text are highlighted in Figure 12.

97 The SFB plume enters into the California Current System (CCS), an Eastern Boundary
98 Upwelling System (Huyer, 1983; Hickey, 1998; Jacox et al., 2018; Renault et al., 2020). In the
99 central portion of the CCS during spring/summer, predominantly equatorward, along-shore
100 winds induce offshore Ekman transport and coastal upwelling, drawing nutrient-rich water
101 from depth; downwelling is driven by poleward along-shore winds that result in onshore
102 Ekman transport (e.g., Marchesiello et al., 2003). To date, little is known about the levels
103 and spatio-temporal patterns of SFB plume dispersal within the Gulf of Farallones and
104 further afield in the context of complex oceanic circulations along the U. S. West Coast
105 (Kaplan & Largier, 2006; Hurst & Bruland, 2008). As such, the mechanisms that drive
106 SFB plume dispersal on the shelf and its subsequent fate in the coastal ocean remains
107 unclear. Furthermore, the SFB plume has high levels of nutrients, phytoplankton, dissolved
108 organic matter, and contaminants (Wang et al., 2020), which may be similar to upwelled
109 concentrations (Hurst & Bruland, 2008).

110 In this study, we numerically investigate the dispersal pathways of the SFB plume over
111 the northern and central California shelf in the period of 2011–2012. A downscaled Regional
112 Ocean Modeling System (ROMS) configuration was established, scaling from a 4-km hori-
113 zontal resolution configuration spanning the entire CCS (Renault et al., 2020; Deutsch et al.,
114 2020), to a 1-km resolution grid covering much of the California coast (Kessouri, Bianchi,

115 et al., 2020), and finally to a 0.3-km grid along the portions of the northern and central
116 California coast centered around the San Francisco Bay (this study). The 0.3-km ROMS
117 grid was coupled with high-frequency ocean-estuary exchanges derived from a well-validated
118 SFB-focused modeling study (Wang et al., 2020) using the Semi-implicit Cross-scale Hy-
119 droscience Integrated System Model (SCHISM). The main objectives are to characterize
120 the shelf-wide spreading of SFB-sourced water discharged from the Golden Gate, and to
121 describe the mean characteristics and temporal variability of its dispersal pathways. We
122 will address the following two major concerns regarding the spatio-temporal pattern of the
123 SFB plume dispersal: (i) how is the net baywater effluent dispersed in the coastal ocean
124 along the various pathways? and (ii) how sustained are periods dominated by any given
125 pathway throughout the investigated time span? This paper lays groundwork for coupled
126 physical-biogeochemical investigations of anthropogenic nutrient discharges in support of
127 San Francisco Bay Nutrient Management Strategy ([https://sfbaynutrients.sfei.org/
128 books/nutrient-management-strategy-san-francisco-bay](https://sfbaynutrients.sfei.org/books/nutrient-management-strategy-san-francisco-bay)).

129 **2 Model Configuration**

130 **2.1 Oceanic Configuration**

131 The Regional Ocean Modeling System, ROMS (Shchepetkin & McWilliams, 2005;
132 Shchepetkin, 2015), is used for the ocean circulation simulations. ROMS is a primitive-
133 equation, hydrostatic, terrain-following oceanic model that allows high-resolution simula-
134 tions in shallow shelf seas. It contains state-of-art numerical algorithms that provide an
135 accurate and stable representation of physical processes down to scales of tens of meters,
136 and allows for multi-level offline downscaling of higher-resolution subdomains within larger
137 domains. Vertical mixing in the boundary layers is represented by a K-profile parameteri-
138 zation (Large et al., 1994).

139 The U.S. hindcast model (Figure 1a) has been successfully run over two decades at 4-km
140 (L0 domain) and 1-km (L1 domain) horizontal resolutions using high-resolution spatial and
141 temporal atmospheric forcing that represents the effects of near-coast wind stress changes,
142 current feedback on the surface stress, and high-frequency wind fluctuations (Renault, Hall,
143 & McWilliams, 2016; Renault, Molemaker, et al., 2016). The L0 simulation was initialized
144 and forced at the open boundaries by a pre-existing northeast Pacific-wide ROMS solution at
145 12-km resolution (Renault et al., 2020), which was initialized and forced on the boundaries

146 by the global model Mercator Glorys2V3 (<http://www.myocean.eu>). The L0 simulation
 147 was run for the period 1995-2017 after a spin-up of 2 years. The L1 simulation was then
 148 initialized and forced by the L0 model, starting in October 1996 and ending in December
 149 2017. Readers are referred to Renault et al. (2020), Deutsch et al. (2020), and Kessouri,
 150 Bianchi, et al. (2020) for the details of 1-km and 4-km model setups and boundary forcings.

151 Forced at the western, southern, and northern boundaries and initialized by the L1
 152 solution, this study investigates the L2 domain with a nominal resolution of 0.3 km ($450 \times$
 153 1200 horizontal cells in total) to capture submesoscale processes, focusing on portions of
 154 the northern and central California coast centered around the San Francisco Bay (Figure
 155 1a). The offline downscaling is based on the Orlanski scheme for the baroclinic mode
 156 (Marchesiello et al., 2001) and a modified Flather scheme for the barotropic mode (Mason
 157 et al., 2010). The model domain extends along a 400-km stretch of the coast (spanning
 158 from Ragged Point in the south to Point Arena in the north), and about 150 km offshore.
 159 The bathymetry data were acquired from the General Bathymetric Chart of the Oceans
 160 (GEBCO_2019) with 15 arc-second resolution. The grid has 60 σ -coordinate vertical levels
 161 with stretching parameters of $\theta_s = 6$, $\theta_b = 3$, and $h_c = 250$ m (Shchepetkin & McWilliams,
 162 2009). The L2 domain is tidally forced by adding the TPXO9-atlas barotropic tides (Egbert
 163 & Erofeeva, 2002) to the L1 forcing at the northern, western, and southern boundaries. The
 164 first 10 constituents are phased with the tide-resolving eastern boundary forcing from the
 165 SCHISM model (i.e., at the Golden Gate).

166 2.2 Ocean-Estuary Coupling

167 A portion of the eastern boundary of the L2 domain is forced at the Golden Gate by
 168 high-frequency (two-hourly) output from a well-validated SFB-focused modeling study over
 169 the 10-year period of 2005–2014 (Wang et al., 2020, see Figure 1b) using the Semi-implicit
 170 Cross-scale Hydroscience Integrated System Model (SCHISM). SCHISM is an open-source
 171 community model based on unstructured grids designed for seamless simulation of three-
 172 dimensional baroclinic circulation across creek-lake-estuary-shelf-ocean scales (Y. Zhang &
 173 Baptista, 2008; Y. Zhang et al., 2016). The 3D model output of momentum, temperature,
 174 and salinity across the Golden Gate in the SCHISM model (yellow line in Figure 1b) were
 175 extracted and offline coupled with the ROMS model. A major challenge was that the ROMS
 176 (structured grid) and SCHISM (unstructured grid) models differ in the bathymetry across
 177 the Golden Gate due to different horizontal and vertical resolutions. Therefore, momentum

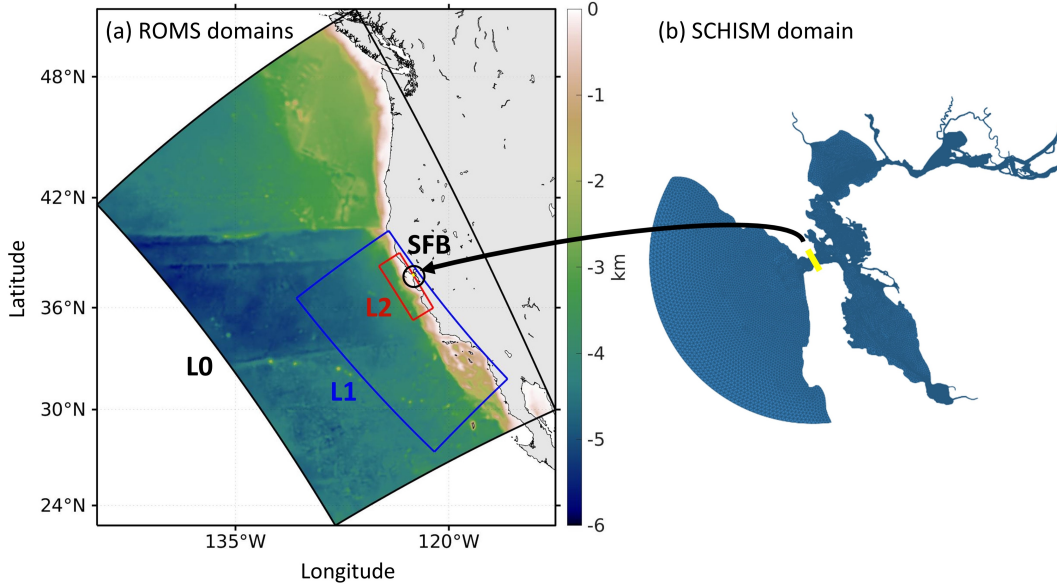


Figure 1. Model configuration: (a) ROMS nested domains; (b) SCHISM domain by Wang et al. (2020). In (a), continuous colors represent bathymetry along the U.S. West Coast and discrete rectangular perimeters indicate the triple grid nesting configuration. The black, blue, and red boxes show the L0, L1, and L2 domains with horizontal resolutions of 4 km, 1 km, and 0.3 km (the present study), respectively. The innermost circle in (a) corresponds to the estuary-focused domain in (b). The yellow line in (b) indicates the cross section from which 3D momentum, temperature, and salinity are extracted to force the eastern boundary of the L2 domain in (a).

178 and tracer concentrations were re-constructed as being laterally uniform while preserving
 179 their vertical structures, which we consider to be more important to capture the key features
 180 of ocean-estuary exchange flows at such a narrow strait. Due to the different average sea
 181 levels between models, the sea surface height at every location of the eastern boundary
 182 was forced as $\zeta = \bar{\zeta}_{\text{ROMS, no SFB-forcing}} + \zeta'_{\text{SCHISM}}$, where $\bar{\zeta}_{\text{ROMS, no SFB-forcing}}$ refers to the
 183 mean sea surface height in ROMS simulations without SFB-forcing (i.e., a closed eastern
 184 boundary condition), and ζ'_{SCHISM} represents sea surface height anomalies in the SCHISM
 185 model.

186 To avoid the ambiguity of reference salinity for ocean water in the coastal ocean (e.g.,
 187 Castela et al., 2008) and also to isolate the San Francisco Bay plume from other sources of
 188 fresh water in the model, a passive, conservative tracer with unit concentration was intro-
 189 duced at the Golden Gate. Following the simulated passive tracer concentration gives an
 190 unambiguous measure, anywhere in the model domain, of the volume fraction of water con-

191 tributed by the SFB outflow, hereafter referred to as “baywater”. The model was initialized
192 with zero baywater concentration everywhere outside of the Golden Gate.

193 As described in section 2.1, an Orlanski scheme was used for 3D temperature and
194 salinity on the eastern boundary, while the clamped open boundary conditions was used for
195 3D momentum. This approach seeks discharge volume consistency with the SCHISM model,
196 as it has been validated against measurements of major river runoffs (including Sacramento
197 River and San Joaquin River) by the California Department of Water Resources (DWR).

198 The model was integrated with a baroclinic time step of $dt = 30$ seconds. Model fields
199 were saved as sequential two-hour averages in order to achieve an accurate calculation of
200 the residual baywater flux which may be dominated by the tidal pumping flux in tidally
201 energetic estuaries and coastal seas (Fram et al., 2007; Zhou et al., 2020; Zhou & Stacey,
202 2020). The L2 simulation was run from January 2011 to December 2012. Upon investigation,
203 remnant coastal freshwater inherited from the L1 solution (where river runoff was included
204 as surface precipitation) is completely dispersed in the L2 simulation on the order of 1–2
205 months, consistent with the results in section 5 where the mean water age in the Gulf of
206 Farallones is generally less than 50 days. Given this rapid flushing, no spin-up period for
207 the passive tracer is considered. As a verification, shifting the average time window forward
208 by 2 months (i.e., from March 2011 to February 2013; not shown) has little effect on the
209 long-term pattern of baywater dispersal.

210 **3 Model Evaluation**

211 Before proceeding to the analysis of the simulation results, we evaluate the model to
212 establish that the modeled ocean hydrodynamics has acceptable fidelity with respect to rel-
213 evant observations. We focus on the L2 domain, as the L0 and L1 domains were previously
214 validated against available observations (Renault et al., 2020). Though discrepancies be-
215 tween the model and data exist, the model-data comparison for various fields shows good
216 overall representation of features of the bulk dynamics of surface currents and state variables.
217 Our goal is to demonstrate that the model is valid for the statistical average simulation of
218 baywater spreading in ocean water off the central California coast. We note that there has
219 been no assimilation of satellite or other data in these simulations.

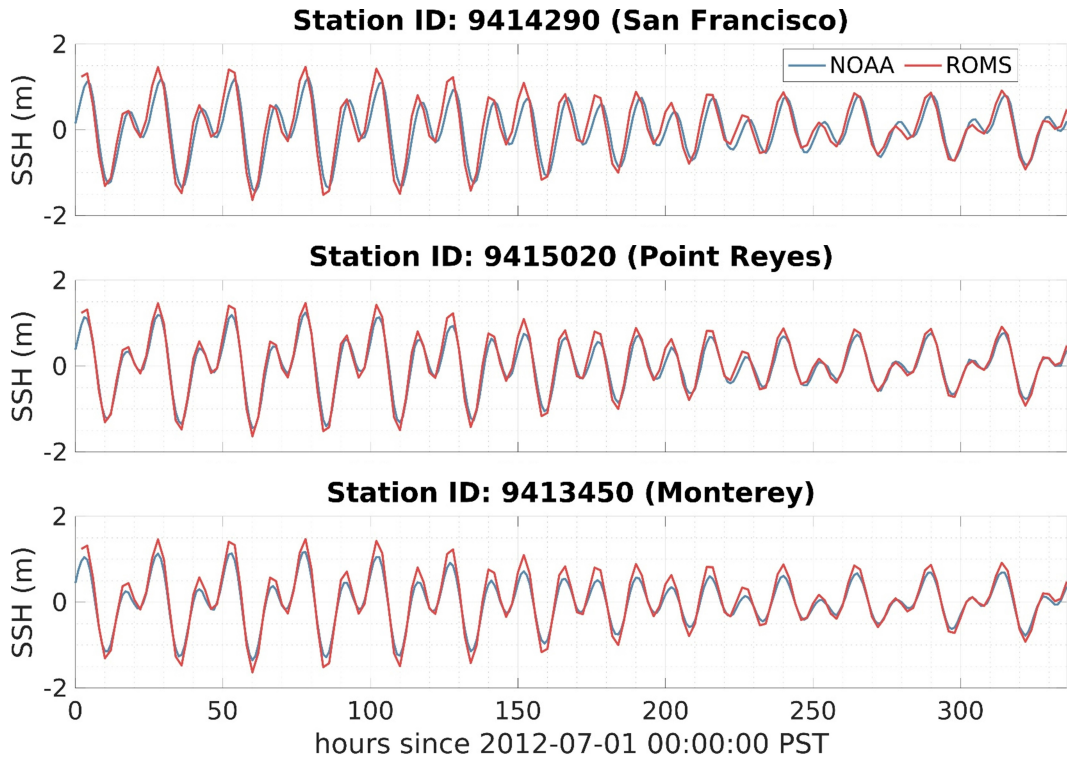


Figure 2. Comparison of modeled and observed sea surface height time-series at three representative locations (blue lines: NOAA tidal gauge measurements; red lines: ROMS simulations). Data during the first two weeks of July 2012 are shown for demonstration.

220 3.1 NOAA Tidal Gauge Measurements

221 The National Oceanic and Atmospheric Administration (NOAA) provides hourly wa-
 222 ter level information at various locations along the U.S. coast ([https://tidesandcurrents](https://tidesandcurrents.noaa.gov/)
 223 [.noaa.gov/](https://tidesandcurrents.noaa.gov/)), with three tide gauge stations within our model domain: 9414290 (San Fran-
 224 cisco), 9415020 (Point Reyes), and 9413450 (Monterey). The modeled sea surface height is
 225 compared with NOAA measurements in Figure 2 for two weeks in July 2012. The model
 226 agrees well with the observations, with root-mean-square deviations (RMSD) between the
 227 model and observation throughout 2011–2012 of 0.318 m, 0.238 m, and 0.234 m for stations
 228 9414290 (San Francisco), 9415020 (Point Reyes), and 9413450 (Monterey), respectively.

229 3.2 High-Frequency Radar Data of Surface Current

230 The land-based HF Radar Network (HFRNet; [https://hfrnet-tds.ucsd.edu/thredds/](https://hfrnet-tds.ucsd.edu/thredds/catalog.html)
 231 [catalog.html](https://hfrnet-tds.ucsd.edu/thredds/catalog.html)) was developed to measure the speed and direction of ocean surface currents

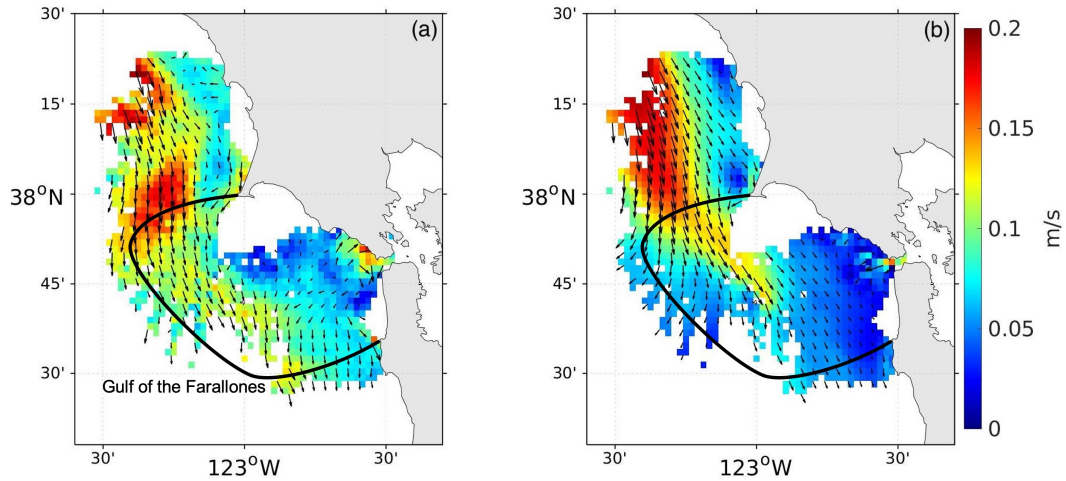


Figure 3. Comparison of annual-mean surface currents for the year 2012 at the outflow of the Golden Gate, including the Gulf of the Farallones (indicated with black outline): (a) observed (HFR); (b) modeled. Color represents current magnitude, and scaled arrows indicate the direction. Note that the model results (0.3 km-resolution) are remapped onto the HFR grid (2 km-resolution) to aid comparison.

232 in near real-time. HFR data covering the U.S. West Coast (including the Central California
 233 Coast centered around the San Francisco Bay) first became available in 2012.

234 Figure 3 compares the annual mean surface currents between HFR data and the model
 235 in 2012. The observed data are plotted only at locations where data availability in time
 236 exceeds 70%; modeled results are plotted at the same locations for ease of comparison. Over
 237 this time period, both observations and model show a predominantly southward mean flow.
 238 Surface currents are generally weak close to the coast, strengthening offshore. A tongue-
 239 shaped zone of strong southward flow north of Point Reyes is successfully reproduced, with
 240 the model showing a somewhat more continuous pattern. Discrepancies between the model
 241 and data also exist. In particular, there exists a difference in mean flow within the Gulf of
 242 the Farallones. The model shows weak alongshore flow whereas the observations indicate
 243 stronger offshore flow. Discrepancies between observations and the model may in part
 244 result from the differing data availability across the average period: the model has full
 245 temporal coverage across the investigated period, while at some locations there are only
 246 limited HFR data available to contribute to the annual mean current. This is especially
 247 the case immediately outside of the Golden Gate where sufficiently high temporal coverage
 248 is needed to obtain averaged currents on tidal and spring-neap timescales. Meanwhile,

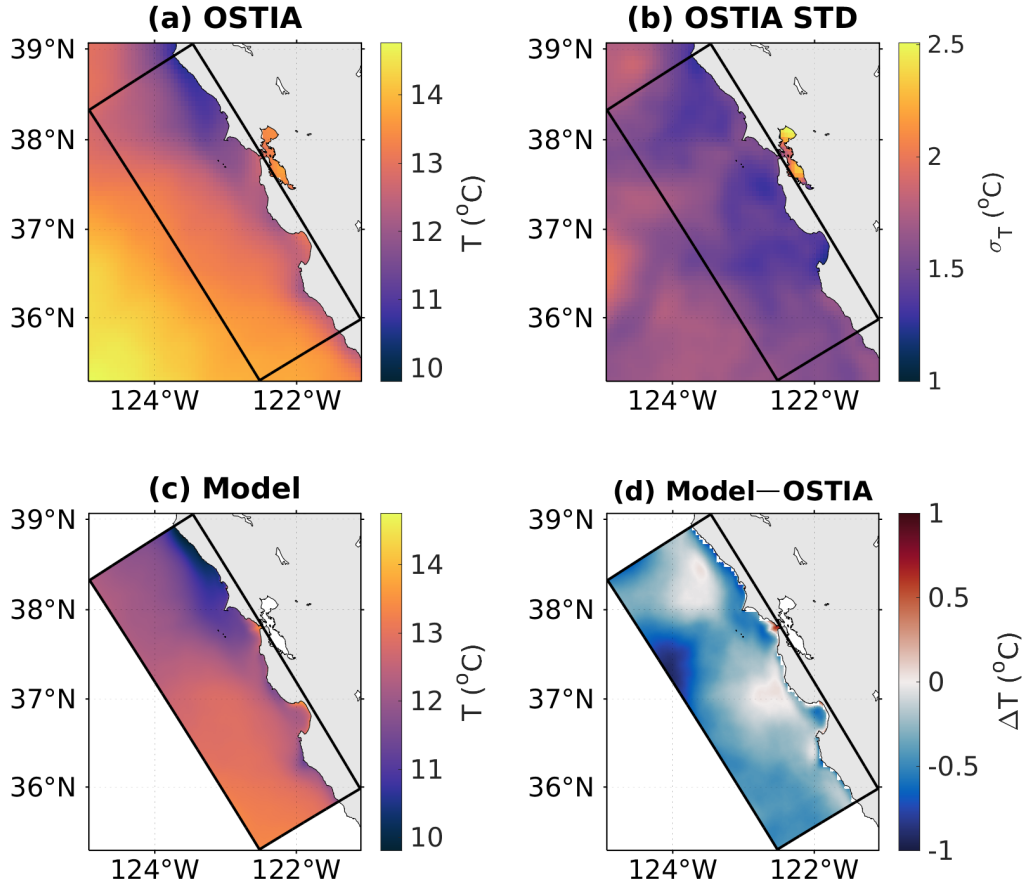


Figure 4. Comparison of observed and modeled 2-year mean sea surface temperature: (a) OSTIA Level-4 product; (b) standard deviation of OSTIA data; (c) modeled SST; (d) model bias ($SST_{\text{model}} - SST_{\text{obs}}$).

249 different spatial resolutions may also contribute to the model-data discrepancy (i.e. 2 km in
 250 the HFR data and 0.3 km in the model). Despite the differences, the general patterns are
 251 well represented and yield a Pearson correlation coefficient of 0.63.

252 3.3 Remote-Sensing Observations of Sea Surface Temperature

253 Sea surface temperature (SST) is one measure of ocean temperature that is readily
 254 available for model evaluation in satellite observations. We compare the GHRSSST Level 4
 255 OSTIA SST product with a spatial resolution of $0.05^\circ \times 0.05^\circ$ ([https://podaac.jpl.nasa](https://podaac.jpl.nasa.gov/dataset/OSTIA-UKMO-L4-GLOB-v2.0)
 256 [.gov/dataset/OSTIA-UKMO-L4-GLOB-v2.0](https://podaac.jpl.nasa.gov/dataset/OSTIA-UKMO-L4-GLOB-v2.0)) to the model results. As shown in Figure 4, the

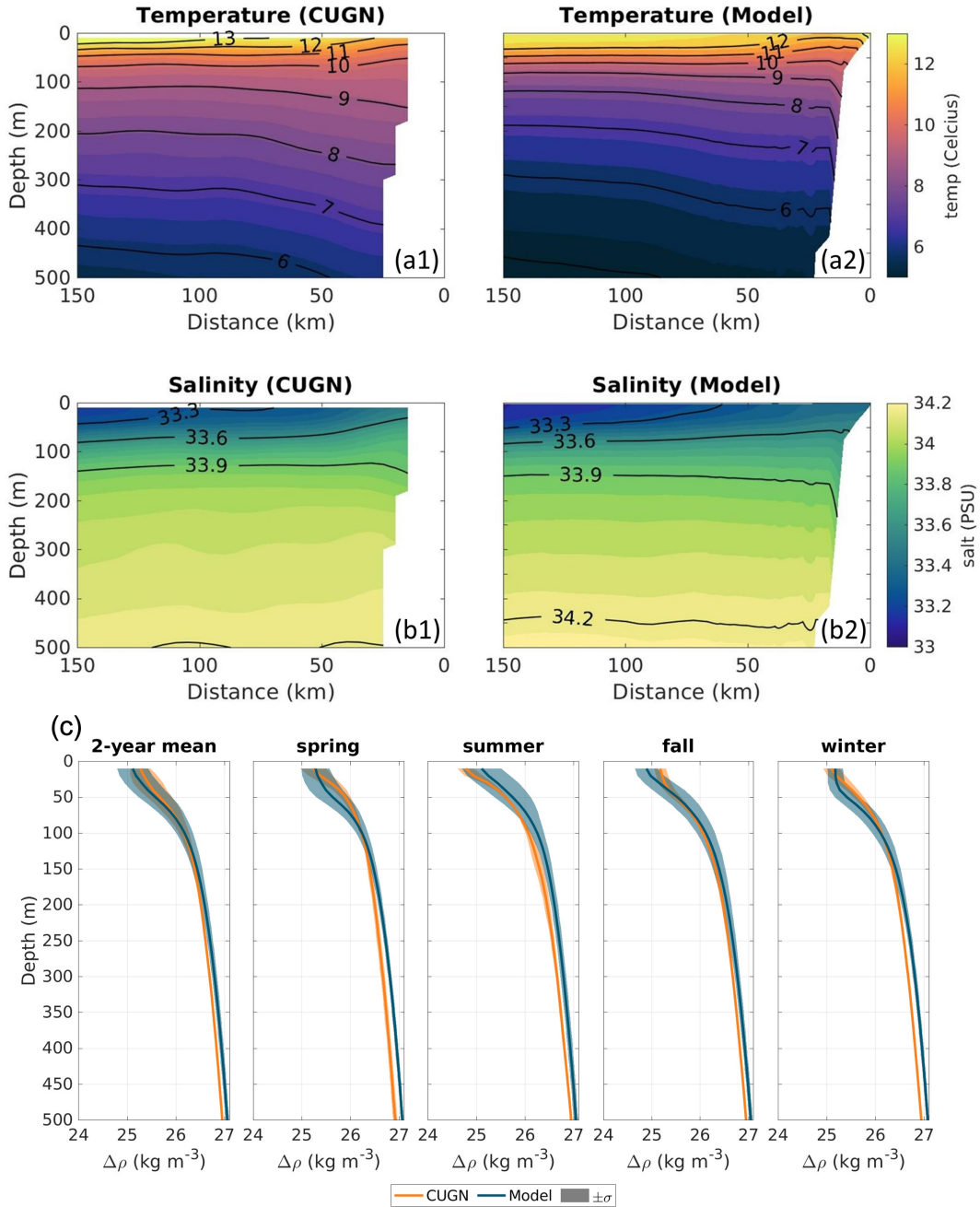


Figure 5. Model evaluation using CUGN data: (a) cross-shore contours of two-year mean (2011–2012) water temperature; (b) cross-shore contours of two-year mean (2011–2012) salinity; (c) vertical profiles of the density anomaly along CalCOFI line 66.7 over the entire 2-year period of 2011–2012 and in different seasons. In (c), both the CUGN data (orange lines) and model results (blue lines) are averaged along the cross-shore direction as shown in (a) and (b), with the shading representing ± 1 standard deviation.

257 overall level and the horizontal distribution of mean SST during 2011–2012 are reasonably
258 captured with a predominantly cold bias throughout the domain, except at the Golden Gate
259 where modeled SST is warmer than OSTIA SST. Overall, biases are smaller than 1°C in
260 magnitude, which is less than the OSTIA standard deviation throughout the domain. We
261 note that instantaneous comparisons of modeled and remotely sensed SST are more variable.
262 Greater discrepancies between model and data on short time-scales are to be expected as
263 small-scale features (e.g., eddies and filaments) are quite nonlinear and less predictable than
264 longer-term mean features.

265 **3.4 The California Underwater Glider Network**

266 The California Underwater Glider Network (<http://spraydata.ucsd.edu/climCUGN/>),
267 CUGN, uses autonomous underwater gliders to measure variables including temperature and
268 salinity. The gliders make repeated dives from the surface to 500-m depth and back, repeat-
269 ing the cycle every 3 hours, and traveling 3 km horizontally each cycle. We compare our
270 model output to the glider data from the cross-shore California Cooperative Oceanic Fish-
271 eries Investigations (CalCOFI) line 66.7 off Monterey Bay (see black dotted line in Figure 6).
272 For ease of comparison, both the CUGN and model data are averaged along the cross-shore
273 direction to obtain vertical density profiles as a function of time. This comparison provides
274 an assessment of the model performance in terms of vertical stratification in the ocean. As
275 shown in Figure 5, agreement in the vertical structure is generally good for the two-year
276 mean of temperature and salinity, with the mean halocline a bit deeper in the model than
277 observations. The model successfully reproduces the shoaling of the pycnocline during sum-
278 mer due to solar heating and upwelling, while also capturing the deepening during winter
279 due to diminished insolation and increased surface turbulence (Figure 5c). The modeled
280 mean pycnocline is, however, deeper (~10 m) than observed in spring and winter, with less
281 (more) dense surface water in fall (summer).

282 **4 Baywater Dispersal**

283 **4.1 Analysis Framework**

284 To examine the patterns of the SFB plume spreading over the continental shelf and
285 beyond, we consider flow across a total of 30 arcs (thick gray lines in Figure 6) centered
286 at the Golden Gate. The radii of the arcs increase by 5 km, starting at a radius of 5 km

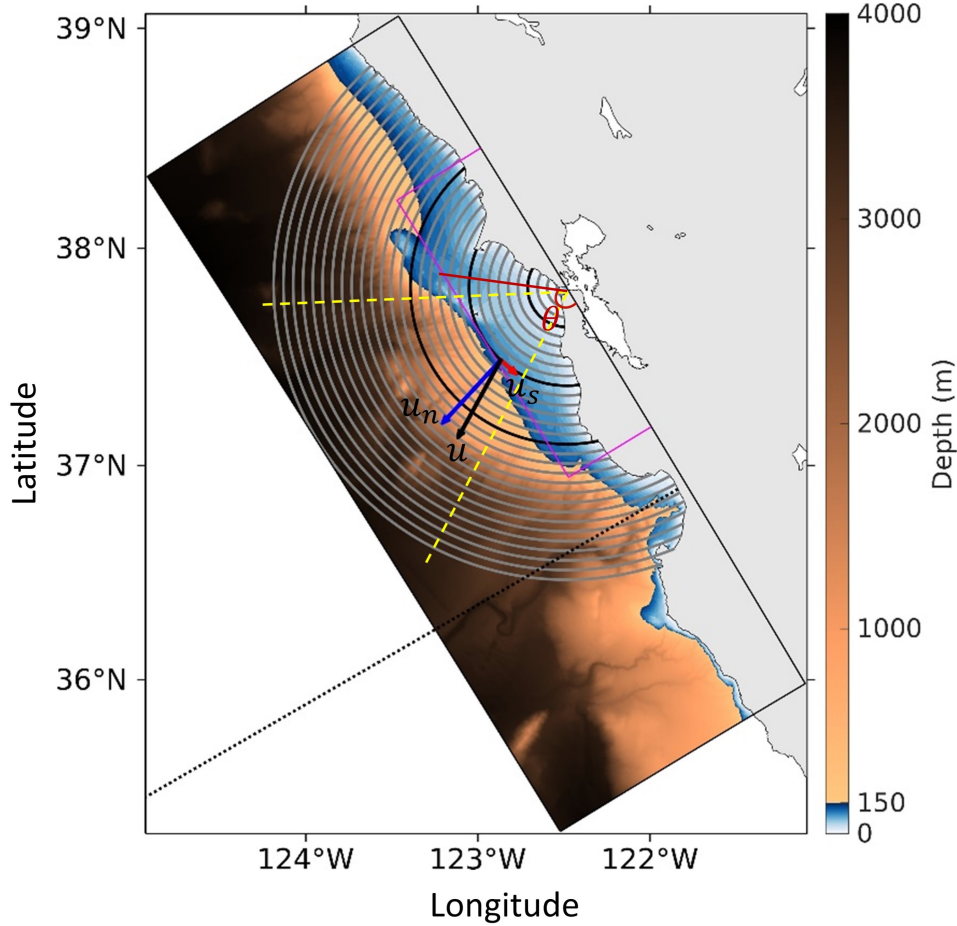


Figure 6. Analysis framework of baywater dispersal superimposed on the bathymetry of the present L2 domain. The continental shelf (defined as regions with depths ≤ 150 m) is highlighted by the bluish colorscale. The concentric arcs on which passive tracer flux is calculated are colored by gray, except for the three black arcs which indicate the locations of the representative arcs in Figure 8. The azimuth angle θ starts at the eastern edge of the grid and increases clockwise. The yellow dashed lines divide the arcs into their southern, offshore, and northern segments (as θ increases from zero). The magenta box indicates the subdomain within which the winds and surface currents are averaged in Figure 10. The CalCOFI line 66.7 is marked by the black dotted line (see section 3.4).

287 (arc 1) out to a radius of 150 km (arc 30). Throughout this paper, “arc i ” corresponds to
 288 the arc with a radius of $5i$ km. At any location on a certain arc, the flow velocity vector is
 289 decomposed into its normal component u_n (blue arrow) and tangential component u_s (red
 290 arrow). Positive u_n is defined as outgoing from the source (i.e., spreading away from the

291 SFB), and positive u_s indicates velocities directed toward the northern end of an arc. We
 292 focus primarily on arcs with radii smaller than 100 km.

293 4.2 Mean Plume Characteristics

294 The two-year (2011-2012) time-averaged, depth-integrated passive-tracer concentration
 295 (Figure 7a) reveals the typical patterns of the SFB plume as it disperses across the northern
 296 and central California shelf. For visualization, the color scale for the depth-integrated tracer
 297 C_{VI} is selected to have an upper limit of 1 in order to emphasize tracer decay structure over
 298 the shelf. The immediate inner-shelf region within the first arc is heavily influenced by the
 299 tidal jets through the narrow Golden Gate, exhibiting elevated levels of vertically integrated
 300 tracer ranging from 1–30. Throughout much of the domain, except for the tidally dominated
 301 region < 25 km from the Golden Gate, the standard deviation of the mean field (Figure 7b)
 302 is considerably larger than the mean, highlighting the plume’s variability. Overall, the plume
 303 influences a large region of the shelf, with the mean tracer found all along the shelf from
 304 near Point Arena to the Monterey Bay.

305 In addition to horizontal variability, the plume is vertically inhomogeneous. Figure 7c
 306 plots the mean centroid depth the SFB plume, $h_c = \int zCdz / \int Cdz$. Overall, the plume
 307 centroid remains shallower than ~ 20 m deep throughout much of the Gulf and to the south,
 308 with plume waters north of Point Reyes extending more deeply. On the innermost arcs, the
 309 plume occupies the whole water depth ($D < 2h_c$). As the arc crosses the shelf break (around
 310 $r = 50$ km), depth increases dramatically and $2h_c$ more reasonably represents the vertical
 311 plume dimension.

312 The 2012 monthly mean fields in Figures 7d–o further illustrate the temporal variabil-
 313 ity of the plume, with the spatial pattern highly variable. Three major baywater transport
 314 pathways emerge: (i) a northward pathway, (ii) a southward pathway, and (iii) an offshore-
 315 directed pathway. The northward pathway is characterized by a sharp, buoyant coastal
 316 current whose tracer signature extends well north of Point Reyes to roughly 120 km up the
 317 coast, largely penetrating deeper than the rest of the plume and travelling closer to the
 318 coast. The second pathway is directed southward from the Golden Gate. It starts as a
 319 strong, broad, shallow feature near its source ($r < 20$ km) that is roughly twice as wide and
 320 the northward pathway and with the highest concentrations shifted offshore. The plume be-
 321 comes increasingly diffuse and less concentrated between 30 and 100 km from the Gate. The

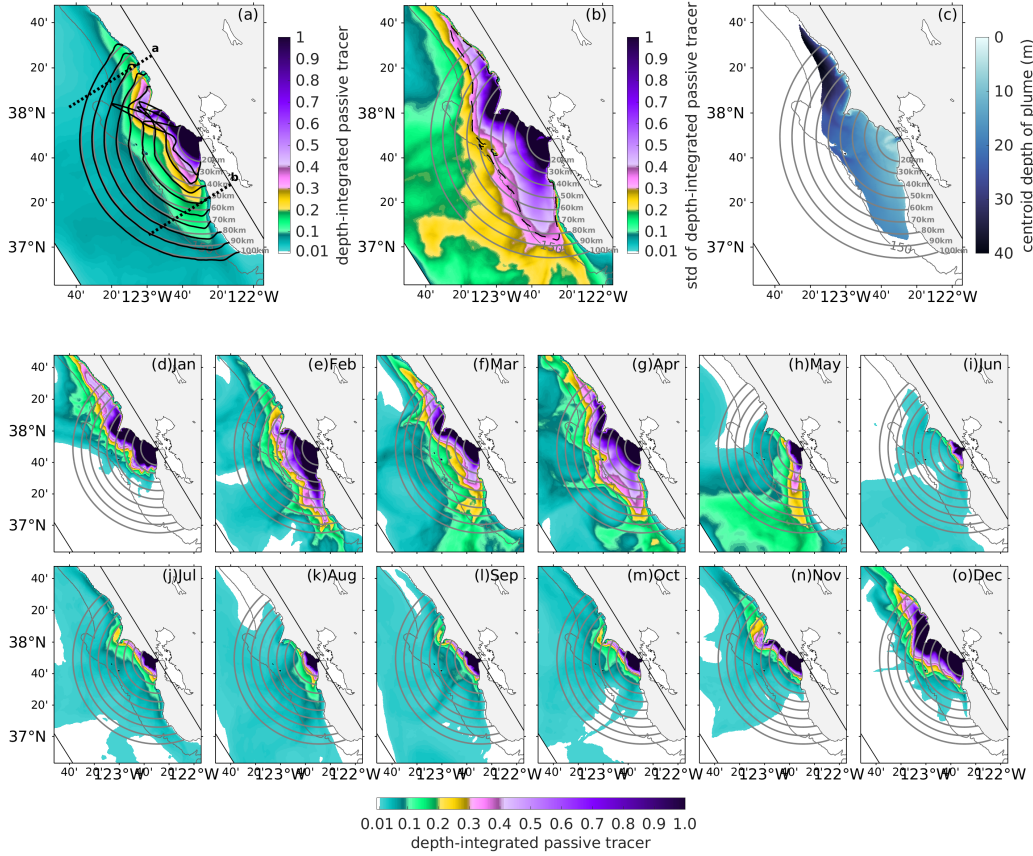


Figure 7. Depth-integrated passive tracer. (a) Two-year mean vertically integrated passive tracer concentration, C_{VI} . Black lines indicate the vertically integrated tracer flux across each arc. The two dotted lines indicate locations of the cross-shore planes in Figure 11 that extend 80 km from the eastern edge of the domain. (b) Standard deviation of mean passive tracer with dashed line indicating the point where $C_{VI} = 0.1$ in (a). (c) Centroid depth of passive tracer within the mean plume. (d–o) Monthly mean vertically integrated tracer concentrations in the year 2012. In all panels, the 150-m isobath is shown as a demarcation between shelf and slope.

322 third pathway is directed westward, but decays offshore quite rapidly, extending only weakly
 323 beyond the shelf-break. This pathway appears transiently and rarely in instantaneous fields
 324 compared to the northward and southward directed motions.

325 The cross-shelf dispersal of baywater seems to be greatly suppressed, with the majority
 326 of the SFB plume body (e.g., with depth-integrated passive tracer concentrations higher
 327 than 0.1) largely inshore of the 150-m isobath (see the portion of plume encompassed by the
 328 dashed line in Figure 7b). Conservation of potential vorticity in a rotating, homogeneous, in-

329 viscid, and steady fluid requires transport along and not across bathymetric contours (Brink,
 330 1998). Though this fluid is not homogeneous, inviscid, or steady, cross-isobath transport is
 331 severely constrained in this region, as it is in other coastal environments. Although cross-
 332 shore Ekman transport at the surface and in the bottom boundary layer, as well as transient
 333 motions (e.g., eddies and filaments), do result in cross-shore flow, their impact on the mean
 334 baywater dispersal is quite modest. While the California Current system is an eddy-rich
 335 region (Kessouri, Bianchi, et al., 2020) with potential impacts on biogeochemical activity
 336 (Gruber et al., 2011), our simulations do not indicate eddy transport as a significant mech-
 337 anism within the Gulf of the Farallones itself. Instead, we find that the eddy kinetic energy
 338 within the Gulf is almost entirely contained within sub-tidal timescales, with little sustained
 339 (sub-)mesoscale energy (not shown).

340 The mean radial flux of baywater reveals vertical and horizontal plume structure at
 341 different distances from the Golden Gate. Figure 8 plots azimuth-depth contours of tracer
 342 flux across three representative arcs. On arc 4 (Figure 8a), a typical two-layer estuarine
 343 circulation (gravitational circulation; Geyer & MacCready, 2014) can be observed even at
 344 this offshore location, with outgoing flux near the surface and ingoing flux at depth. On arc
 345 10 (Figure 8b), the estuarine circulation largely diminishes, and there exists an ingoing flux
 346 between $\theta = 100\text{--}150^\circ$, associated with a recirculation near Drakes Bay and south of Point
 347 Reyes (see Figure 7a). On arc 16 (Figure 8c), the bathymetry deepens significantly as the
 348 arc crosses the shelf break. At this distance, it is clear that the plume exists as a thin layer
 349 in the upper few tens of meters, sharply differentiated from the underlying shelf and slope
 350 water. This structure is a common feature of surface-trapped river plumes (Fong & Geyer,
 351 2002; Horner-Devine et al., 2015).

352 A more quantitative description of the average baywater dispersal can be based on
 353 simple geometrical arguments, testing a model to describe the mean vertically integrated
 354 passive tracer concentration (\overline{C}_{VI}) on a given arc, knowing only the modeled vertically
 355 integrated passive tracer concentration on arc 1 ($\overline{C}_{VI,\text{modeled}}|_{r_1}$). The overbar here indicates
 356 averaging along a given arc (i.e., arc-averaged). The total concentration along an arc of
 357 radius, r , is equal to $2\pi\overline{C}_{VI,\text{calculated}} \cdot r$. If we assume that all of the passive tracer on arc 1
 358 is dispersed onto an outer arc, a uniformly spreading plume would be described as

$$359 \quad \overline{C}_{VI,\text{calculated}} = \overline{C}_{VI,\text{modeled}}|_{r_1} \cdot (r/r_1)^{-1}. \quad (1)$$

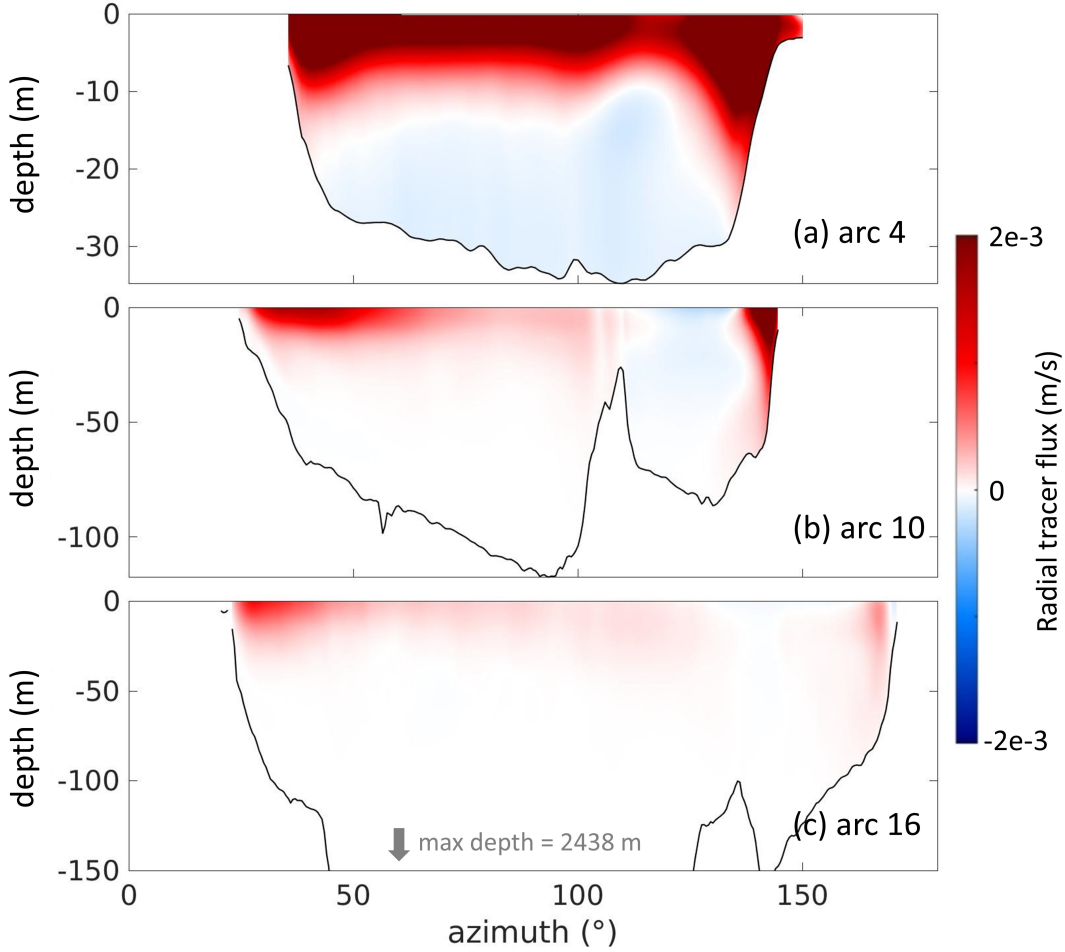


Figure 8. Two-year mean radial tracer flux across three representative arcs. Note the differing extents of vertical axes among panels. In (c), the max depth reaches 2438 meters, but only the upper 150 meters of water is shown.

360 Equation (1) is plotted in Figure 9 for all the 30 arcs considered in section 4.1. Rather
 361 than scaling directly with the ratio of the arc radii, the plume is best described by a -1.4
 362 power law, a more rapid decline in concentration than predicted by pure spreading. The
 363 -1.4 power relationship likely results from the local storage of tracer on the inner arcs and
 364 cross-arc mixing. It is also worth noting that as r increases in Figure 9, the curve of $2\bar{h}_c$
 365 (an approximation for the arc-averaged vertical dimension of the plume) gradually flattens,
 366 in contrast to the considerable increase of arc-averaged water depth \bar{D} . This is consistent
 367 with Figure 8c where the plume exists as a thin surface layer on distant outer arcs.

The above spreading analysis assumes advective dispersal. A similar exercise can also be conducted for a purely diffusive case. Assuming a continuous point source at the origin,

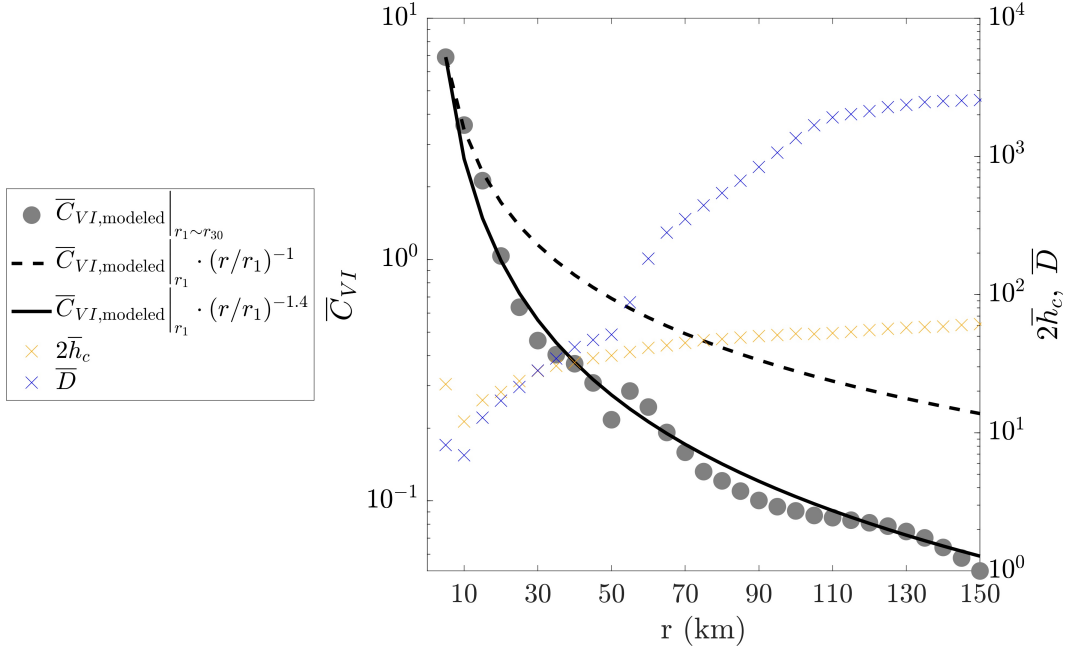


Figure 9. Vertically integrated passive tracer averaged along a given arc, \bar{C}_{VI} , as a function of arc radius, illustrating the geometrical plume spreading.

if the diffusion coefficient is κ and the source strength at radius $r = 0$ is $S > 0$ starting at $t = 0$ when the concentration is $C(r, 0) = 0$, then the concentration on each arc will increase in time and decrease with distance according to (Carslaw & Jaeger, 1959; Crank, 1975):

$$C(r, t) = \frac{S}{4\pi\kappa} E_1\left(\frac{r^2}{4\kappa t}\right), \quad (2)$$

where $E_1(x) = \int_x^\infty \frac{e^{-t}}{t} dt$ is the exponential integral. Under this purely diffusive assumption, the concentration decreases rapidly with increasing radial distance. Combining both the advective and diffusive analysis, we can infer that the transport is predominantly advective, though with some diffusive influence and storage given the more rapid decay in concentration ($r^{-1.4}$) than predicted by pure advection.

4.3 Drivers of Temporal Variability

While mean properties are useful to describe the overall behavior of the SFB plume, temporal information offers understanding of the drivers of plume dynamics. Two-year timeseries of several fields related to baywater dispersal are presented in Figure 10, including the net baywater discharge at the Golden Gate, the cross-shore and along-shore winds, the along-shore barotropic pressure gradient, and the along-shore surface-current velocity.

379 We note that the net baywater discharge in Figure 10a should not be interpreted as the
 380 conventional “river discharge” of typical river plumes because freshwater enters the San
 381 Francisco Bay from the Sacramento River and San Joaquin delta far upstream of the Golden
 382 Gate, and these waters undergo intensive mixing with saline water of coastal origin before
 383 being exported from the estuary. To remove high-frequency signals and focus on subtidal
 384 frequencies, we apply a Godin filter, a three-step low-pass filter (Godin, 1972), to all time-
 385 series in this figure. Despite this filtering, there remains a small spring-neap cycle visible in
 386 Figure 10a that likely still results from tidal aliasing. Winds and surface currents are spatial
 387 averages within a sizable subdomain (indicated by the magenta box in Figure 6) that spans
 388 the majority of the region of interest. Positive baywater flux is defined as outgoing from
 389 SFB.

390 The bay discharge (Figure 10a) shows largest amplitude in the spring of 2011 with small
 391 values through the rest of the 2-year period. The winter/spring signal in Q is surprisingly
 392 muted in 2012. Characteristic equatorward winds are apparent during much of the two years
 393 (Figure 10c), punctuated by brief reversals (also referred to as relaxations) that last a few
 394 days except for more sustained poleward winds during early spring of 2011 and 2012 and
 395 late fall/winter of 2012. The spatial mean along-shore surface current (Figure 10e) generally
 396 follows that of the along-shore wind, except for September 2011–January 2012 when the
 397 Davidson Current (a poleward surface coastal current off U.S. West Coast) dominates (Reid
 398 & Schwartzlose, 1962; Hickey & Pola, 1983; Connolly et al., 2014). This is manifested by
 399 the poleward barotropic pressure gradient between September 2011 and January 2012 in
 400 Figure 10d.

401 Figure 10f–h presents plume dispersal characteristics, including net baywater discharge
 402 across arc 10 ($r = 50$ km) as a function of time and angle relative to the alongshore strike
 403 of the coast (Figure 10f), the total transport across arc 10 in the three pathways identified
 404 (Figure 10g), and the angle reached by the furthest point on the plume with a vertically
 405 integrated passive-tracer concentration of at least 1.0 (Figure 10h). An azimuth of 25° indi-
 406 cates transport adjacent to the coast south of the Golden Gate, 90° indicates the direction
 407 directly offshore, and 145° corresponds to waters adjacent to the coast to its north. Regions
 408 with azimuth ranges of 0° – 25° and 145° – 180° are land-masked.

409 Figure 10f reveals characteristic spatial and temporal patterns of baywater discharge.
 410 Export from the Golden Gate generally crosses arc 10 either over much of its southern

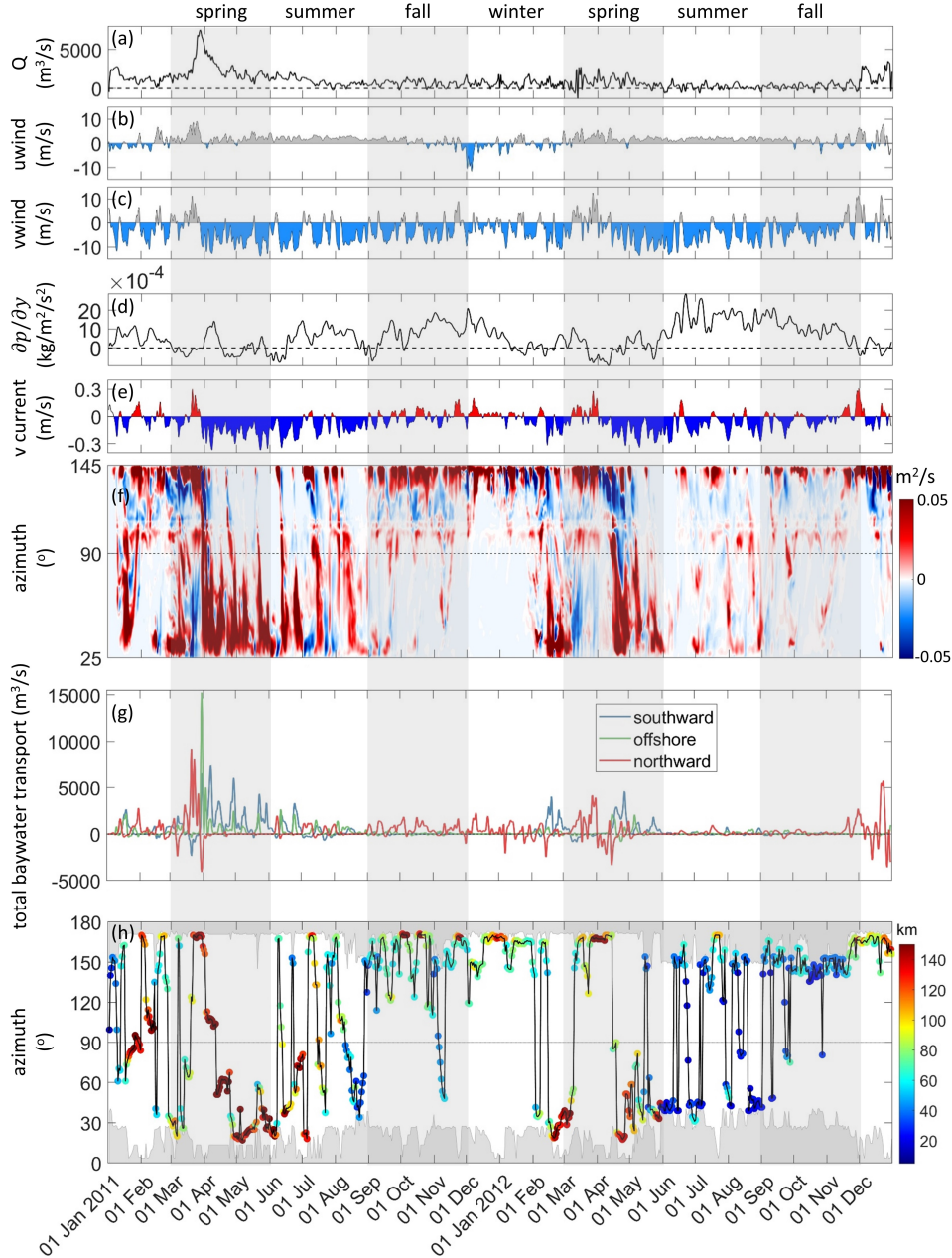


Figure 10. Godin-filtered time series of (a) net baywater discharge at the Golden Gate; (b) subdomain-averaged cross-shore wind (light blue indicates easterly wind); (c) subdomain-averaged along-shore wind (light blue indicates northerly wind); (d) along-shore barotropic pressure gradient, $(p_{\text{south}} - p_{\text{north}})/L$, in a narrow coastal band (L is the along-shore distance between the northern/southern boundaries); (e) subdomain-averaged along-shore surface current (blue indicates southward current); (f) vertically integrated baywater flux across arc 10.; (g) spatially integrated baywater transport across the three segments of arc 10; (h) positional history of the plume front. In (h): color indicates the radius of the outermost arc across which the maximum vertically-integrated tracer concentration C_{VI} is higher than 1.0; and vertical axis indicates the azimuthal location of maximum value on the outmost arc; gray-shaded area represents the coastal land-masked cells for the corresponding arc.

411 half, or in a very narrow zone near its northern edge. Between these export signals is a
 412 recirculation that crosses the arc toward the Golden Gate, between $\theta \approx 105^\circ$ and 125° ,
 413 consistent with the baywater circulation shown in Figure 7. All of these features of the
 414 cross-arc flow variability can also be observed for arcs with $r = 20\text{--}60$ km in Figure 7, but
 415 disappear for more distant arcs ($r = 70\text{--}100$ km; not shown).

416 There is a noticeable seasonality in the baywater dispersal patterns, with peak fluxes
 417 predominantly occurring during spring months and the temporal variation of baywater
 418 highly dependent on net input of baywater into the domain, the wind field, and the surface
 419 current. Generally south and northward baywater flux occur during south and northward
 420 alongshore surface currents (Figure 10e), respectively. The baywater transport intensity on
 421 the arc differs between years, with the outgoing flux being stronger and more continuous in
 422 the spring of 2011 than in 2012, and clearly related to the interannual differences in peak
 423 discharge. Overall, there is a pattern of north/south switching, with baywater discharge
 424 generally being larger in magnitude to the south or north but not simultaneously.

425 Consistent with idealized river plume studies (e.g., Fong & Geyer, 2001, 2002; S. Lentz,
 426 2004), the pattern of the along-shore wind field significantly influences the behavior of the
 427 SFB plume. As shown in Figure 11, the direction and magnitude of the wind forcing deter-
 428 mines the plume shape. Southerly, downwelling-favorable wind drives northward dispersal
 429 of baywater and the associated onshore surface Ekman transport confines higher concentra-
 430 tions near to the coast (Figure 11a). Equatorward (northerly), upwelling-favorable winds
 431 lead to southward dispersal of baywater and the associated offshore surface Ekman trans-
 432 port draws the plume away from the coast (Figure 11b). These qualitative descriptions are
 433 borne out in the spatial patterns shown in Figure 7.

434 A plume's trajectory is the result of its forcing history. As such, comparing instantane-
 435 ous forcing to instantaneous plume direction does not result in any significant correlations.
 436 We find, however, that comparing 1-week running means with lag times of up to a few days
 437 can result in high correlations between a forcing parameter and plume azimuth. Azimuth
 438 is most strongly related to the surface currents ($r^2 > 0.8$ for a two-week lag), which are in
 439 turn strongly related to the near-surface winds. As a result, the mean plume azimuth is
 440 also well-correlated with the wind direction ($r^2 > 0.7$), with strengthening northerly winds
 441 resulting in more pronounced southward plume transport.

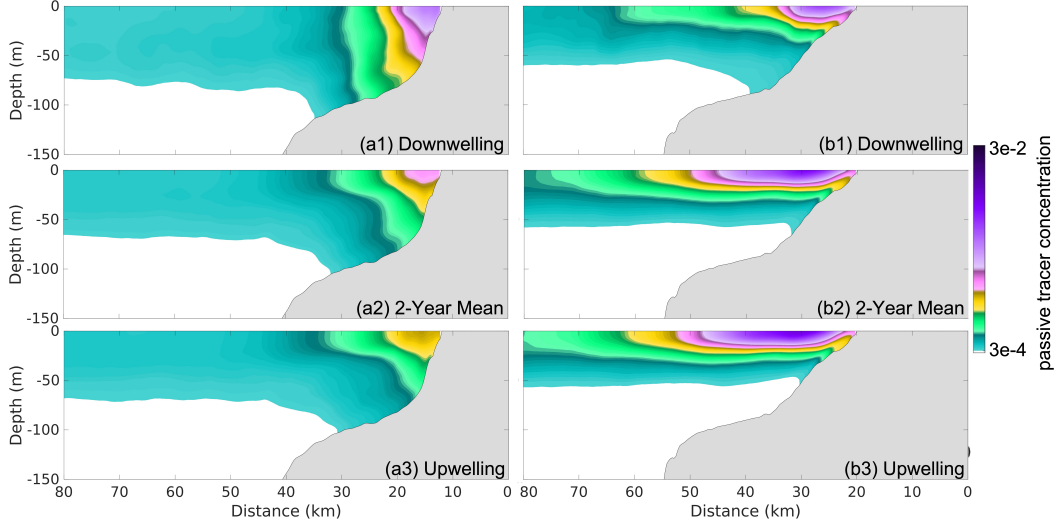


Figure 11. Cross-shore contours of passive tracer concentration at transects a and b in Figure 7a for different conditional averaging: (1) during downwelling (southerly winds) conditions, (2) two-year mean, and (3) during upwelling (northerly wind) conditions.

4.4 Spatio-Temporal Summary of Transport

Based on the discussions in preceding sections, Figure 12 provides a more global perspective on the spatio-temporal pattern of the shelf-wide spreading of the SFB plume. Figure 12 plots the total baywater transport (solid lines) and the total time spent in a given pathway (dashed lines) with increasing arc radius on the vertical axis. More precisely, \bar{Q}_i is the two-year averaged, spatially integrated baywater transport across the three arc segments as defined in Figure 6, where i corresponds to one of the following: “total”, “southward”, “off-shore”, and “northward”, and \bar{Q}_{GG} is the two-year mean baywater discharge at the Golden Gate, which is 924 m^3 (an invariant number that is strictly matched between ROMS and SCHISM models). The total time the plume is dominated by southward, offshore, and northward baywater transport, denoted $\sum T_i$, is determined by accumulating periods with the largest intensity of the three pathways throughout 2011–2012 on each arc (see Figure 10g for the example of arc 10 with a radius of 50 km). Finally, $\sum T_{total}$ is the total length of the two-year timeframe.

Values for \bar{Q}_i/\bar{Q}_{GG} reveal how net baywater effluent is distributed along the different transport pathways in a temporally averaged sense. For example, at $r = 75 \text{ km}$, $\bar{Q}_{southward}/\bar{Q}_{GG} = 43.5\%$ (blue solid), indicating that on this arc 43.5% of the total bay-

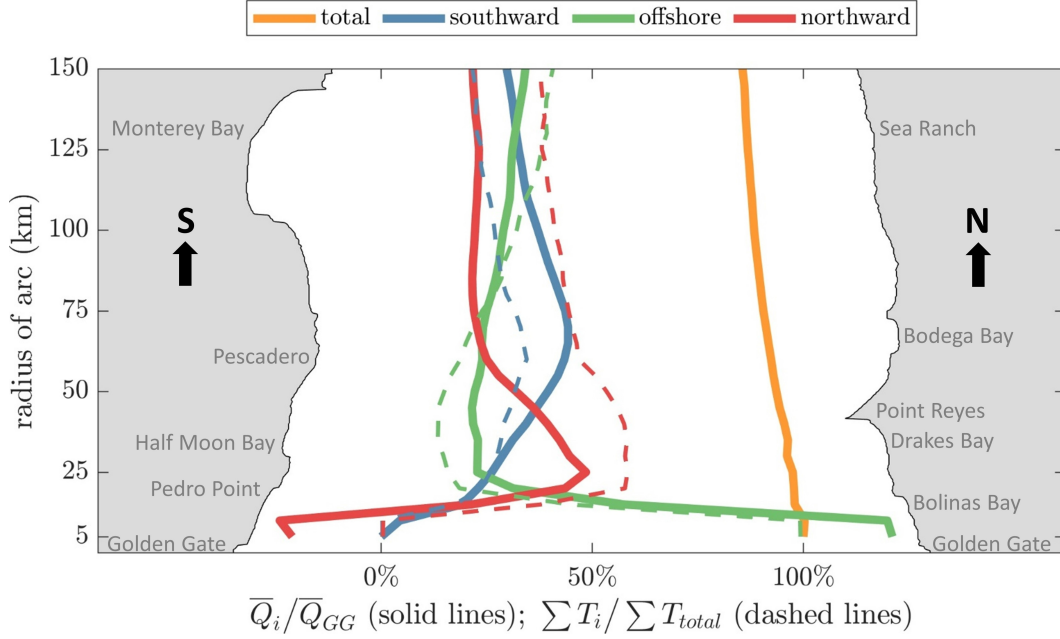


Figure 12. Spatio-temporal pattern of baywater dispersal as a function of arc radius. Solid lines: proportions of two-year mean southward ($\theta = 0-120^\circ$), offshore ($\theta = 120-240^\circ$), and northward ($\theta = 240-360^\circ$) transport of the total 2-year mean discharge at the Golden Gate (924 m^3); Dashed lines: fraction of time dominated by southward, offshore, and northward transport throughout 2011–2012. The southern and northern coastlines surrounding the Golden Gate are superimposed to provide context for the given radii.

459 water discharge is dispersed along the southward pathway. Near the Golden Gate ($r < 25$
 460 km), offshore transport $\bar{Q}_{offshore}/\bar{Q}_{GG}$ (green) dominates other pathways and for $r < 10$
 461 km, the northern pathway (red) is negative, indicating a return flow on northern segments.
 462 Offshore transport declines rapidly from the Golden Gate as the baywater tracer flux shifts
 463 primarily to the northern and secondarily to the southern pathways. At arcs free from the
 464 SFB tidal pulses ($r > 25$ km), $\bar{Q}_{offshore}/\bar{Q}_{GG}$ shows a mild increase as it receives tracer
 465 from two separate sources: (i) Tracer within the northward pathway shifts to the offshore
 466 pathway due to southward transport near Point Reyes ($25 < r < 50$ km) and direct ad-
 467 vection by the prevailing northerly wind still further north ($r > 50$ km). The northward
 468 fraction, $\bar{Q}_{northward}/\bar{Q}_{GG}$, shows a corresponding decrease for $25 < r < 70$ km; (ii) The
 469 offshore pathway also receives offshore-advected water from the southward pathway due to
 470 surface Ekman transport and possibly from the transient, directly offshore motion. This is
 471 accompanied by the decrease of $\bar{Q}_{southward}/\bar{Q}_{GG}$ for $70 < r < 150$ km. Comparing vari-

472 ations of $\bar{Q}_{northward}/\bar{Q}_{GG}$ and $\bar{Q}_{southward}/\bar{Q}_{GG}$ for $50 < r < 70$ km reveals that much of
 473 the water originally along the northward pathway is ultimately passed on to the southward
 474 pathway, with the offshore third acting as a mediator. The fact that there is no noticeable
 475 increase in the offshore transport at this distance is indicative of the tracer passing through
 476 the arcs with no flux divergence in and out of the region. The sum-total baywater transport
 477 $\bar{Q}_{total}/\bar{Q}_{GG}$ (yellow) gradually decreases towards outer arcs due to small local storage of
 478 tracer in areas between the inner arcs over this two year period.

479 The ratio of $\sum T_i/\sum T_{total}$ (dashed lines in Figure 12) reveals how dominant each path-
 480 way is through the modeled period and comparing $\sum T_i/\sum T_{total}$ to \bar{Q}_i/\bar{Q}_{GG} reveals infor-
 481 mation about the intensity of transport. For example, the fraction of southward transport,
 482 $\bar{Q}_{southward}/\bar{Q}_{GG}$ always exceeds the fraction of time the plume is dominated by southward
 483 transport, $\sum T_{southward}/\sum T_{total}$. This means that the southward pathway accounts for a
 484 larger portion of the total baywater transport in less time. In contrast, $\bar{Q}_{northward}/\bar{Q}_{GG}$ is
 485 always less than $\sum T_{northward}/\sum T_{total}$ meaning that the more frequent northward pathway
 486 accounted for less transport of plume water over the two-year period. This imbalance in
 487 transport is likely due to the coincidence of peak discharge and persistent northerly wind
 488 in Spring of 2011 (Figure 10), rather than an indication that the southward transport is
 489 somehow more efficient. The offshore pathway, having strong interaction with the two along-
 490 shore pathways, exhibits an intermediate state with a transition point $r \simeq 80$ km (where
 491 the solid and dashed green lines intersect). Performing an average across all the 30 arcs,
 492 weighted by arc radius, we are able to give the following estimates of the spatio-temporal
 493 pattern of SFB plume dispersal during 2011–2012: (i) of the two-year mean net discharge of
 494 924 m^3 , 11.1% is stored within 150 km of the Golden Gate, 35.1% is dispersed southward,
 495 29.7% is dispersed offshore (up to the shelf break), and 24.1% is dispersed northward; (ii)
 496 across the two-year time span, the discharged baywater is dispersed southward for 26.0% of
 497 the time, offshore for 31.8% of the time, and northward for 42.2% of the time.

498 5 Water Age

499 Water age has utility for estimating ventilation rates of ocean basins, inferring ocean
 500 circulation and mixing, and studying rates of biogeochemical processes (W. G. Zhang et al.,
 501 2010). In this section, we focus on the time scale associated with the spreading of the SFB
 502 plume over the northern and central California shelf. We apply the constituent-oriented age
 503 theory (Delhez et al., 1999) to the circulation of the SFB-sourced water.

5.1 The Constituent-Oriented Age Theory

According to the constituent-oriented age theory (Delhez et al., 1999), the age of a passive tracer is a time-dependent, pointwise quantity that can be obtained from the solution of two partial differential equations governing the evolution of the concentration of the passive tracer (C) and an auxiliary variable called the “mean age concentration” (α).

In this approach, each fluid parcel at position \mathbf{x} and time t is recognized to consist of constituents having different ages (i.e., times since leaving the Golden Gate). A parcel’s age concentration (i.e., the concentration of tracer with a particular age τ) is denoted $c(\mathbf{x}, t, \tau)$, where \mathbf{x} refers to the parcel position at time t . The total passive tracer concentration is calculated as the integral of the age concentration across all ages $C(\mathbf{x}, t) = \int_0^\infty c(\mathbf{x}, t, \tau) d\tau$, and the mean age concentration $\alpha(\mathbf{x}, t)$ is given by the first moment of the age concentration, $\alpha(\mathbf{x}, t) = \int_0^\infty \tau c(\mathbf{x}, t, \tau) d\tau$. The mean age, $a(\mathbf{x}, t)$, is obtained as the ratio of the mean age concentration to the total tracer concentration,

$$a(\mathbf{x}, t) = \frac{\alpha(\mathbf{x}, t)}{C(\mathbf{x}, t)}. \quad (3)$$

In this application, concentration and age tracers are introduced only at the Golden Gate and there is no production or destruction of tracer within the domain. Concentrations of a given age can be changed through advection, mixing, and aging of the tracer itself. Thus, the evolution of age concentration obeys

$$\frac{\partial c}{\partial t} = \nabla \cdot (\mathbf{u}c - \mathbf{K} \cdot \nabla c) - \frac{\partial c}{\partial \tau}. \quad (4)$$

Here, the flow velocity is given by \mathbf{u} , and \mathbf{K} represents the eddy diffusivity tensor. The final term on the right-hand side represents the aging of water within the grid cell. The integral of equation (4) with respect to τ yields an expression for the time evolution of $C(\mathbf{x}, t)$. Applying a sensible constraint on the age concentration, $\lim_{\tau \rightarrow \infty} c(t, \mathbf{x}, \tau) = 0$, one obtains

$$\frac{\partial C}{\partial t} = c(\mathbf{x}, t, \tau = 0) - \nabla \cdot (\mathbf{u}C - \mathbf{K} \cdot \nabla C). \quad (5)$$

The evolution equation for the mean age concentration $\alpha(\mathbf{x}, t)$ is obtained by multiplying equation (5) by τ and integrating in τ

$$\frac{\partial \alpha}{\partial t} = C(\mathbf{x}, t) - \nabla \cdot (\mathbf{u}\alpha - \mathbf{K} \cdot \nabla \alpha). \quad (6)$$

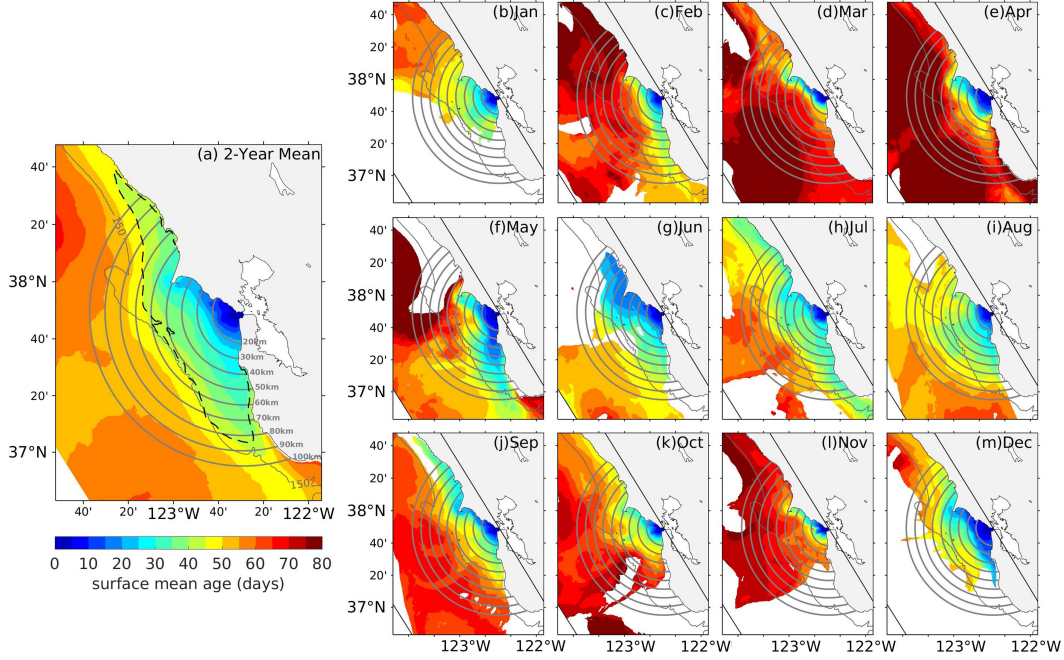


Figure 13. Surface mean age where depth-integrated passive tracer concentration $C_{VI} \geq 0.01$: (a) two-year mean; (b–m) monthly mean in the year 2012.

531 The total tracer concentration $C(\mathbf{x}, t)$ thus drives changes in mean age concentration. Con-
 532 sidering an isolated parcel in the absence of advection and diffusion, if a passive tracer is
 533 non-zero, the mean age concentration increases in time, and $\frac{da(\mathbf{x}, t)}{dt} = 1$.

534 In the present study, the first term on the right-hand side of equation (6) was added
 535 to the ROMS code, and equations (5) and (6) were solved together numerically. Here, we
 536 regard locations where the concentration is lower than 10^{-4} as being free of SFB plume
 537 water, and water age there is undefined. The initial conditions for both C and α is zero.

538 **5.2 Surface Mean Age of the SFB Plume**

539 Figure 13a shows the two-year averaged surface mean age. Water age increases rapidly
 540 with increasing radius from the Golden Gate; starting at 0 days, up to roughly 20 days at a
 541 distance of 20 km from the Golden Gate. Within the main body of the plume ($C_{VI} \geq 0.1$;
 542 encompassed by the dashed line in Figures 7b and 13a), the average surface mean age ranges
 543 from 0–45 days. The maximum value of surface mean age in the Gulf of the Farallones is
 544 around 50 days, which indicates that the SFB-sourced water is typically flushed out of
 545 the region within this time frame. Consistent with the three-pathway pattern of baywater

546 dispersal described in section 4, we see the farthest penetration of young water along the
547 coast north of the Golden Gate. For example, water with a mean age of 45 days can be
548 found 120 km up the northern coast. Water in Drakes Bay is persistently freshened as it
549 retains SFB-sourced water, and the mean age there ranges between 20–25 days. On the
550 other hand, along the southern coast, water with a mean age of 45 days only extends up
551 to 90 km from the Golden Gate. Half Moon Bay experiences slightly older water than just
552 offshore, and Monterey Bay hosts relatively old water with mean age of 55–60 days when
553 the plume travels far enough south.

554 Temporal variability is highlighted when considering monthly averaged surface mean
555 age as shown in Figures 13b–m (c.f., passive tracer concentrations in Figures 7d–o). In
556 some months, water is transported more rapidly through the Gulf, with surface mean ages
557 less than 30 days throughout much of the region (e.g., June). On the other hand, there
558 are months where water is retained for much longer time periods within the Gulf. April
559 shows the oldest average age in the Gulf of the Farallones, that is, around 60–70 days. The
560 mean age is inversely related to the baywater discharge (more rapid flushing associated with
561 stronger outflow). Mean age north of the Golden Gate decreases during northward surface
562 transport of young water directly from the Golden Gate (often associated with southerly
563 winds), and increases during southward transport (often associated with northerly winds).
564 Overall, the cross-shore distribution of surface mean age in Figure 13 echoes the baywater
565 dispersal pattern shown in Figure 7 (i.e., the portion of the southern shelf occupied by
566 young water is wider and shifted offshore more than that of the northern shelf due to the
567 differential Ekman transports).

568 **6 Summary and Discussion**

569 We conducted a study of the dispersal of the San Francisco Bay plume over the northern
570 and central California shelf. Two years (2011–2012) of high-resolution simulations were used
571 to analyze the baywater dispersal pathways and associated time scales (i.e., mean water
572 age) in terms of both mean behaviour and temporal variability. High-frequency ocean-bay
573 exchange data that are available from an existing estuarine model (SCHISM) were applied to
574 the domain’s eastern boundary at the Golden Gate through which the SFB-sourced water
575 enters the coastal ocean. A passive tracer was introduced to facilitate an unambiguous
576 measure of the baywater dispersal.

577 Tidal forcing is an important factor in driving exchange at the Golden Gate (e.g., Fram
578 et al., 2007) as well as mixing (e.g., MacCready et al., 2009, as in the Columbia River plume),
579 particularly within the estuary. Previous work has also shown that tides exert an important
580 influence at the inflow of a buoyant plume over one tidal cycle (McCabe et al., 2009) and
581 can enhance cross-shelf mixing in the absence of other forcing (e.g., Izett & Fennel, 2018a).
582 We did not carry out analysis of mixing associated with tidal bottom stresses along the shelf
583 but generally find that the plume structure is surface enhanced except for a narrow region
584 immediately outside the Golden Gate. Thus while tidal motion is critical in that vicinity,
585 plume variability is largely dominated by wind stress forcing.

586 In spite of the complex coastline of the region, the San Francisco Bay plume behaves
587 similarly to other river-sourced buoyant plumes, including idealized plumes. Upon entering
588 the ocean, the vast majority of the SFB plume is sharply differentiated from the underlying
589 shelf water. We identify three distinct transport pathways: a southward pathway that
590 extends 80 km south of the Golden Gate on average; a northward pathway that reaches as
591 far as 120 km north of the Golden Gate on average; and an offshore pathway that transiently
592 delivers baywater cross-shore, which largely ceases near the shelf break (Figure 7). The
593 natural tendency for the plume to turn north under the influence of the Coriolis force,
594 combined with northward surface currents during downwelling conditions, result in a plume
595 that is narrower and deeper in Figures 7 and 11 (e.g., Fong & Geyer, 2002; Lv et al.,
596 2020; Izett & Fennel, 2018a) compared to the southern branch which is favored during
597 upwelling conditions that result in a broader, shallower plume (as in Fong & Geyer, 2001,
598 2002). Though intra- and inter-annual variability exists, shelf waters within the Gulf of the
599 Farallones exhibit water ages typically less than 50 days from release at the Golden Gate.

600 Overall, we find similar behavior to the Columbia River plume described by Hickey
601 et al. (2005). As with our analysis, they find that a bi-directional plume is present at
602 the Columbia River outflow due to the presence of both upwelling and downwelling wind
603 conditions. The narrower northward branch of the Columbia River plume occurs roughly
604 50% of the time, which is similar to the 42% we find for the SF Bay plume. Despite its less
605 frequent occurrence (26% of the time), the southern pathway contributes most to export
606 (35.1% of total baywater) due to the coincidence of high plume discharge and northerly
607 winds in Spring 2011. Wind forcing is the dominant factor in determining the prevailing
608 direction of the plume, with a lag of three days between a weakening or reversal of winds

609 and a reversal of plume direction. This value is consistent with Hickey et al. (2005) who also
610 find a lag with wind reversal and a propagation of the plume front of roughly 35 km d^{-1} .

611 The dispersal pathways of the plume have implications for biogeochemical processes over
612 northern and central California shelf because the San Francisco Bay is a significant source of
613 nutrients, organic matter, and dissolved and suspended contaminants to the shelf, with loads
614 similar to open ocean inputs (Hurst & Bruland, 2008). The patterns of baywater dispersal
615 revealed here indicate that the destination of material transported in the San Francisco Bay
616 discharge changes rapidly on the scales of a few days, but also with longer-term seasonal
617 differences. The water age analysis echoes the pattern of tracer dispersal pathways, with
618 youngest water near the Golden Gate (<10 days old) and within the main body of the
619 plume (< 50 days on average). For river-borne material that is biologically or geochemically
620 active on time scales from a few days to months, the transport pathways and water age
621 inferred here will influence deposition, availability to the regional marine ecosystem in several
622 national marine sanctuaries (e.g., the Gulf of the Farallones NMS, the Cordell Bank NMS,
623 and the Monterey Bay NMS), as well as regions where material may be exported from the
624 San Francisco Bay by advection. When considering export timescales, a change of just
625 a few days can have a significant impact on the amount of nutrients processed locally or
626 downstream within a plume (Izett & Fennel, 2018b). Similar to the work by Kessouri et al.
627 (2021), follow-up work should use physical-biogeochemical coupled simulations to explore
628 the importance of anthropogenic nutrient loads in the California Current System, which is
629 one of the world's four major wind-driven upwelling systems.

630 **Data Availability Statement**

631 The model code and outputs of this study are available at: <https://doi.org/10.5281/zenodo.7433924>.

632 **Acknowledgments**

633 This work was funded by the San Francisco Estuary Institute (SFEI) grant #1270, the
634 California Ocean Protection Council grant #17661, the National Natural Science Foundation
635 of China (52209085), the Jiangsu Specially-Appointed Professor Program (B1203512), and
636 the Fundamental Research Funds for the Central Universities (B220201033). Computational
637 resources were provided by the Extreme Science and Engineering Discovery Environment
638 (XSEDE) through allocations TG-OCE170017 and TG-OCE030000N. We thank Zhengui
639 Wang and Fei Chai for sharing the SCHISM data of high-frequency ocean-estuary exchanges.

References

- 640
- 641 Basdurak, N. B., Largier, J. L., & Nidzieko, N. J. (2020). Modeling the dynamics of small-
 642 scale river and creek plumes in tidal waters. *Journal of Geophysical Research: Oceans*,
 643 *125*, e2019JC015737.
- 644 Brink, K. H. (1998). Deep sea forcing and exchange processes. In K. H. Brink & A. R. Robin-
 645 son (Eds.), *The global coastal ocean: process and methods* (Vol. 10, p. 151-167). Cam-
 646 bridge, MA: Harvard University Press.
- 647 Cahill, B., Schofield, O., Chant, R., Wilkin, J., Hunter, E., Glenn, S., & Bissett, P. (2008).
 648 Dynamics of turbid buoyant plumes and the feedbacks on near-shore biogeochemistry
 649 and physics. *Geophysical Research Letters*, *35*, L10605.
- 650 Carslaw, H. S., & Jaeger, J. C. (1959). *Conduction of heat in solids*. New York: Oxford
 651 University Press. (520 pp)
- 652 Castelao, R., Schofield, O., Glenn, S., Chant, R., & Kohut, J. (2008). Cross-shelf transport
 653 of freshwater on the New Jersey shelf. *Journal of Geophysical Research: Oceans*, *113*,
 654 C07017.
- 655 Chin, J. L., Ueber, E., Stauffer, P. H., & James W. Hendley II. (2001). *Beyond the*
 656 *golden gate; oceanography, geology, biology, and environmental issues in the gulf of*
 657 *the farallones* (Tech. Rep. No. 1198). USGS.
- 658 Cloern, J. E. (1996). Phytoplankton bloom dynamics in coastal ecosystems: A review with
 659 some general lessons from sustained investigation of San Francisco Bay, California.
 660 *Reviews of Geophysics*, *34*, 127-168.
- 661 Cloern, J. E., Schraga, T. S., Nejad, E., & Martin, C. (2020). Nutrient status of San
 662 Francisco Bay and its management implications. *Estuaries and Coasts*, *43*, 1299-
 663 1317.
- 664 Connolly, T. P., Hickey, B. M., Shulman, I., & Thomson, R. E. (2014). Coastal trapped
 665 waves, alongshore pressure gradients, and the California Undercurrent. *Journal of*
 666 *Physical Oceanography*, *44*(1), 319-342.
- 667 Crank, J. (1975). *The mathematics of diffusion*. London, WI: Oxford University Press.
 668 (414 pp)
- 669 Delhez, E. J. M., Campin, J., Hirst, A. C., & Deleersnijder, E. (1999). Toward a general
 670 theory of the age in ocean modeling. *Ocean Modelling*, *1*, 17-27.
- 671 Deutsch, C., Frenzel, H., McWilliams, J. C., Renault, L., Kessouri, F., Howard, E., . . . Yang,
 672 S. (2020). Biogeochemical variability in the California Current System. *bioRxiv*, *2*(10),

- 673 942565.
- 674 Egbert, G. D., & Erofeeva, S. Y. (2002). Efficient inverse modeling of barotropic ocean
675 tides. *Journal of Atmospheric and Oceanic Technology*, *19*(2), 183-204.
- 676 Fong, D. A., & Geyer, W. R. (2001). Response of a river plume during an upwelling favorable
677 wind event. *Journal of Geophysical Research: Oceans*, *106*(C1), 1067-1084.
- 678 Fong, D. A., & Geyer, W. R. (2002). The alongshore transport of freshwater in a surface-
679 trapped river plume. *Journal of Physical Oceanography*, *32*, 957-972.
- 680 Fram, J. P., Martin, M. A., & Stacey, M. T. (2007). Dispersive fluxes between the coastal
681 ocean and a semienclosed estuarine basin. *Journal of Physical Oceanography*, *37*,
682 1645-1660.
- 683 Garvine, R. W. (1999). Penetration of buoyant coastal discharge onto the continental shelf:
684 A numerical model experiment. *Journal of Physical Oceanography*, *29*, 1892-1909.
- 685 Geyer, W. R., & MacCready, P. (2014). The estuarine circulation. *Annual Review of Fluid*
686 *Mechanics*, *46*, 175-197.
- 687 Godin, G. (1972). *The analysis of tides*. Toronto: University of Toronto Press. (264 pp)
- 688 Gruber, N., Lachkar, Z., Frenzel, H., Marchesiello, P., Munnich, M., McWilliams, J., ...
689 Plattner, G.-K. (2011). Eddy-induced reduction of biological production in eastern
690 boundary upwelling systems. *Nature Geosciences*, *4*, 787-792.
- 691 Hickey, B. M. (1998). Coastal oceanography of Western North America from the tip of
692 Baja California to Vancouver Island. In K. H. Brink & A. R. Robinson (Eds.), *The*
693 *Sea* (Vol. 11, p. 345-393). New York, NY: Wiley and Sons, Inc.
- 694 Hickey, B. M., Geier, S., Kachel, N., & MacFadyen, A. (2005). A bi-directional river plume:
695 The columbia in summer. *Continental Shelf Research*, *25*(14), 1631-1656.
- 696 Hickey, B. M., & Pola, N. E. (1983). The seasonal alongshore pressure gradient on the
697 West Coast of the United States. *Journal of Geophysical Research: Oceans*, *88*(C12),
698 7623-7633.
- 699 Horner-Devine, A. R., Hetland, R. D., & MacDonald, D. G. (2015). Mixing and transport
700 in coastal river plumes. *Annual Review of Fluid Mechanics*, *47*, 569-594.
- 701 Hurst, M. P., & Bruland, K. W. (2008). The effects of the San Francisco Bay plume on
702 tracer metal and nutrient distributions in the Gulf of the Farallones. *Geochimica et*
703 *Cosmochimica Acta*, *72*, 395-411.
- 704 Huyer, A. (1983). Coastal upwelling in the california current system. *Progress in Oceanog-*
705 *raphy*, *12*(3), 259-284.

- 706 Izett, J. G., & Fennel, K. (2018a). Estimating the cross-shelf export of riverine materials:
707 Part 1. general relationships from an idealized numerical model. *Global Biogeochemical*
708 *Cycles*, *32*(2), 160-175.
- 709 Izett, J. G., & Fennel, K. (2018b). Estimating the cross-shelf export of riverine materials:
710 Part 2. estimates of global freshwater and nutrient export. *Global Biogeochemical*
711 *Cycles*, *32*(2), 176-186.
- 712 Jacox, M. G., Edwards, C. A., Hazen, E. L., & Bograd, S. J. (2018). Coastal upwelling
713 revisited: Ekman, Bakun, and improved upwelling indices for the U.S. West Coast.
714 *Journal of Geophysical Research: Oceans*, *123*, 7332-7350.
- 715 Kaplan, D. M., & Largier, J. (2006). HF radar-derived origin and destination of surface
716 waters off Bodega Bay, California. *Deep Sea Research Part II: Topical Studies in*
717 *Oceanography*, *53*, 2906-2930.
- 718 Kessouri, F., Bianchi, D., Renault, L., McWilliams, J. C., Frenzel, H., & Deutsch,
719 C. A. (2020). Submesoscale currents modulate the seasonal cycle of nutrients and
720 productivity in the California Current System. *Global Biogeochemical Cycles*, *34*,
721 e2020GB006578.
- 722 Kessouri, F., McLaughlin, K., Sutula, M., Bianchi, D., Ho, M., McWilliams, J. C., ...
723 Leinweber, A. (2020). Configuration and validation of an oceanic physical and biogeo-
724 chemical model to investigate coastal eutrophication in the Southern California Bight.
725 *Earth and Space Science Open Archive*, 1-62.
- 726 Kessouri, F., McWilliams, J. C., Bianchi, D., Sutula, M., Renault, L., Deutsch, C., ...
727 Weisberg, S. B. (2021). Coastal eutrophication drives acidification, oxygen loss, and
728 ecosystem change in a major oceanic upwelling system. *Proceedings of the National*
729 *Academy of Sciences*, *118*(21), e2018856118.
- 730 Large, W. G., McWilliams, J. C., & Doney, S. C. (1994). Oceanic vertical mixing: A review
731 and a model with a nonlocal buoyancy layer parameterization. *Reviews of Geophysics*,
732 *32*(4), 363-403.
- 733 Lentz, S. (2004). The response of buoyant coastal plumes to upwelling-favorable winds.
734 *Journal of Physical Oceanography*, *34*, 2458-2469.
- 735 Lentz, S. J. (1987). A description of the 1981 and 1982 spring transition over the northern
736 California shelf. *Journal of Geophysical Research: Oceans*, *92*, 1545-1567.
- 737 Lv, R., Cheng, P., & Gan, J. (2020). Adjustment of river plume fronts during downwelling-
738 favorable wind events. *Continental Shelf Research*, *202*, 104143.

- 739 MacCready, P., Banas, N. S., Hickey, B. M., Dever, E. P., & Liu, Y. (2009). A model study
740 of tide- and wind-induced mixing in the columbia river estuary and plume. *Continental*
741 *Shelf Research*, *29*(1), 278-291.
- 742 Marchesiello, P., McWilliams, J. C., & Shchepetkin, A. (2001). Open boundary conditions
743 for long-term integration of regional oceanic models. *Ocean Modelling*, *3*(1-2), 1-20.
- 744 Marchesiello, P., McWilliams, J. C., & Shchepetkin, A. (2003). Equilibrium structure and
745 dynamics of the California Current System. *Journal of Physical Oceanography*, *33*,
746 753-783.
- 747 Mason, E., Molemaker, J., Shchepetkin, A. F., Colas, F., McWilliams, J. C., & Sangra, P.
748 (2010). Procedures for offline grid nesting in regional ocean models. *Ocean Modelling*,
749 *35*(1-2), 1-15.
- 750 McCabe, R. M., MacCready, P., & Hickey, B. M. (2009). Ebb-tide dynamics and spreading
751 of a large river plume. *Journal of Physical Oceanography*, *39*(11), 2839 - 2856.
- 752 Reid, J. L., & Schwartzlose, R. A. (1962). Direct measurements of the Davidson Current
753 off central California. *Journal of Geophysical Research: Oceans*, *67*(6), 2491-2497.
- 754 Renault, L., Hall, A., & McWilliams, J. C. (2016). Orographic shaping of u.s. west coast
755 wind profiles during the upwelling season. *Climate Dynamics*, *46*, 273-289.
- 756 Renault, L., McWilliams, J. C., Jousse, A., Deutsch, C., Frenzel, H., Kessouri, F., & Chen,
757 R. (2020). The physical structure and behavior of the California Current System.
758 *bioRxiv*, *2*(10), 942730.
- 759 Renault, L., Molemaker, M. L., McWilliams, J. C., Shchepetkin, A. F., Lemarie, F., Chelton,
760 D., ... Hall, A. (2016). Modulation of wind work by oceanic current interaction with
761 the atmosphere. *Journal of Physical Oceanography*, *46*, 1685-1704.
- 762 Sharples, J., Middelburg, J. J., Fennel, K., & Jickells, T. D. (2017). What proportion of
763 riverine nutrients reaches the open ocean? *Global Biogeochemical Cycles*, *31*.
- 764 Shchepetkin, A. F. (2015). An adaptive, courant-number-dependent implicit scheme for
765 vertical advection in oceanic modeling. *Ocean Modelling*, *91*, 38-69.
- 766 Shchepetkin, A. F., & McWilliams, J. C. (2005). The Regional Oceanic Modeling Sys-
767 tem (ROMS): A split-explicit, free-surface, topography-following-coordinate oceanic
768 model. *Ocean Modelling*, *9*(4), 347-404.
- 769 Shchepetkin, A. F., & McWilliams, J. C. (2009). Correction and commentary for “Ocean
770 forecasting in terrain-following coordinates: Formulation and skill assessment of the
771 regional ocean modeling system” by Haidvogel et al. *J. Comp. Phys.* *227*, pp. 3595-

- 772 3624. *Journal of Computational Physics*, 228(24), 8985-9000.
- 773 Trenberth, K. E., Smith, L., Qian, T., Dai, A., & Fasullo, J. (2007). Estimates of the global
774 water budget and its annual cycle using observational and model data. *Journal of*
775 *Hydrometeorology*, 8, 758-769.
- 776 Wang, Z., Chai, F., Dugdale, R., Liu, Q., Xue, H., Wilkerson, F., . . . Zhang, H. (2020). The
777 interannual variabilities of chlorophyll and nutrients in San Francisco Bay: a modeling
778 study. *Ocean Dynamics*, 70, 1169-1186.
- 779 Whitney, M. M., & Garvine, R. W. (2006). Simulating the Delaware Bay buoyant outflow:
780 Comparison with observations. *Journal of Physical Oceanography*, 36, 3-21.
- 781 Xiao, C., Zhang, W., & Chen, Y. (2021). Impact of shelf valleys on the spread of surface-
782 trapped river plumes. *Journal of Physical Oceanography*, 51, 247-266.
- 783 Zhang, W. G., Wilkin, J. L., & Schofield, O. M. E. (2010). Simulation of water age and
784 residence time in New York Bight. *Journal of Physical Oceanography*, 40, 965-982.
- 785 Zhang, Y., & Baptista, A. M. (2008). SFLFE: A semi-implicit Eulerian-Lagrangian finite-
786 element model for cross-scale ocean circulation. *Ocean Modelling*, 21(3-4), 71-96.
- 787 Zhang, Y., Ye, F., Stanev, E. V., & Grashorn, S. (2016). Seamless cross-scale modeling
788 with SCHISM. *Ocean Modelling*, 102, 64-81.
- 789 Zhou, J., & Stacey, M. T. (2020). Residual sediment transport in tidally energetic estuarine
790 channels with lateral bathymetric variation. *Journal of Geophysical Research: Oceans*,
791 125, e2020JC016140.
- 792 Zhou, J., Stacey, M. T., Holleman, R. C., Nuss, E., & Senn, D. B. (2020). Numerical
793 investigation of baroclinic channel-shoal interaction in partially stratified estuaries.
794 *Journal of Geophysical Research: Oceans*, 125, e2020JC016135.